Generating Detonation Waves in an Annulus via Phased Adiabatic Shocks

Joseph D. Heath

A thesis

submitted in partial fulfillment of the

requirements for the degree of

Masters of Science

University of Washington

2015

Reading Committee:

Dr. Mitsuru Kurosaka, Chair

Dr. Carl Knowlen, Co-Chair

Program Authorized to Offer Degree:

Aeronautics and Astronautics

University of Washington

Abstract

Generating Detonation Waves in an Annulus via Phased Adiabatic Shocks

Joseph D. Heath

Chair of the Supervisory Committee:
Dr. Mitsuru Kurosaka
Aeronautics and Astronautics

This thesis documents the design and development of a continuous rotating detonation combustor. The design of the combustor incorporates a new system to initiate and control detonation waves within an annular duct. This system known as the wave controller functions by generating phased adiabatic shocks using an azimuthal array of spark plugs. The main intent of the research was to determine the effectiveness and usability of the wave controller in developing transverse waves to initiate a detonation wave. Imaging data of the adiabatic shocks in the annulus was obtained using a high-speed camera and optical setup. The data presented here illustrates the wave controller's capability in creating transverse shock waves traveling circumferentially. Another aspect of the research is to introduce a new injection scheme and provide experimental results on its effectiveness in mixing fuel and oxidizer.

TABLE OF CONTENTS

CONTENTS

LIST OF FIGURES

LIST OF TABLES

ACKNOWLEDGEMENTS

I would like to first acknowledge Mitsuru Kurosaka for his knowledge and support throughout my graduate education. Only with his ideas and theory regarding continuous rotating detonation, were we able to make great strides in advancing the technology. I was provided with a major role in the design and development of the combustor and I appreciated Mitsuru's high level of confidence in me throughout the entire process. Overall, he was a great mentor, advisor, and friend.

I would also like to thank Carl Knowlen for being such a great resource throughout the entire span of the project. He provided significant expertise in the testing and experimentation of all aspects of the combustor. Another major technical expert that was crucial to the advancement of research was Tom Mattick. He designed and built all the electronics for the wave controller. Without the system he developed, this research would not have been possible. In designing the injection method, it was invaluable to have resident fluid mixing expert, Bob Breidenthal, as a resource. He provided great insight into what would be the best injection method for the combustor.

I would also like to acknowledge the assistance provided by my friend and fellow graduate student, Jake Boening. He made the countless hours of analyzing imaging data much more enjoyable.

Last but not least, I would like to thank my wife Rachel for being very supportive throughout my graduate education and research.

DEDICATION

To Vivy, the newest joy in my life.

Chapter 1. INTRODUCTION

1.1 THEORY OF DETONATION COMBUSTORS

1.1.1 *Types of Combustion*

Combustion is a chemical reaction in which fuel burns in the presence of an oxidizer. There are two types of combustion reactions. The most common type is called deflagration combustion. In this scenario, the fuel and oxidizer react and the flame propagates at subsonic speeds. Examples of this form of combustion include the combustors of jet engines and rocket engines, the Bunsen burner and a gas stove. Alternatively, combustion in which the flame propagates at supersonic speeds is called detonation. In detonation burning, the flame travels upwards of 2,000 m/s and also generates an accompanying shock wave.

1.1.2 *Pressure Gain Combustion*

Detonation combustion is also referred to as pressure gain combustion. This is one of the benefits of detonation burning over deflagration is the rise in pressure during the combustion process. In order to examine the effect of the pressure gain in detonation burning, a more in-depth look at deflagration combustion must be considered. In ideal deflagration combustion the pressure remains constant. This ideal situation is also described as isentropic. Consider the combustion in an ideal Brayton cycle as depicted in Figure 1.1 (the grey section). Each point in the diagram specifies the state of process. States 1-2a is the compression stage of the cycle. For the ideal cycle it follows the curve of constant temperature. The OPR (overall pressure ratio) determines the pressure at state 2. Combustion occurs from states 2a-3. The deflagration combustion process results in an increase of both temperature and specific volume, while pressure remains constant. The final stage of the cycle is called expansion and is shown by the curve from 3-4. Here the pressure decreases in addition to an increase in specific volume. Similar to the compression stage, the expansion stage follows the line of constant temperature. To reiterate, this description only applies to the ideal or isentropic Brayton cycle. In reality, no thermodynamic cycle is an isentropic process. The increase in entropy would manifest itself in all the stages of the cycle through pressure and temperature losses. The benefit of representing thermodynamic cycles in this manner helps quantify the available work output of the cycle. The total capable energy

output of the process is determined by the area enclosed by the lines. In comparing the ideal cycle to the non-isentropic one, it is evident that the entropy rise associated with the compression, combustion, and expansion decreases the enclosed area and thereby lowering the total energy output.

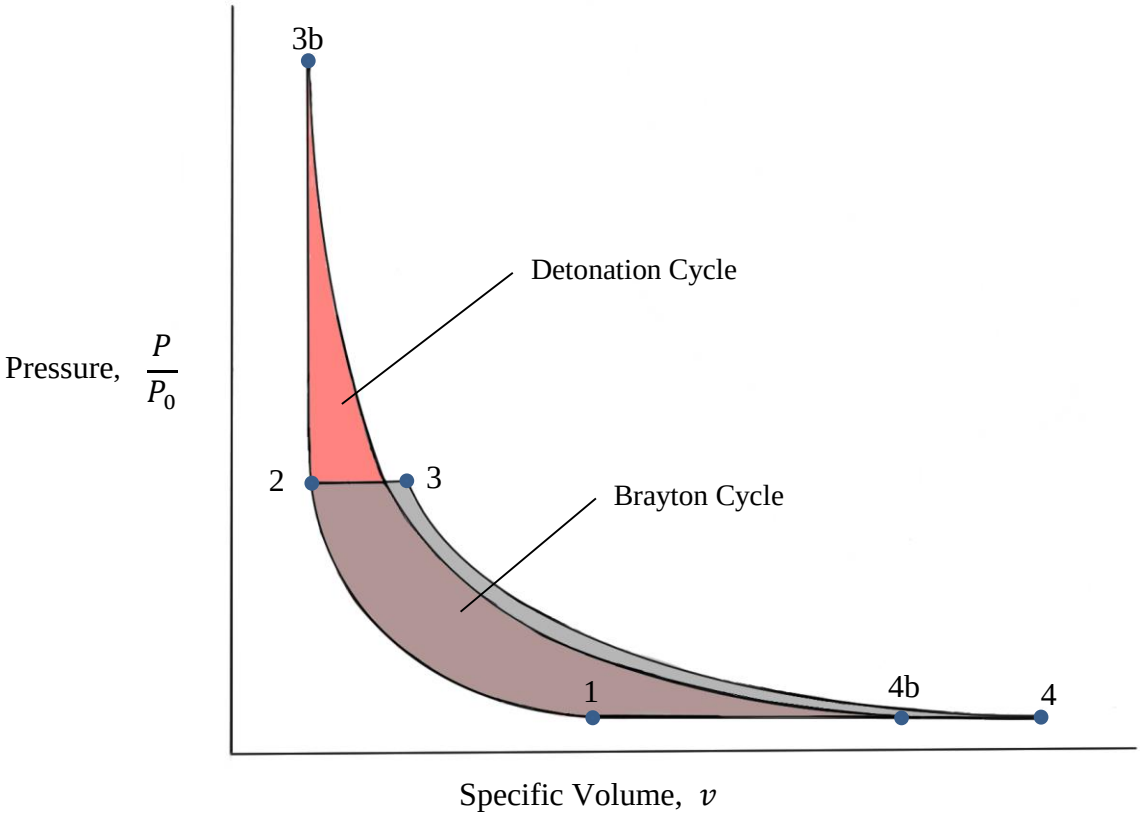

Figure 1.1: Brayton Cycle compared to detonation combustion of Fickett-Jacob Cycle [1]

Now consider if in this same scenario the deflagration combustor were replaced with a detonation combustor. This is known as a Fickett-Jacob cycle. Detonation not only increases the pressure during combustion, it also combusts under a constant volume. Assuming that the detonation has the same temperature increase as the deflagration model, the effect of pressure gain would result in the process moving from states 1, 2, 3b, 4b on the same P-V diagram shown in Figure 1.1. From this modification it is apparent that the detonation modified Brayton cycle has a larger enclosed area, which translates to more available work output. With the detonation combustion of the Fickett-Jacobs cycle, the increase in total energy output is near 20% when compare to the deflagration equivalent cycle. While there are benefits of pressure gain

combustion, creating a system to deliver repeatable and controlled detonation combustion has proven difficult.

1.1.3 *Continuous Rotating Detonation Combustor*

One of the first designs to utilize pressure gain combustion is a continuous rotating detonation combustor (CRDC). This particular incarnation uses a cylindrical annular combustion chamber to enclose detonation waves which travel azimuthally. Fuel and oxidizer are constantly injected into one end of the combustor to begin the reaction. A detonation wave is commonly initiated using a pre-detonator. This is a device that is aligned tangentially to the combustor which "shoots" a detonation wave into the annulus. The detonation wave consumes the reactants as it rotates around the annulus. Provided that the combustion reactants are consistently injected, the detonation wave is self-sustaining. The rotating wave also produces an oblique shock wave that produces a helical pattern toward the exit. This oblique shock acts like a nozzle throat causing the combustion products to exit the combustor at supersonic speeds, producing thrust. A depiction of this process is shown below in Figure 1.2.

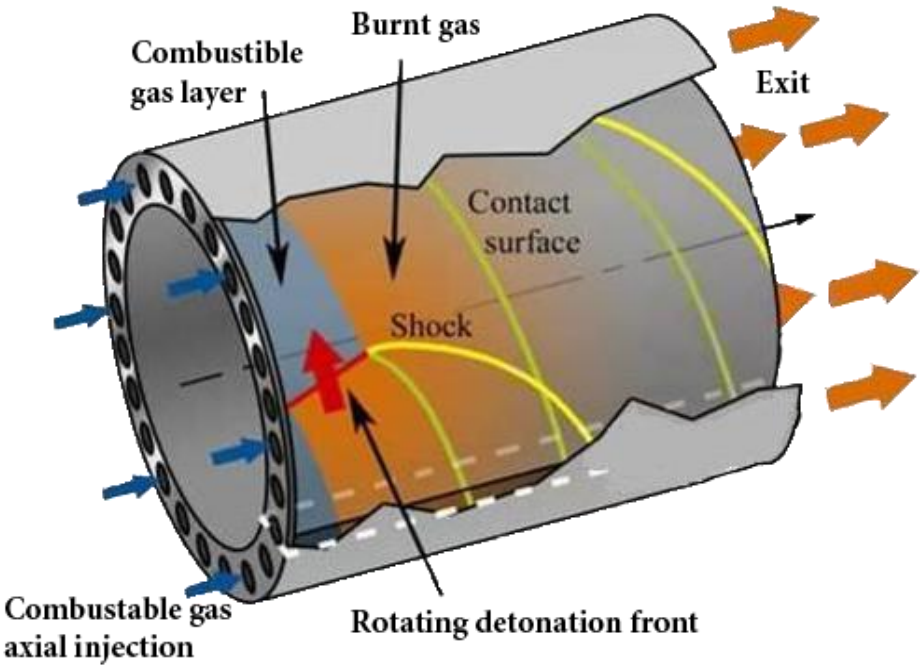

Figure 1.2: Continuous rotating detonation operation in an annulus.

One of the benefits of this design is that the geometry doesn't require a nozzle at its exit to produce supersonic flow. Effective, well-designed nozzles can be very difficult manufacture.

1.1.4 *Engine Applications*

The continuous rotating detonation combustor could be applied to many different areas of technology. In the aerospace sector, the combustor could completely replace a bi-propellant rocket engine. The detonation combustor would also work as a pressure gaining combustion process in a ramjet for a supersonic plane. In the ramjet mode, it can provide standing thrust, eliminating a need for a booster or a mother carrier aircraft. Along the same lines, there is potential to incorporate the combustor in a bypass duct of turbojet engine for use as an afterburner. Another possibility is to utilize the combustor as a device to generate energy. By scaling up the combustor and adding a turbine to the exit, the engine could produce energy in the form of shaft work. For this application, the engine could serve as a power plant for a city or a large ship.

1.2 PRIOR EXTERNAL RESEARCH

Since there is great appeal in pressure gain combustion, a significant amount of research has been conducted in hopes to advance the field. However, when specifically considering the area of continuous rotating detonation combustors, the field is more niche. Within the last 15 years, a significant amount of new research has been published. In 2006, some Russian scientists performed an extensive study on varying the size and geometry of continuous rotating detonation combustors [1]. Their work has been very valuable in the developing a combustor design for this research. At the Air Force Institute of Technology, Jason C. Shank developed a continuous rotating detonation combustor [2]. In his experiments, he was successful in generating detonation waves, but in some instances, the waves were moving in opposite directions. While most of the research in the area of continuous detonation has come from universities, several engineers at Aerojet Rocketdyne have been developing their own rotating detonation engines [3]. They were able to obtain high-speed video of the detonation waves, viewed through the open exhaust.

1.3 PURPOSE

One of the common themes from prior research in the field of continuous rotating detonation is the difficulty of controlling the wave detonation direction as well as the number of waves produced. Overcoming this problem is the main intent of the research presented here. This challenge will be confronted by employing a new method of generating detonation waves without the need of a pre-detonator device. The new method will also provide an ability to control the direction and the number of waves generated. The development and design of the entire combustor incorporating this new method of wave control will be presented in the next chapter.

Chapter 2. ENGINE DEVELOPMENT AND DESIGN

The design of the new combustor was developed over several months through collaboration with several team members. This chapter delves into the design process of the combustor and its sub-systems.

In developing the design of the combustor, there were many design goals and specifications to consider. One of the main goals was to keep the combustor as simple as possible. This was done by focusing on a design that was relatively easy to manufacture while also minimizing the number of machined parts. Beyond these general goals, the combustor was required to do the following.

- Implement the new method to create and control a transverse detonation wave.
- Withstand the high temperatures of the detonation combustion for short period of time.
- Be sized accordingly to be retrofitted to the Shock Wave Reactor[1] (SWR) setup.
- Deliver the fuel and oxidizer at a combined flow rates between 100-250 g/sec.
- Measure the pressure at different locations along the azimuthal line of the spark plugs to determine if a detonation wave was in fact created.
- Measure the temperature and pressure at other locations of the combustor

The process of designing a combustor to meet these requirements will be discussed more thoroughly in the following sections.

2.1 THE WAVE CONTROLLER

The most important element of the continuous rotating detonation engine is the system designed to initiate and control the detonation waves. This system is called the wave controller. The theory behind the controller involves generating sequential shock waves or blast waves with phasing at varying azimuthal locations on the annulus. Owing to the non-linear aspect of the path of the waves, the combined waves will coalesce to form a strong single wave. The curvature of the annulus forces the wave to travel circumferentially. This phenomenon is called the whispering

[1] See Appendix A.1 for more details on the Shock Wave Reactor

gallery effect. The name stems from a specific scenario involving a large amphitheater style building that has a continuous circular wall with a large diameter. This is often referred to as a gallery. If a person standing very close to the wall were to whisper in a tangential direction, another person on the opposite half of the circle would still be able to hear the whisper despite being a significantly long distance apart. There are several buildings that exemplify this phenomenon. One particular example is St. Paul's Cathedral in London. Even though the annular duct of the combustor is significantly smaller in diameter when compared to a large gallery, the principle still applies. While the whispering gallery effect is helpful in sustaining the pressure wave, the wave will eventually damp out. This is because the strength or intensity of a pressure wave is inversely proportional to the distance squared. Hence the need for sustaining the original wave generated by the spark. Therefore, an initial blast wave that is consistently sustained by successive blast waves would create a single transverse wave that would rotate around the annulus indefinitely.

A single blast wave can be initiated quite simply with a standard spark plug. While a spark plug typically acts as a catalyst to initiate a combustion reaction, the spark also creates a spherical blast wave emanating from the spark location. From geometry constraints, the best location for the spark plug is along the exterior of the outer cylinder of the annulus, with the spark itself being perfectly tangent to annular duct flow area. Due to the blast wave's spherical nature, a wave emitted from the outer interior wall of the annulus will travel in both azimuthal directions as well as axially. This presents a problem since the eventual goal is to generate a single detonation wave traveling in one direction. By adding more spark plugs around the exterior of the annulus at the same axial position, the wave can be encouraged to travel in one azimuthal direction. This is done by timing the blast waves in such a way that successive blast waves would be perfectly tuned to each other, thus generating a coalesced transverse wave. This tuning process is conceptualized in Figure 2.1.

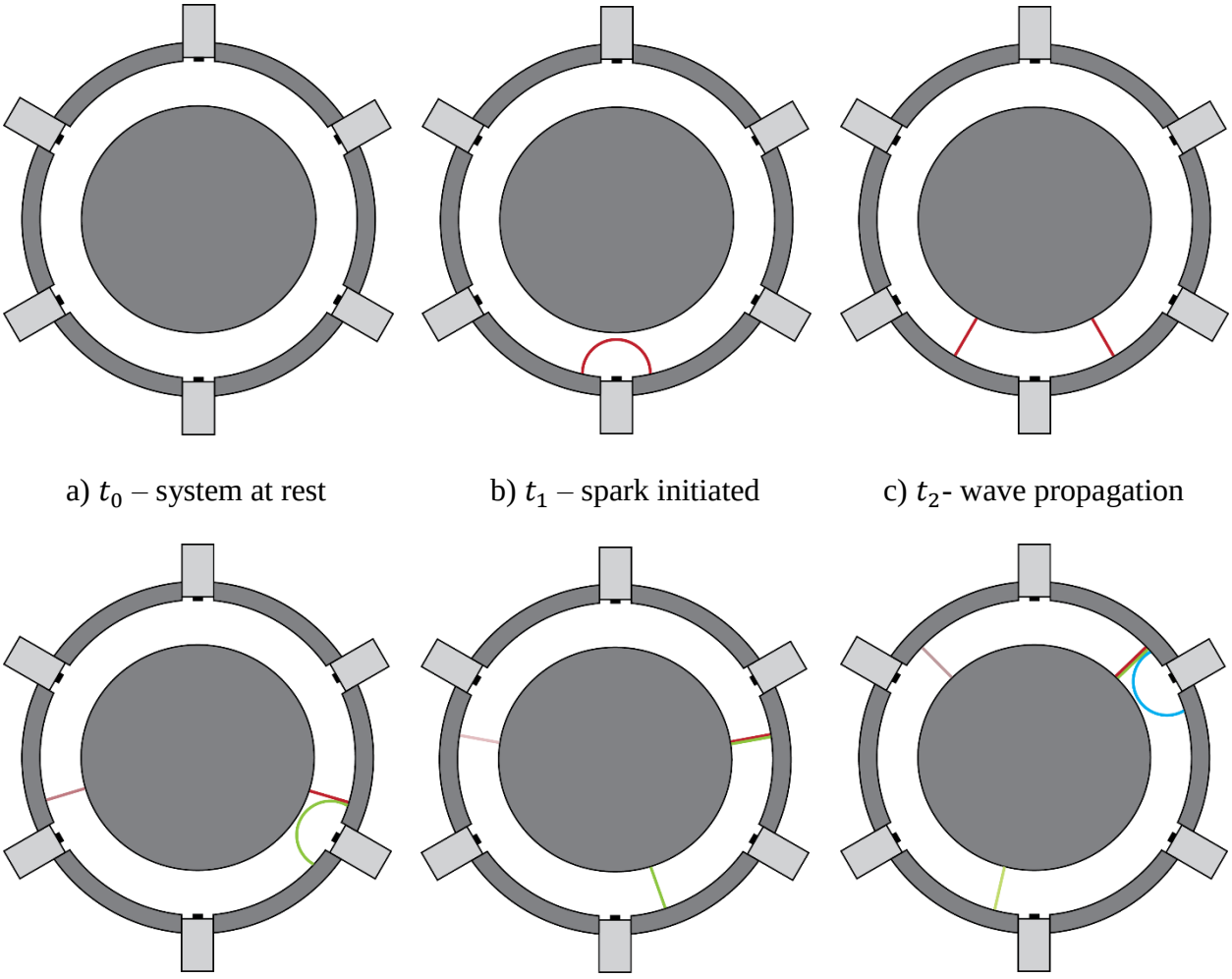

a) t_0 – system at rest b) t_1 – spark initiated c) t_2- wave propagation

d) t_3 – second spark fired e) t_4 – wave propagation f) t_5 – third spark fired

Figure 2.1: Schematic of sparking for wave controller. Each color represents a new wave generated from a spark plug.

In the first frame of the figure, it shows a 2D cross-sectional view of the annular duct. The 6 equally spaced rectangles represent the spark plugs or blast wave initiators. The next frame depicts a moment slightly after the first spark plug is fired. Due to the 2D simplification, the blast wave is illustrated as a red circular arc. As time marches forward, the blast wave continues down both sides of the annulus at a velocity slightly above the speed of sound. Once this wave reaches the next two adjacent spark plugs, only one fires. Thus one azimuthal direction of the initial wave is amplified and the other segment remains at the same intensity. This is illustrated by frame 4. With the initial wave strengthened, the next spark plug further magnifies the

intensity of the wave. By continuing to bolster the wave with additional sparks a transverse wave will emerge within milliseconds.

While the generation of a transverse wave is significant part of the process, it will not create a detonation wave on its own. A detonation involves the combustion of a fuel and oxidizer in combination with a mechanism to induce a supersonic flow scenario. The transverse wave created by the spark plugs acts as the mechanism to transfer the combustion from deflagration to detonation. Not only do the spark plugs create the rotating wave, they also ignite the fuel and oxidizer when both are introduced into the annulus. Once the detonation wave is indeed created, theoretically there is no need to control its motion in the annulus via the spark plugs because the detonation wave is self-sustaining. This of course requires that the detonation wave be continuously supplied with well-mixed fuel and oxidizer. If for some reason the detonation wave begins to migrate in the opposite direction from its original course (which has happened in other continuous rotating detonation research), the wave controller can help compensate for the deviation and maintain smooth operation.

Transferring the 2D conceptual design of the wave controller depicted in Figure 2.2 into three dimensions resulted in the design depicted below.

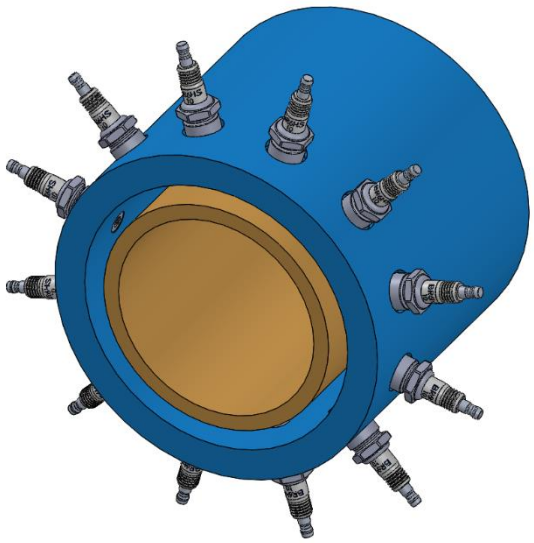

Figure 2.2: Spark plug array aligned along the azimuth at a single axial location.

As shown in the figure, the final design increased the number of spark plugs from six to twelve. This allowed for more modes of operations since it can now accommodate up to four waves

generated simultaneously. Also, by using twelve spark plugs, the distance for a blast wave to travel before it is enhanced was decreased. This increases the overall energy input to the system by the spark plugs, but also enhances the ability of the wave controller.

The electronics behind the spark plug firing mechanism are somewhat proprietary so it will be explained fairly generally. The main component of the spark plug mechanism is the wave controller box. This box required the input of a function and generator and a variable power supply with the ability to control the amperage and voltage. The wave controller box would then output 12 signals; one to each of the spark plugs. The figure below illustrates this general electrical schematic.

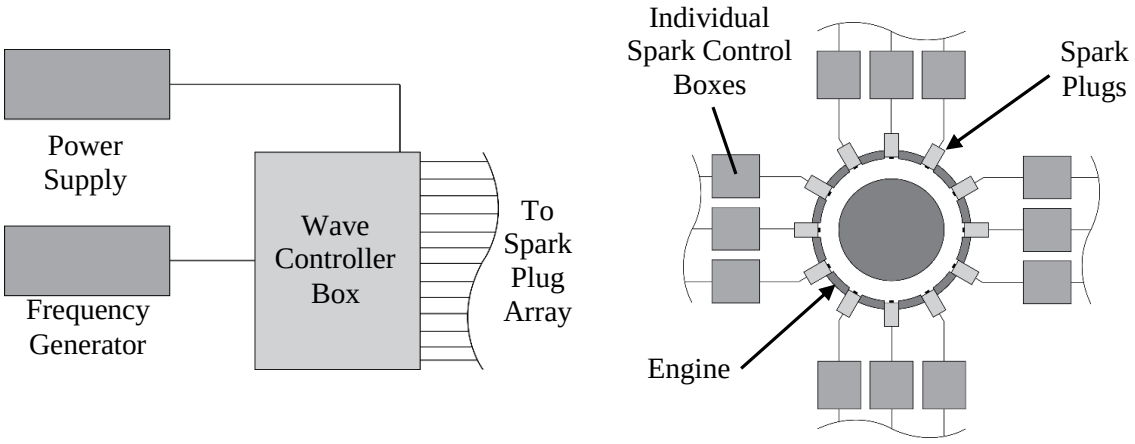

Figure 2.3: General schematic for the spark plug electronics

The box itself had the ability to set the number of waves generated by the spark plug array. It was capable of creating from 1 to 4 distinct waves. The function generator was used to set the frequency of the waves. The frequency on the function generator corresponded to 12 times the frequency of an individual spark plug. Equivalently, the input frequency describes the total number of sparks emitted by all 12 plugs for one second. For example, by inputting a frequency of 9.125 kHz on the frequency generator, each spark plug would fire at a frequency of 760 Hz. This particular frequency was very significant because it corresponded to the time required for a single acoustic wave to make one full rotation around the annulus when the gaseous medium is air. This is also known as the speed of sound frequency. The equations to obtain these values for n-number of waves are shown below.

$$f_{input} = 12 f_{spark} \tag{2.1}$$

$$f_{spark} = \frac{nV}{\pi d_c} \quad (2.2)$$

$$a = \sqrt{\gamma RT} \quad (2.3)$$

$$f_a = \frac{n\sqrt{\gamma RT}}{\pi d_c} \quad (2.4)$$

In these equations, f describes the frequency, n is number of waves generated, and a is the speed of sound for a specific gas.

2.2 COMBUSTOR DEVELOPMENT

In general, a continuous detonation combustor requires at a minimum a duct with one end being the fuel and oxidizer injection point and the opposite end being the exhaust. However, from prior external research it was determined that an annular duct performs better than a completely open duct. The simplest implementation of this annular duct is created by using two concentric cylinders of different diameters. This type of annulus was the basis for the design. In this section, the process of designing the combustor will be discussed, focusing on the main design points and the reasoning behind certain design choices.

2.2.1 *Material Selection*

The material selection for the CRDC was based on two main factors. The first is that the material must withstand the extremely hot temperatures of a detonation wave. This sets the requirement that the material have a relatively high melting temperature and decent thermal conductivity to help dissipate the heat out from the internal walls of the annular combustion area. However, since the energy gained from combustion is directly related to the temperature increase during the reaction, any heat lost due to thermal conductivity through the material will in essence decrease the efficiency of the combustor. This presents a Catch-22 in that the designer has to make a choice on what is more important: efficiency or thermal management. This problem is evident in essentially all combustion engines designs, and especially in turbine or rocket engines. There becomes a point in which the combustor technology is limited by the design material's capabilities.

The second factor for material selection is of lesser importance. Since the CRDC would be adapted to work with the pre-existing Shock Wave Reactor Lab or SWR, the material would need to be somewhat compatible. The bulk of the SWR system utilizes stainless steel for the flow system. By selecting a material with similar heat characteristics including melting temperature, thermal conductivity, and thermal expansion; the possible negative effects of dissimilar material could perhaps be avoided. The main set of the materials that were considered were copper, stainless steel, quartz and other ceramics. The following table lists some of the important characteristics of each material.

Table 2.1: Material specifications

Material	Yield Strength (MPa)	Melting Point (℃)	Thermal Conductivity $(W/m-K)$	Thermal Expansion Coefficient (e^{-6}/K)	Machinability[1]	Welding Capability
Copper C110 (hot rolled)	69	1083	388	17	20%	Low
Stainless Steel 304L	205	1400-1450	16.2	16-17	70%	High
Quartz Type 214 Fused	48	1683[2]	1.4	0.55	Low	None

The data in Table 2.1 provides many insights into what material will work best for the combustor. The most notable fact from the material properties is that none of them have melting temperatures higher than the flame temperature of 3500 K. Since the detonation wave is rotating, the interior walls of the annulus will not be seeing this maximum temperature for the entire operation. The constant maximum temperature assumption also doesn't account for the heat transfer through the metal known as heat soak. For the SS 304L and 214 Fused Quartz, these two materials will have negligible heat transfer due to their low thermal conductivity. Therefore these materials will essentially run hotter when compared to copper since copper will be able to wick" the heat away from the internal surfaces exposed to the combustion reaction. In terms of thermal management, copper is the best choice.

[1] The machinability metric is based on a comparison. For copper it is compared to C360, also known as Free Cutting Brass. For SS 304L, it is compared to Carbon Steel 1212. No such comparison exists for Quartz.
[2] Quartz acts like a glass in that it doesn't have an exact melting temperature. The value for this criteria refers to quartz's softening temperature.

When considering the manufacturing process, which requires significant machining of the combustor for attaching the spark plugs and measurement probes, the best choice is stainless steel. Using SS 304L also ensures that the entire system is constructed from the same metal. The reason that quartz was even considered as a final choice for the combustor material is that it is slightly translucent. With an index of refraction of 1.458, quartz would allow for visual feedback to determine the effectiveness of both the wave controller and the combustion. Despite this fact, the thermal properties and lack of machinability of quartz were too problematic to make it a viable combustor material.

After all these considerations, stainless steel was chosen mainly for its manufacturability, when compared to the other two. While the melting temperature and thermal conductivity are cause for concern, it is important to consider the elapsed time of each combustion test. Each hot-fire test will only last 1 second long. The reason for this set length of time is related to the limits of the flow system and will be further discussed in Section 2.1.6. With this limitation, managing the heat of the combustor due to the flame temperature wave is much less of a concern. To further quantify this the following 1D thermal analysis was performed. The analysis assumes that the exposed wall temperature is held at 3500 K for one second. At one second, the system is purged with a cold inert gas which is assumed to simultaneously drop the temperature to 300 K at the exposed wall. The analysis, shown by the figure below, was developed by a colleague, Jake Boening.

The analysis shows that for the duration of the combustion, 3 millimeters into the wall of the metal will be at or above the melting temperature of the stainless steel. However, within 1.2 seconds of the inert gas purge, the entirety of the internal metal is cooled to a temperature below the melting point. Over the lifetime of the combustor, the internal surfaces of the annulus will degrade even for short one second test durations. While the degradation is unavoidable, the effect can be slightly diminished via external cooling methods. However, active cooling is beyond the scope of the current research. More details regarding active cooling will be discussed in the *Recommendations* section in Chapter 5.

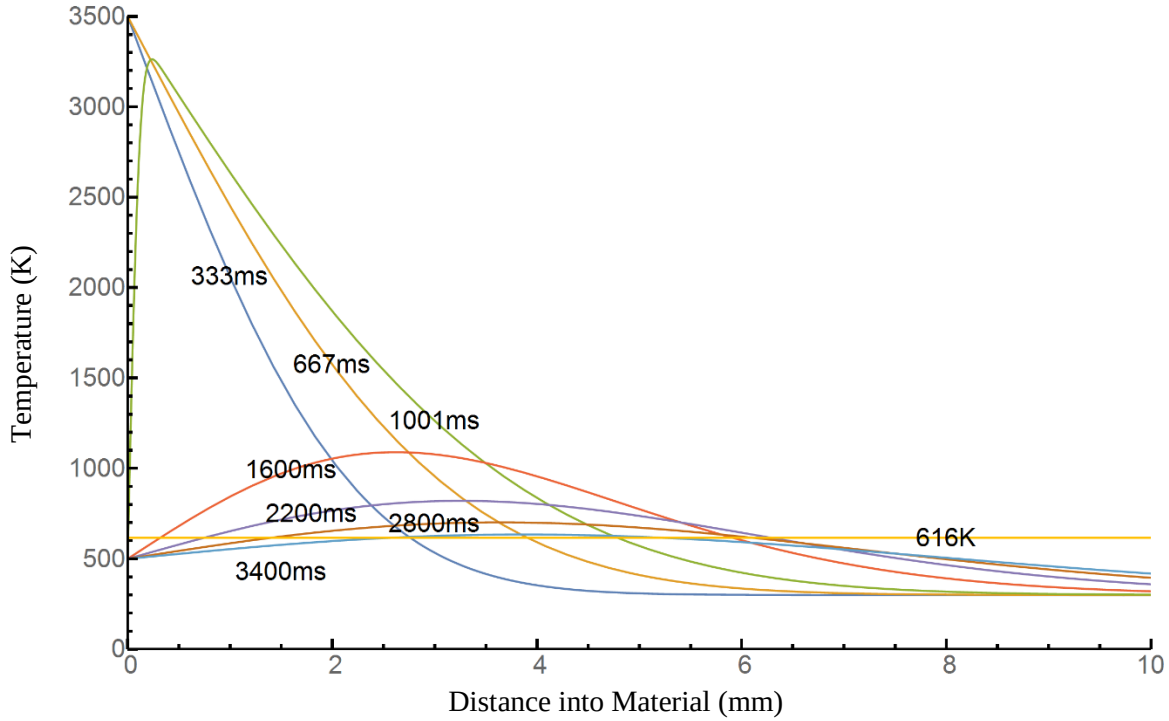

Figure 2.4: 1D thermal analysis of the stainless steel wall of the annulus at different times during the combustion and purge process.

2.2.2 *Sizing the Annular Duct*

The overall size of the combustor and configuration was determined from several factors. The base point in determining the diameter, length, and annular gap of the engine was obtained from the research done by Russian scientists in 2006. From their research, they concluded that the height of the annulus should have the following relationship.

$$\frac{d_o}{d_i} = 1.1\sim1.2 \qquad 2.5$$

Where d_o is defined as the outer radius of the annulus and d_i is the inner radius. Within this range, for constant angular velocity of the detonation waves, their circumferential velocity still remains close to the Chapman-Jouguet detonation speed at all radii of the annular gap. This relationship still allows for the variation of the centerline radius of the annulus. Theoretically, a combustor with an annulus of any radius will function if equation 2.5 is satisfied. One of the driving factors of this radial dimension is the wave controller. As described in the previous section, the wave controller functions by firing an azimuthal array of spark plugs in succession to generate a transverse acoustic wave. Since the wave begins as purely acoustic, the speed at

which this wave travels is the speed of sound. To reiterate from Section 2.1, the speed of sound is defined by the following relationship.

$$a = \sqrt{\gamma RT} \tag{2.6}$$

Where a is the speed of sound, γ and R are the ratio of specific heats and specific gas constant for the particular gaseous medium, and T is the temperature. Using this speed and the circumference of the annulus centerline, the frequency of sparking in Hertz is obtained. This creates the relationship,

$$f = \frac{na}{\pi d_C} \tag{2.7}$$

From this formula, it is evident that as diameter of the annulus is reduced, the frequency increases. This assumes only one wave is traveling in the annulus. The frequency of each spark firing doubles if the number of waves is increased to two. Due to the nature of the electronics running the spark plugs, the maximum frequency is limited to 6.5 kHz per spark plug. Utilizing equation 2.7 with the speed of sound for air and this prescribed maximum frequency, the centerline diameter is around 0.659 inches. This would make a very small combustor, but it actually only provides an initial lower bound on the diameter.

The use of the sound speed in air is just one characteristic velocity of the combustor. However, the wave is expected to evolve from an acoustic wave into a detonation wave. The speed of this detonation wave is a much more important characteristic velocity compared to the speed of sound. While the detonation velocity varies slightly depending on the combustion gases and other physical conditions, the best assumption for this value is the Chapman-Jouguet (CJ) speed. The CJ speed can be determined quite simply with the program called Chemical Equilibrium Analysis or CEA. This program solves many different combustion type problems including Chapman-Jouguet detonation, rocket chamber combustion, shock tube interactions, and many more. It is a decent preliminary analysis for most combustion related problems. Using the ideal detonation model with hydrogen and oxygen as the fuel and oxidizer, respectively, and prescribing standard pressure and temperature values of 1 atm and 300 K the CJ speed is 2,835 m/s. This corresponds to a Mach number of 5.2. In reality, the detonation speed is lower than this value due to thermodynamic losses and other non-ideal conditions. Now using this much larger characteristic velocity and the maximum capable frequency the centerline diameter of the annulus is 5.46 inches. This diameter describes the minimum diameter in which the spark plugs

can maintain a rotating detonation wave travelling at 2,835 meters per second. With this in mind, the centerline radius was chosen to be 6 inches.

Based on this centerline diameter the annular gap could be determined. Modifying equation 2.5 to incorporate the height of the annulus and the centerline diameter results in the following.

$$\frac{d_c + h}{d_c - h} = 1.2 \tag{2.8}$$

Solving for this equation yields an annular height of ~1 cm. The final size to determine is the annulus length. This was also obtained using data from the Russian research. They advised that the length of the annulus be on the same order of the diameter or more specifically,

$$\frac{L}{d_c} \approx 1 \tag{2.9}$$

Using the calculated centerline diameter, the length measured from the spark plug array was established to be near 6 inches. From these calculated sizing constraints for the annulus, the final dimensions required some slight modification in order to be closer to standard pipe and tube sizing. The table below shows the primary dimensional specifications of the annulus.

Table 2.2: Annulus Dimensions in centimeters (inches)

Centerline Diameter	14.28 (5.62)
Annular Gap Height	1.12 (0.44)
Exterior Wall Thickness	1.75 (0.68)
Interior Wall Thickness	0.86 (0.34)
Combustor Length*	13.97 (5.50)

*Measured from the spark plug array

2.2.3 *Propellant Chemistry and Injector Design*

The method of fuel and oxidizer injection is an aspect of the design that directly influences the efficiency of the combustion. Essentially, the better these two compounds mix together the more complete the combustion will be. Because the combustor was being adapted to the SWR, the fuel and oxidizer were determined to be gaseous hydrogen and oxygen reacting at a near stoichiometric mixture ratio. The simplified combustion reaction for these two gases and their respective molecular weights are,

$$2H_2 + O_2 \rightarrow 2H_2O \tag{2.10}$$

$$MW_{H_2} = 2.01\frac{kg}{mol}, \qquad MW_{O_2} = 31.99\frac{kg}{mol}$$

From the chemical reaction equation, the molar ratio of fuel to oxidizer is 2:1. Using the molecular weights of both of the species, the mass ratio was determined to be 1:8, hydrogen to oxygen. The reason for determining the stoichiometric mixture ratio on a mass basis is because the flow rate will be measured in kilograms per second. Therefore the stoichiometric mass ratio is equivalent to the mass flow ratio. This ratio will be helpful in determining the orifice size of the injectors for each gas.

In the desire to achieve the best fluid mixing possible, many different injection configurations were considered and iterated upon. The first configuration explored was based on the impingement of a transverse jet in a primary flow, which is considered to demonstrate quick mixing of two fluids. A simple two dimensional sketch of this method is shown below in Figure 2.6.

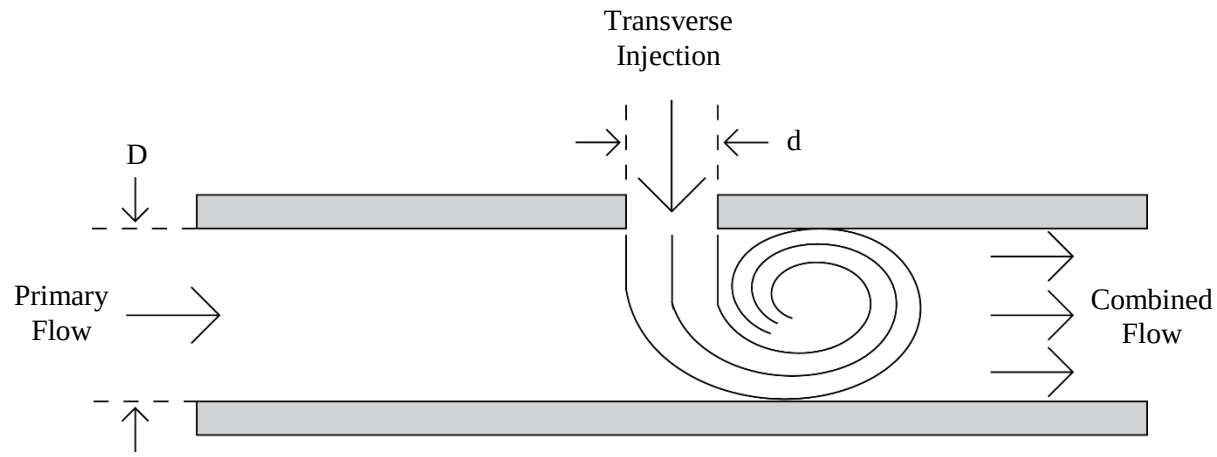

Figure 2.5: Schematic of a transverse jet in a primary flow.

In this scenario, the velocity of the primary, fully-developed flow is low and the transverse jet's velocity is high. This momentum difference helps in enhancing the mixing of the two fluids. A significant amount of research has been conducted in this particular mixing method. In one particular study performed by Edwards, Sherman, and Breidenthal [4], the degree of mixing correlated with the following relationship.

$$\frac{C'}{C} = 0.4\frac{D}{Jx} \tag{2.11}$$

$$J = \frac{(\dot{m}V^2)_j}{(\dot{m}U^2)_p} \tag{2.12}$$

Equation 2.11 represents the concentration fluctuation of the fluid mixture at a distance x from the point of transverse injection. Therefore, the quality of mixing is improved as the fluctuation in concentration approaches zero. The variable J represents the ratio of momentum between the two streams. D represents the diameter of the duct and x is the distance down the duct from the injection point. The researchers varied the momentum ratio within the subsonic flow regime and recorded the results. These results are depicted here in Figure 2.6.

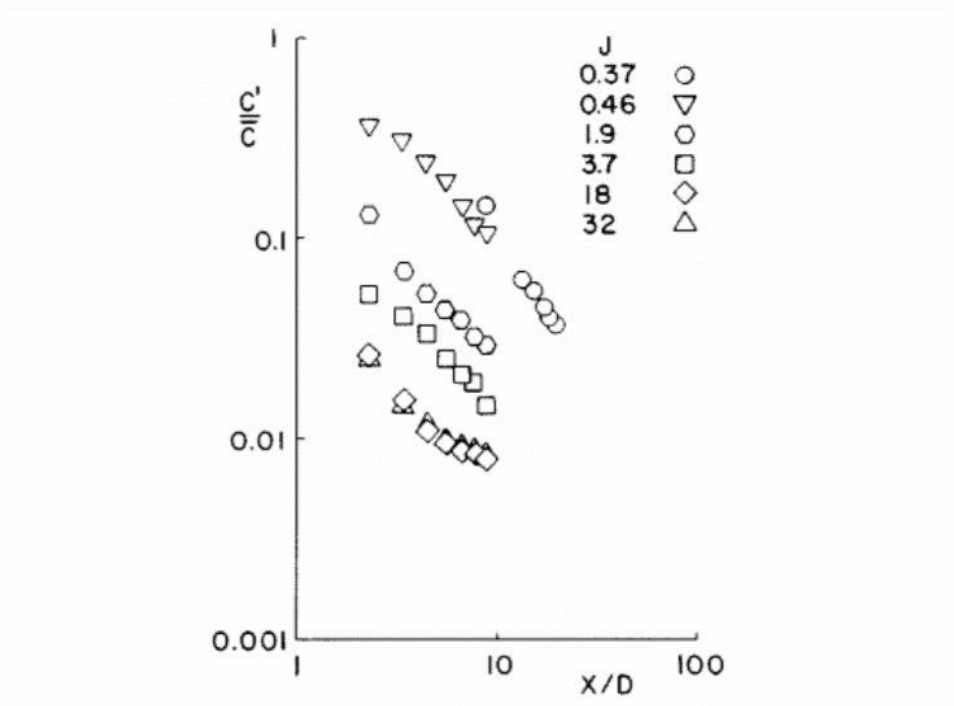

Figure 2.6: Concentration fluctuation as a function of the non-dimensional distance, x/D.

This data proves the relationship that increasing the momentum ratio results in better mixing. For hydrogen and oxygen with a stoichiometric mass flow ratio of 1:8 and with an estimated velocity ratio of 1:2, the momentum ratio is 32 when oxygen is the transverse jet fluid. From Figure 2.6 this correlates to a fluctuation concentration of around 0.01 after a length equal to 5 diameters. From this metric, it is evident that a transverse jet injection method would provide sufficient mixing for hydrogen and oxygen. However, this method needs to be modified slightly since the combustor will have an annular duct, not a completely open duct. The modification can be obtained, by taking the 2D configuration shown in Figure [x1] and revolving it about an offset horizontal axis. This yields a configuration like the image depicted below. In this image, the transverse jets become inward radial jets equally spaced along the circumference of the annulus.

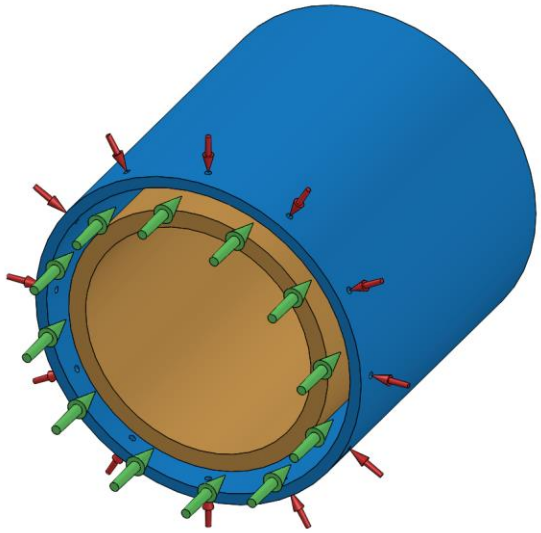

Figure 2.7: Annular duct of primary flow (green arrows) with inward radial jet injection (red arrows)

It is important to note that a true revolution of the 2D configuration would result in an injection slot instead of individual holes. The reason for this change is that it increases the amount of fluid interaction. A slot would only produce vortices on its upper and lower edges, while each individual hole will have shedding vortices in all directions. In general, high levels of vorticity in a flow is the best indication of two fluids mixing together; hence the desire to increase the number of vortices. The mixing can be further improved by adding opposing and perfectly offset holes that induce coaxial vortices.

Another requirement of the injectors is that each orifice needs to be choked. This refers to the flow being sonic at the exit of the orifice. Choked flow only occurs when the pressure before and after the orifice has pressure ratio of around 2. The reason for this stipulation stems from the large pressure rise associated with the detonation wave. With pressure on the order of 20 times the upstream pressure, there is a high possibility that reversed flow will occur. Back flow could cause the combustible mixture to enter either the hydrogen and oxygen manifolds, which may result in an explosion. By maintaining choked orifices for both fuel and oxidizer, the potential for back flow is reduced.

In order to control the point at which the flow is choked requires a distinct flow restriction, such as an orifice. The configuration in Figure 2.7 doesn’t include any possible choke point for the

primary flow. Thus, the annulus requires a front plate with distinct holes along the centerline diameter for the fuel injection. One challenge with this configuration is the hydrogen flow would necessitate fully developed flow before the oxygen is injected radially into the primary flow of hydrogen. The distance between the two points of injection would have to be at a minimum 3 times the height of the annular gap. While this configuration isn't impossible, it requires three individual manifolds; one for the hydrogen and one for each of the inner and outer oxygen inlet holes.

In an attempt to simplify the injection configuration, the idea to eliminate the primary axial flow entirely and instead utilize the inner radial injectors for fuel and the outer radial injectors for the oxidizer. A two-dimensional illustration of the coaxial vortices developed via perfectly offset radial injection is shown in Figure 2.8. According to the results from research conducted on fluid mixing via jets in a confined volume, the best mixing occurs from the largest possible vortices, defined by the geometry [6]. Due to the nature of an annulus, the maximum diameter of a vortex from a single jet is confined to be the same as the annular gap. Since the diameter of each vortex is roughly equivalent to the height of the annular gap, the ideal distance between the opposing jets would be the same as the annular height.

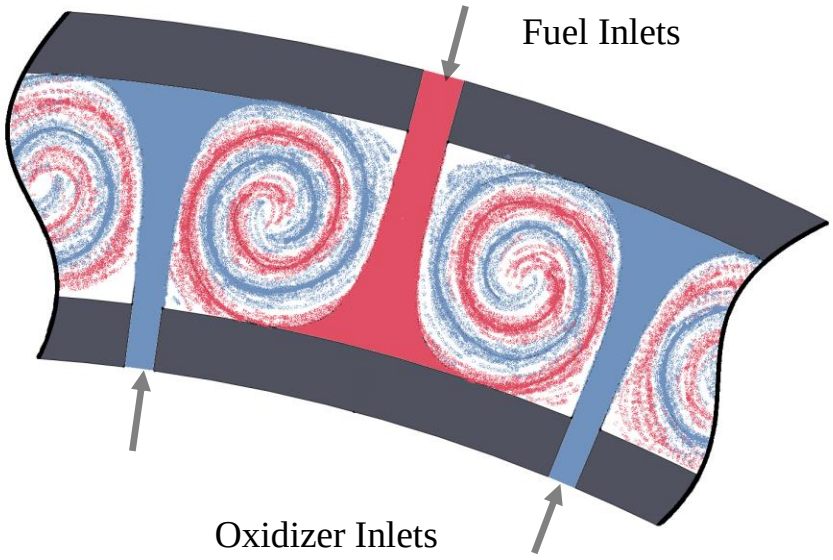

Figure 2.8: 2D illustration of coaxial vortices developed from perfectly offset radial injection.

To maintain the symmetry of the injections holes, the distance between injectors could not be chosen precisely. However, selecting 24 injection holes on each side, for a total of 48 injectors

separated by 7.5°, produced a distance between opposing injectors of 1.01 cm. This is 0.08% smaller than the height of the annular gap.

Using opposing radial injectors simplified the setup significantly and also had some benefits in terms of the mixing. Referring back to Figure 2.6, the concentration fluctuation is decreased as the momentum ratio is increased. By completely eliminating the primary flow, essentially the momentum ratio is infinite. While equation x2 no longer applies since J is an infinite value, the general trend of the data provided in Figure 2.6 conveys that this injection method should be an improvement over the mixing configuration involving a primary flow with transverse jet injection. Due to the lack of sufficient data on this specific flow configuration, mixing tests will be conducted to verify the capability of the injection configuration.

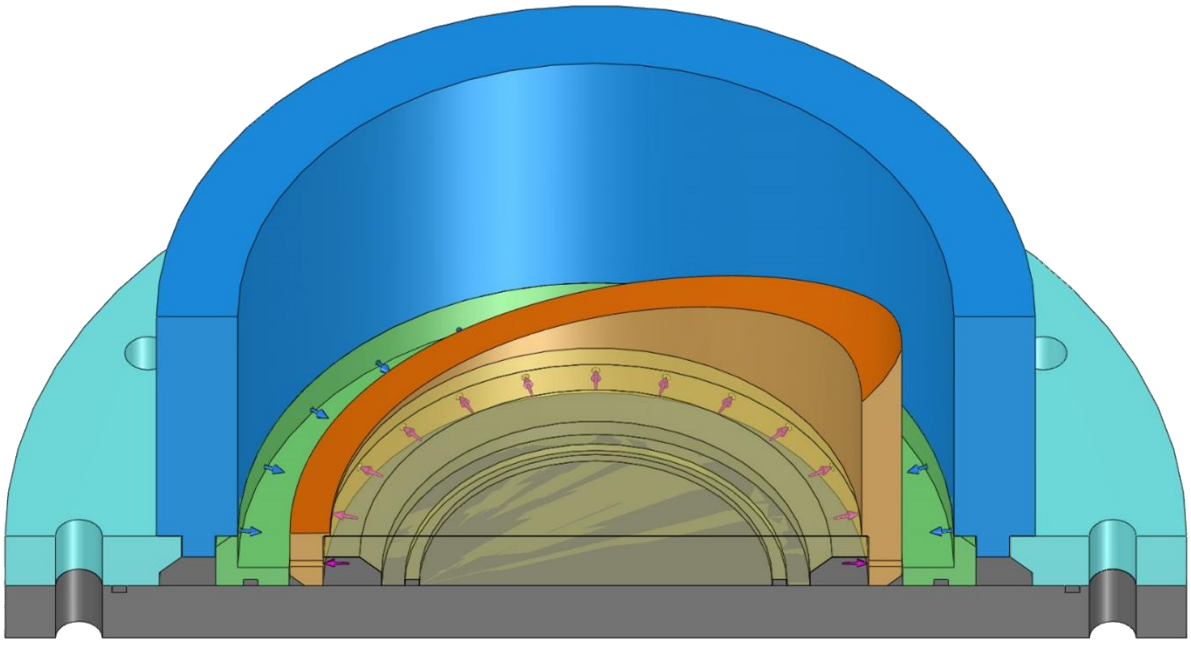

Figure 2.9: Cut-away view of final injection configuration with perfectly offset radial injectors indicated by the pink and blue arrows.

Another important aspect of the injection scheme is the size of each orifice. As previously mentioned, the flow out of each orifice needed to be sonic. The flow rate of an ideal compressed gas through a choked orifice is calculated from the following equation.

$$\dot{m} = \frac{AP_t}{N}\sqrt{\frac{\lambda}{T_t R}}\left(\frac{\lambda+1}{2}\right)^{-\frac{\lambda+1}{2(\lambda-1)}} \quad 2.13$$

In the equation, $\dot{m}$ represents the mass flow rate, A is the flow area, N is the number of holes, P_t and T_t are the manifold pressure and temperature, λ and R are the ratio of specific heats and gas constant for the particular the gas. By setting the operating mass flow rate with an associated pressure and temperature, the area of each orifice can be calculated. This rearranged equation is illustrated below.

$$A = \frac{\dot{m}N}{P_t}\sqrt{\frac{T_t R}{\lambda}}\left(\frac{\lambda+1}{2}\right)^{\frac{\lambda+1}{2(\lambda-1)}} \quad 2.14$$

Setting the mass flow rate of the oxidizer to 150 g/s for a manifold pressure and temperature of 1 MPa and 298 K and with 24 injection holes, the orifice diameter is 1.80 mm (0.071 inches) for each hole. Since the stoichiometric fuel to oxidizer mass flow rate ratio is 1:8, the input parameter for the mass flow rate of fuel is 18.75 grams per second. Utilizing the same inputs of 1 MPa and 298 K for the manifold pressure and temperature established a fuel orifice diameter of 1.27 mm (0.050 inches). Note that this calculations do not incorporate a discharge coefficient. The true flow area of each orifice will be smaller than the area determined in the calculations. Since mass flow tests will be conducted, the calculations were mainly used to get mass flow rates and associated pressures within a decent range of operation for the combustor. Figure 2.10 shown below, illustrates the calculated operating range of the injector flow system.

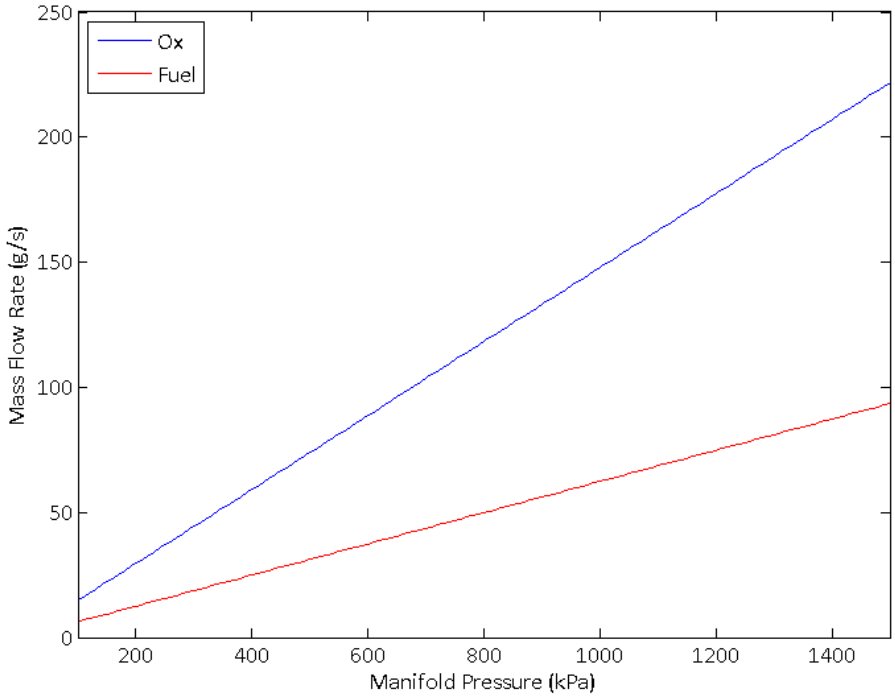

Figure 2.10: Mass flow rates of the oxidizer and fuel injectors based on orifice size.

Another important aspect to the injection system was the size of the oxygen and hydrogen manifolds and the number of inlets into these manifolds. The number of inlets to each of the manifolds was chosen to be four, since the current Shock Wave Reactor Lab plumbing already incorporated four lines. This implies that each entrance to the manifold provides flow to a quarter of the injectors, which is 6 holes. Sizing the cross-sectional area of the manifolds correctly ensures that all of the small injections holes into the annulus have an equivalent mass flow rate. To achieve this, the manifolds were oversized so that the cross-sectional area was at least 10 times larger than the total flow area of the holes. The summary of the injector and manifold sizing is given in the following table. Note the slight change in orifice size to match available drill sizes.

Table 2.3: Characteristics of injector

	Fuel	Oxidizer
Orifice Size	1.19 mm (0.047 in)	1.78 mm (0.070 in)
Cross-sectional Area of Manifold	94.6 mm² (0.146 in²)	98.1 mm² (0.152 in²)
Number of Injectors	24	24

2.2.4 *Flow System and Instrumentation*

Since the combustor was designed for use in the SWR, much of the flow system was already in place. The flow system involved source tanks for the fuel, oxidizer, and inert purge gases. The source for each of the gases was provided by compressed gas tanks pressurized anywhere from 600-2600 psi. The inert gases used were nitrogen, argon, and helium. Both the oxygen and hydrogen lines were plumbed with an inert gas line tee-ed in for easy transition between combustibles and inert gases. For the fuel and oxidizer lines, each line would pass through a flow regulator set to the desired pressure. They would then each pass through a Venturi style flow meter which measured the flow rate. After the flow meters, the oxygen and hydrogen lines split into four streams each and entered their respective manifolds. The pressure in these manifolds controlled the amount of flow of gas injected to the system. The hydrogen line was also plumbed with the ability to release any hydrogen leftover in the line to the roof of the building for safety reasons. After combustion in the annulus, the exhaust would travel down a long stretch of pipe and eventually into a dump tank held at vacuum pressure. The schematic in Figure 2.11 illustrates the flow system in its entirety.

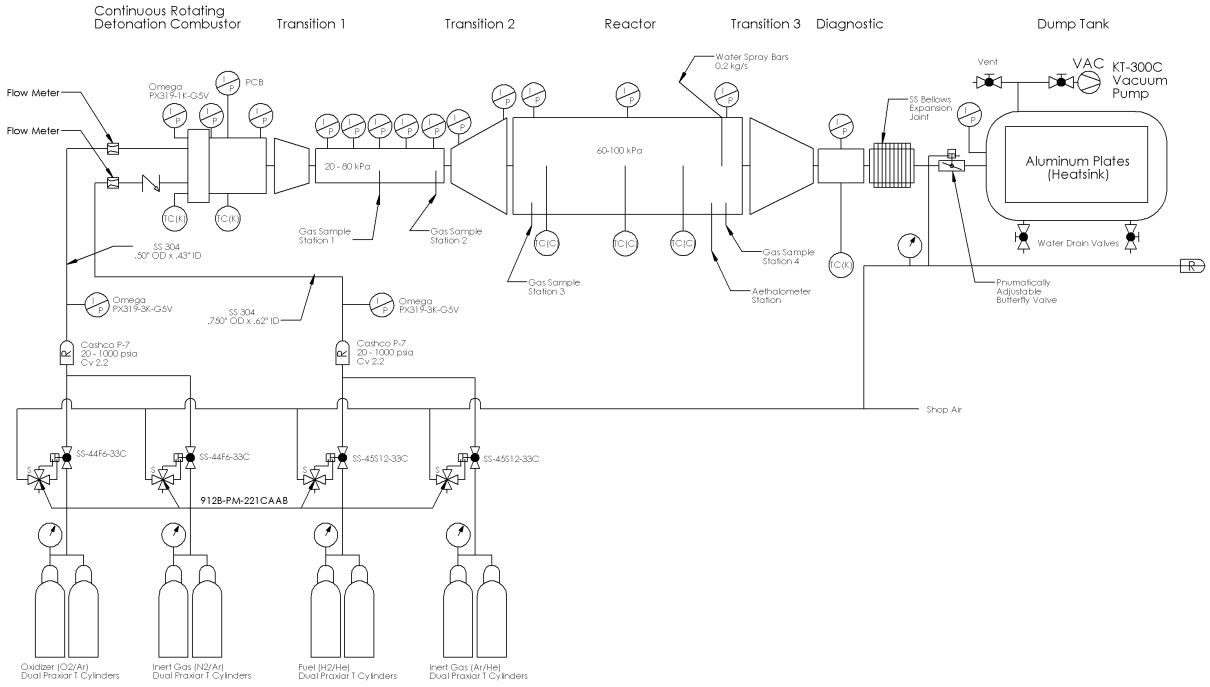

Figure 2.11: Schematic of the flow system for the combustor

A significant amount of instrumentation and sensors were utilized to acquire information about the combustion and gas flow. For more information on the exact models for the instrumentation as well as a larger flow system schematic please see Appendix 2.

2.3 Final Combustor Design

With all the major design factors considered, the final design was complete. An image of the 3D model designed in SolidWorks is illustrated below. Figure 2.13 on the following page, shows a cut-away view to show the combustor internals including the manifolds, injectors, and annular combustion chamber.

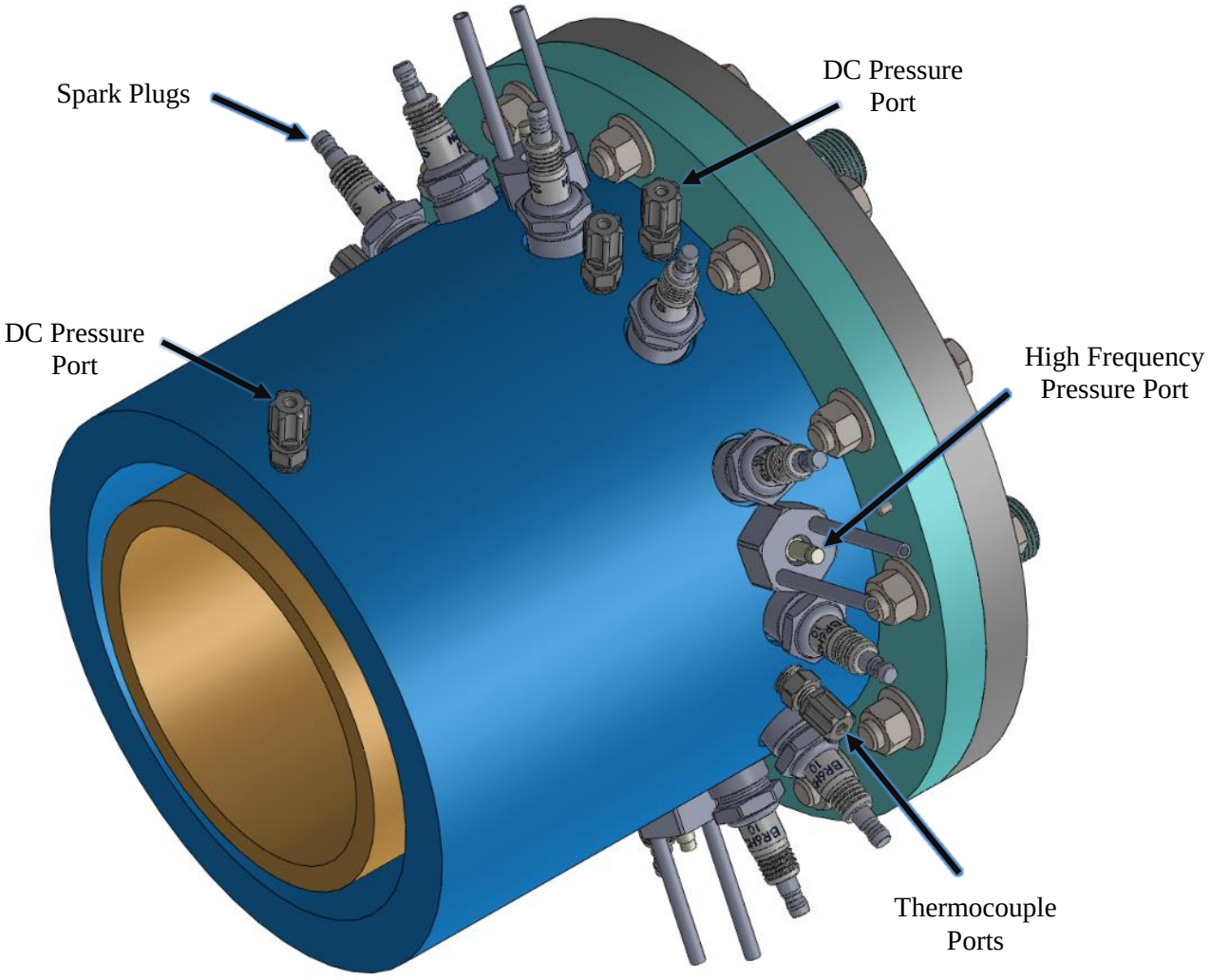

Figure 2.12: 3D model of the entire combustor.

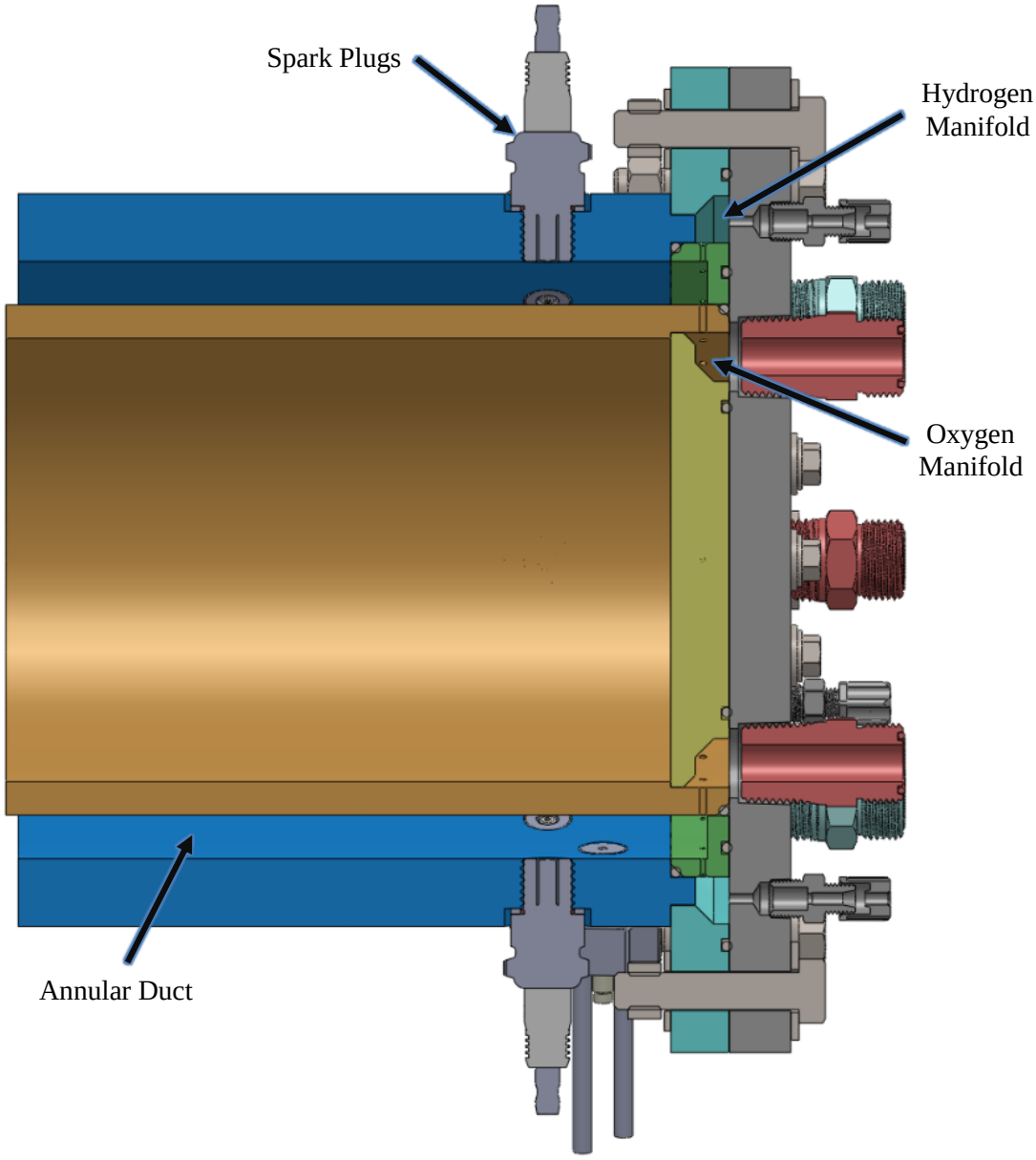

Figure 2.13: Cross section view of combustor design

Using the three dimensional CAD models, all of the parts were machined and welded. The following figures show the finished combustor and the individual parts. The drawings used to machine the parts can be found in Appendix C.

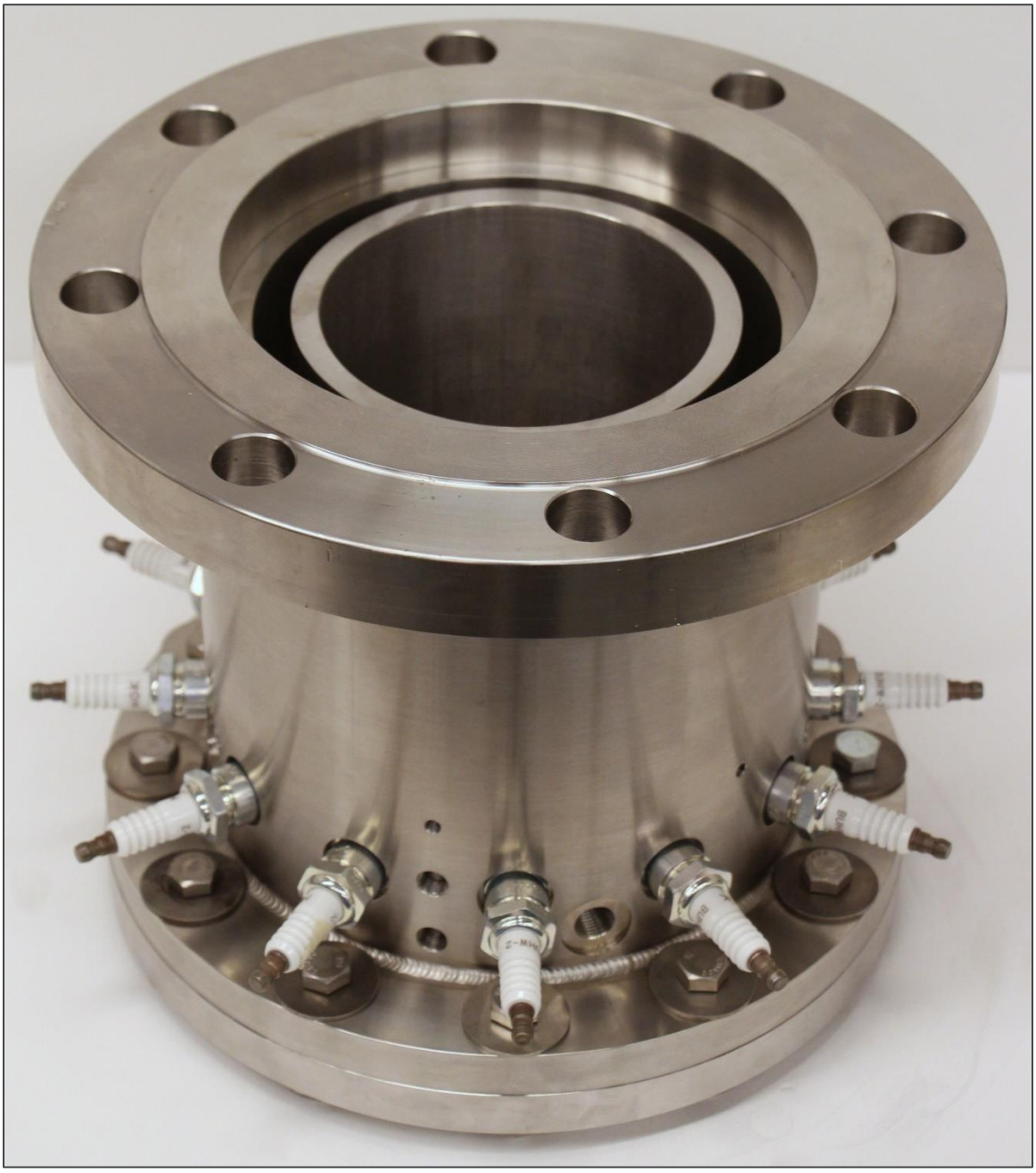

Figure 2.14: Assembled combustor with spark plugs attached

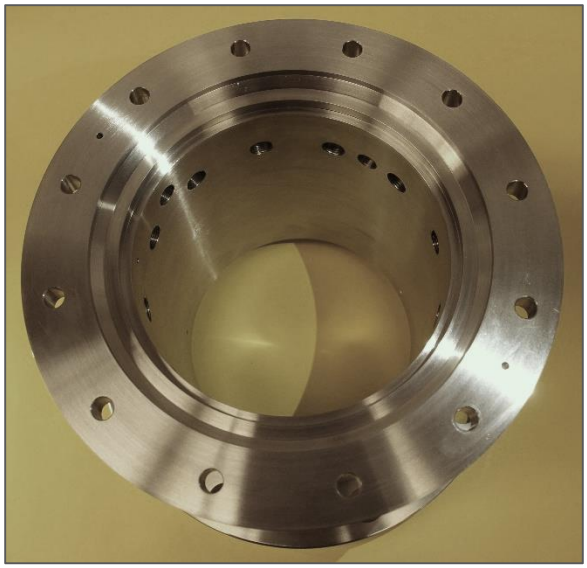

a) Outer Cylinder

b) Inner Cylinder

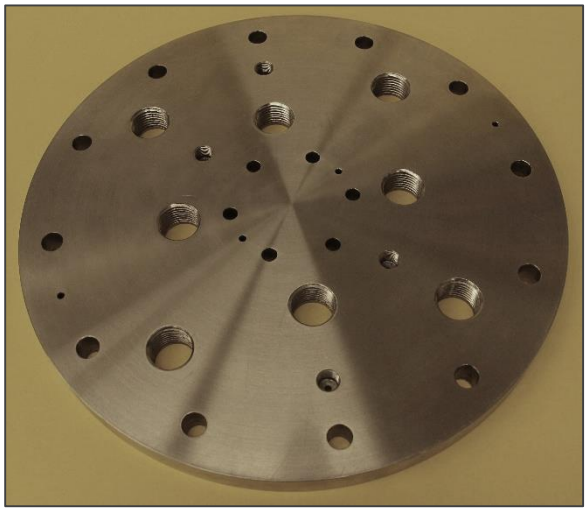

c) Back Plate

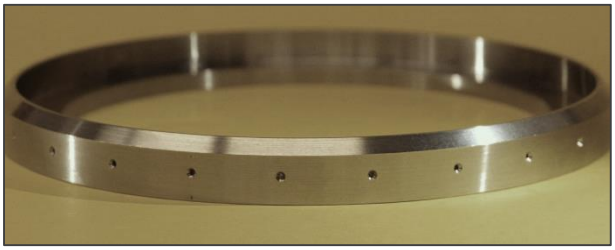

d) Injector Ring

Figure 2.15: Images of individual combustor parts.

Chapter 3. 2D ACOUSTIC NUMERICAL SIMULATION

In order to augment the experimental data of the wave controller, a simple 2D acoustic numerical simulation was created. The intent of the model was to visualize the interactions of the wave controller without factoring in the effect of combustion. This section outlines how the numerical model was developed as well as the different methods used to solve the equations.

3.1 NUMERICAL MODEL

In order to translate the experiment to a numerical simulation, the 2D acoustic wave equation in polar coordinates involving pressure was used. Each individual spark was modeled as a spike in pressure at one particular node. The sparking points were spread apart circumferentially at twelve points equally spaced. The partial differential equation is,

$$\frac{\partial^2 P}{\partial t^2} = a^2\left(\frac{1}{r}\frac{\partial}{\partial r}\left(r\frac{\partial P}{\partial r}\right)+\frac{1}{r^2}\frac{\partial^2 P}{\partial \theta^2}\right) \tag{3.1}$$

where P is the pressure, a is the speed of sound, r is the radius, θ is the angle from horizontal, and t is the time. The physical dimensions of the annulus used for testing the wave controller and other known data are defined as follows:

$$r_{inner} = 6.62\ cm, \qquad r_{outer} = 7.62\ cm, \qquad gap = 1\ cm$$
$$P_o = 101.3\ kPa, \qquad P_{spark} = 1.25 \cdot P_o, \qquad a = 347.18\ m/s$$

The interior and exterior boundary walls were modeled as “hard walls” meaning that any velocity component that hits the wall would be reflected at the same velocity and incident angle. This results in Von Neumann boundary conditions and is defined as,

$$\left(\frac{\partial P}{\partial r}\right)_{wall} = 0 \tag{3.2}$$

The next criteria for the model is the initial conditions. The first initial condition, t_0, all the values on the grid are set to P_o. At t_1, every point on the grid stays the same except for one exterior node located at $\theta = 0°$ and $r = r_{outer}$ set equal to P_{spark}. With the boundary and initial conditions defined, a numerical approximation of the acoustic wave equation can be determined. Two different numerical approximations were created to solve this time-variant problem to compare and contrast the results. The first scheme uses an explicit method and the second uses an implicit Crank-Nicolson method. The following sections will expound on these two methods.

3.1.1 *2nd Order Explicit Method*

The explicit method to solve each time step uses a 2nd order finite difference for the derivatives with respect to time and theta. The derivative with respect to the radius is also a 2nd order finite difference, but it slightly different in its creation. The following equations show the finite difference approximations.

$$\frac{\partial^2 P}{\partial t^2} = \frac{P_{i,j}^{k+1} - 2P_{i,j}^{k} + P_{i,j}^{k-1}}{\Delta t^2} \tag{3.3}$$

$$\frac{1}{r}\frac{\partial}{\partial r}\left(r\frac{\partial P}{\partial r}\right) = \frac{r_{i+\frac{1}{2}}\left(P_{i+1,j}^{k} - P_{i,j}^{k}\right) - r_{i-\frac{1}{2}}\left(P_{i,j}^{k} - P_{i-1,j}^{k}\right)}{r_i\,\Delta r^2} \tag{3.4}$$

$$\frac{1}{r_i^2}\frac{\partial^2 P}{\partial \theta^2} = \frac{P_{i,j+1}^{k} - 2P_{i,j}^{k} + P_{i,j-1}^{k}}{r_i^2 \Delta\theta^2} \tag{3.5}$$

$$r\colon\ i = 1 \to m, \qquad \theta\colon\ j = 1 \to n, \qquad t\colon\ k = 1 \to t_f$$

Combining and solving for the pressure at the next time step yields,

$$P_{i,j}^{k+1} = 2P_{i,j}^{k} - P_{i,j}^{k-1} + (a\Delta t)^2\left(\frac{r_{i+\frac{1}{2}}\left(P_{i+1,j}^{k} - P_{i,j}^{k}\right) - r_{i-\frac{1}{2}}\left(P_{i,j}^{k} - P_{i-1,j}^{k}\right)}{r_i\,\Delta r^2} + \frac{P_{i,j+1}^{k} - 2P_{i,j}^{k} + P_{i,j-1}^{k}}{r_i^2\Delta\theta^2}\right) \tag{3.6}$$

This equation applies to all the spatial interior nodes, which includes all j components and i components such that, $i = 2 \to m - 1$. For the boundary condition, the finite differencing looks like,

$$\left(\frac{\partial P}{\partial r}\right)_{i=1} = \frac{3P_{1,j}^{k+1} - 4P_{2,j}^{k+1} + P_{3,j}^{k+1}}{2\Delta r} = 0 \tag{3.7}$$

$$\left(\frac{\partial P}{\partial r}\right)_{i=m} = \frac{3P_{m,j}^{k+1} - 4P_{m-1,j}^{k+1} + P_{m-2,j}^{k+1}}{2\Delta r} = 0 \tag{3.8}$$

Using these boundary equations, the interior and exterior nodes can be obtained.

$$P_{1,j}^{k+1} = \frac{4P_{2,j}^{k+1} - P_{3,j}^{k+1}}{3} \tag{3.9}$$

$$P_{m,j}^{k+1} = \frac{4P_{m-1,j}^{k+1} - P_{m-2,j}^{k+1}}{3} \tag{3.10}$$

The explicit method is quite simple to implement, but it does have its downsides. The first major problem is that it is highly dependent on the ratio between the spatial and time step sizes. This ratio is called the CFL number and has been defined as

$$CFL = \left(\frac{a\Delta t}{\Delta r}\right)^2 < 1 \; for \; Stability \tag{3.11}$$

The CFL number is what determines the stability of the method and must be less than 1 to maintain stability. This is limiting because in order to maintain high spatial resolution, the time step is miniscule – on the order of 1 microsecond. For this particular application the time step isn't as crucial since the elapsed time is on the order of 10 microseconds. Despite this, a different approach that isn't as dependent on the CFL will also be implemented.

3.1.2 *Implicit Crank-Nicolson*

This method is a slight modification of the same finite differencing methods outlined in the previous section. How it differs is that it introduces additional $(k+1)$ terms, requiring an implicit solution. The basis of the method is defined by the following,

$$\frac{\partial^2 u}{\partial t^2} = F\left(u, x, t, \frac{\partial u}{\partial x}, \frac{\partial^2 u}{\partial x^2}\right) \tag{3.12}$$

$$\frac{u_{i,j}^{k+1} - 2u_{i,j}^{k} + u_{i,j}^{k-1}}{\Delta t^2} = F_i^k\left(u, x, t, \frac{\partial u}{\partial x}, \frac{\partial^2 u}{\partial x^2}\right) \quad (forward \; Euler) \tag{3.13}$$

$$\frac{u_{i,j}^{k+1} - 2u_{i,j}^{k} + u_{i,j}^{k-1}}{\Delta t^2} = F_i^{k+1}\left(u, x, t, \frac{\partial u}{\partial x}, \frac{\partial^2 u}{\partial x^2}\right) \quad (backward \; Euler) \tag{3.14}$$

$$\frac{u_{i,j}^{k+1} - 2u_{i,j}^{k} + u_{i,j}^{k-1}}{\Delta t^2} = \frac{1}{2}\left[F_i^{k+1}\left(u, x, t, \frac{\partial u}{\partial x}, \frac{\partial^2 u}{\partial x^2}\right) + F_i^{k}\left(u, x, t, \frac{\partial u}{\partial x}, \frac{\partial^2 u}{\partial x^2}\right)\right] \tag{3.15}$$

Applying this to the acoustic wave equation and combining like terms yields,

$$P_{i,j}^{k+1} - \frac{(a\Delta t)^2}{2}F^{k+1} = 2P_{i,j}^{k} - P_{i,j}^{k-1} + \frac{(a\Delta t)^2}{2}F^{k} \tag{3.16}$$

$$where, \qquad F^k = \frac{r_{i+\frac{1}{2}}\left(P_{i+1,j}^{k} - P_{i,j}^{k}\right) - r_{i-\frac{1}{2}}\left(P_{i,j}^{k} - P_{i-1,j}^{k}\right)}{r_i \, \Delta r^2} + \frac{P_{i,j+1}^{k} - 2P_{i,j}^{k} + P_{i,j-1}^{k}}{r_i^2 \Delta\theta^2}$$

This makes it possible to form a matrix equation of the following form,

$$AP^{k+1} = BP^{k} - I_x P^{k-1} \tag{3.17}$$

Where the input parameters are defined by the following,

$$P = [\, P_{11} \ldots P_{m1}\, P_{12} \ldots P_{m2} \;\ldots\; P_{1n} \;\ldots\; P_{mn}]^T \tag{3.18}$$

$$A = \begin{pmatrix} T & S & 0 & \cdots & 0 & S \\ S & T & S & \ddots & \ddots & 0 \\ 0 & \ddots & \ddots & \ddots & \ddots & \vdots \\ \vdots & \ddots & \ddots & \ddots & \ddots & 0 \\ 0 & \ddots & \ddots & S & T & S \\ S & 0 & \cdots & 0 & S & T \end{pmatrix}_{N\,x\,N} \qquad B = \begin{pmatrix} U & S & 0 & \cdots & 0 & S \\ S & U & S & \ddots & \ddots & 0 \\ 0 & \ddots & \ddots & \ddots & \ddots & \vdots \\ \vdots & \ddots & \ddots & \ddots & \ddots & 0 \\ 0 & \ddots & \ddots & S & U & S \\ S & 0 & \cdots & 0 & S & U \end{pmatrix}_{N\,x\,N}$$

Where T, U, and S are sub-matrices. The size of both A and B are NxN, where $N = mn$. The sub-matrices are further defined as,

$$T = \begin{pmatrix} 3 & -4 & 1 & 0 & \cdots & 0 \\ -b_i & 1-a_i & -c_i & 0 & \cdots & \vdots \\ 0 & \ddots & \ddots & \ddots & \ddots & \vdots \\ \vdots & \ddots & \ddots & \ddots & \ddots & 0 \\ \vdots & \ddots & 0 & -b_i & 1-a_i & -c_i \\ 0 & \cdots & 0 & 1 & -4 & 3 \end{pmatrix}_{m\,x\,m}$$

$$U = \begin{pmatrix} 0 & 0 & 0 & \cdots & 0 \\ b_i & 2+a_i & c_i & 0 & \vdots \\ 0 & \ddots & \ddots & \ddots & 0 \\ \vdots & 0 & b_i & 2+a_i & c_i \\ 0 & \cdots & 0 & 0 & 0 \end{pmatrix}_{m\,x\,m} \qquad S = \begin{pmatrix} 0 & 0 & \cdots & \cdots & 0 \\ 0 & -d_i & \ddots & \ddots & \vdots \\ \vdots & \ddots & \ddots & \ddots & \vdots \\ \vdots & \ddots & \ddots & -d_i & 0 \\ 0 & \cdots & \cdots & 0 & 0 \end{pmatrix}_{m\,x\,m}$$

Where,

$$a_i = \frac{(a\Delta t)^2}{2}\left(\frac{r_{i+\frac{1}{2}} + r_{i-\frac{1}{2}}}{r_i \Delta r^2} - \frac{2}{(r_i \Delta\theta)^2}\right) \quad b_i = \frac{r_{i-\frac{1}{2}}}{2r_i}\left(\frac{a\Delta t}{\Delta r}\right)^2 \quad c_i = \frac{r_{i+\frac{1}{2}}}{2r_i}\left(\frac{a\Delta t}{\Delta r}\right)^2 \quad d_i = \frac{1}{2}\left(\frac{a\Delta t}{r_i \Delta\theta}\right)^2$$

While this may look convoluted, it is actually fairly straight forward. The matrix T is quasi-tri-diagonal and corresponds to a radial line of grid points at one particular theta. The top and bottom rows of T correspond to the same boundary condition expressed in the explicit method explanation. The matrix U is almost identical to T; the only exceptions are the positive values on a_i, b_i, and c_i, and that the top and bottom rows are zero, to ensure the right hand side of the equation is zero for all the boundary conditions. The S matrix are the contributions of nodes in

the $\Delta\theta$ direction with respect to the center node. The last portion to be defined is the modified identity matrix. Since the RHS of the equation needs to satisfy the boundary equations, the top and bottom rows of the sub-matrix, I_{mod}, are all zeros.

$$I_x = \begin{pmatrix} I_{mod} & 0 & \cdots & 0 \\ 0 & \ddots & \ddots & \vdots \\ \vdots & \ddots & \ddots & 0 \\ 0 & \cdots & 0 & I_{mod} \end{pmatrix}_{NxN} \qquad I_{mod} = \begin{pmatrix} 0 & 0 & \cdots & \cdots & 0 \\ 0 & 1 & 0 & \ddots & \vdots \\ \vdots & \ddots & \ddots & \ddots & \vdots \\ \vdots & \ddots & 0 & 1 & 0 \\ 0 & \cdots & \cdots & 0 & 0 \end{pmatrix}_{m\,x\,m}$$

Since the matrix equation (equation 2) has all unknowns P^{k+1} on the left hand side and known values on the right, the solution can be obtained by either Gaussian elimination or some iterative methods such as Jacobi, Conjugate Gradient, or SOR.

$$P^{k+1} = A^{-1}(BP^k - I_x P^{k-1}) \qquad 3.19$$

The benefit to using the implicit method is that the relation between the time step and the spatial step are slightly relaxed. While it is still affected by the CFL number, it isn't necessary for stability. However, a large CFL number will result in numerical inaccuracies. With both explicit and implicit methods derived, a numerical solution can be obtained.

3.2 NUMERICAL SIMULATION RESULTS

In applying the numerical model, several different grid sizes were used. The following figure depicts these grids. The data corresponding to the values that produce the plots are described in Table 1.

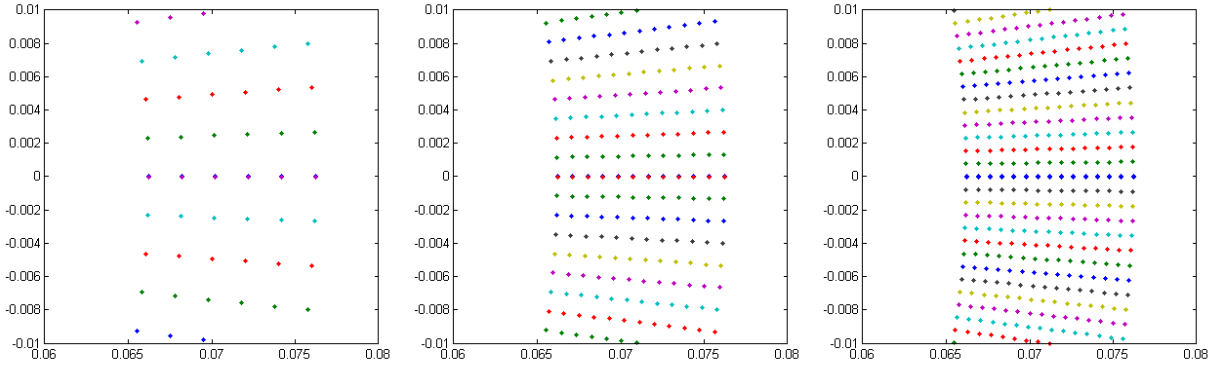

Figure 3.1: Plots of the mesh points (zoomed in) for the coarse, medium, and fine grids.

As for the time resolution, it varied for the explicit and implicit methods. Table 2, shown below, describes the different time steps utilized for each mesh size. Using this criteria, the results for both the explicit and implicit methods were obtained.

Table 3.1: Spatial mesh grid data

Mesh	Δr (m)	m	$\Delta\theta$ (rad)	n	Nodes
Coarse	2e-3	6	3.51e-2	180	1,080
Medium	9.09e-4	12	1.75e-2	360	4,320
Fine	7.14e-4	15	1.17e-2	540	8,100

Table 3.2: Time data based on the spatial mesh grid

	Explicit			Implicit					
Mesh	CFL	Δt (s)	n_t	CFL	Δt (s)	q	CFL	Δt (s)	n_t
Coarse	0.5	4.07e-6	200	2	8.15e-6	200	5	1.29e-5	200
Medium	0.5	1.85e-6	150	2	3.70e-6	100	5	5.85e-6	150
Fine	0.5	1.45e-6	100	2	2.91e-6	50	5	4.60e-6	100

3.2.1 *Explicit Method Solution*

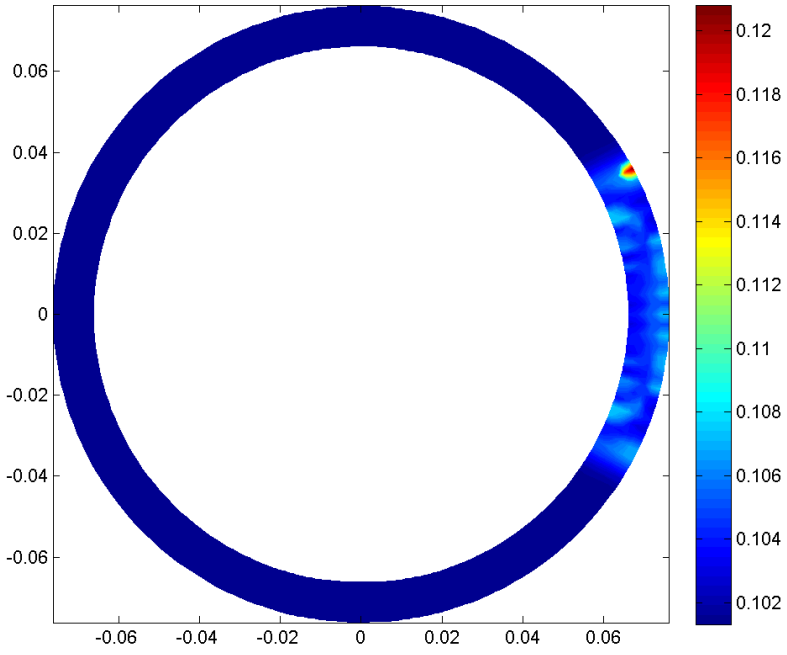

Figure 3.2: Coarse mesh solution at t = 0.13 milliseconds. The color bar units of pressure are in MPa.

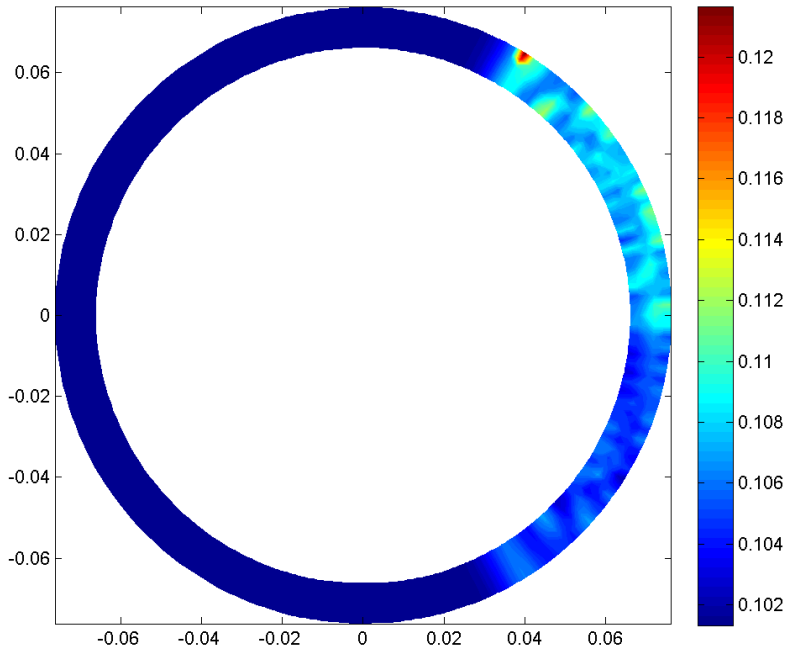

Figure 3.3: Coarse mesh solution at t = 0.24 milliseconds. Units are in MPa.

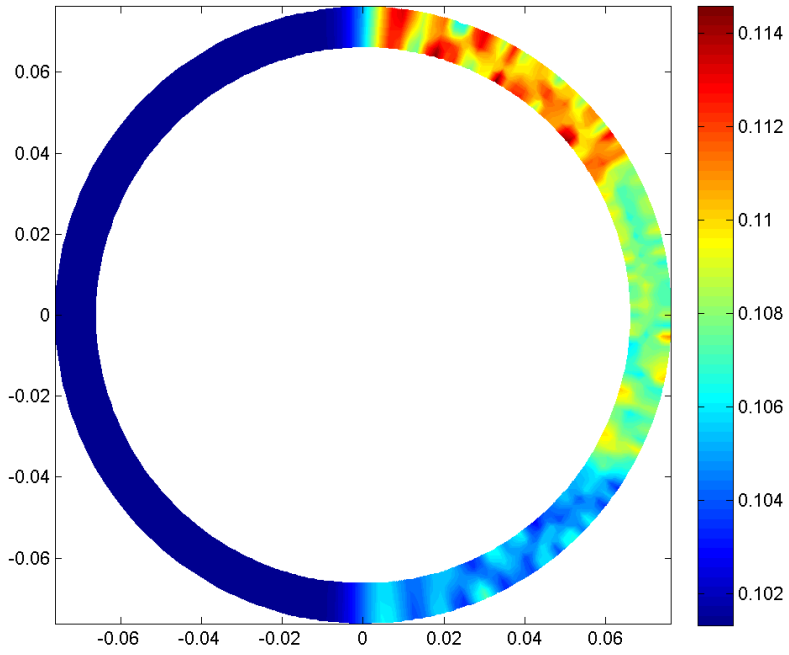

Figure 3.4: Coarse mesh solution at t = 0.34 milliseconds. Units are in MPa.

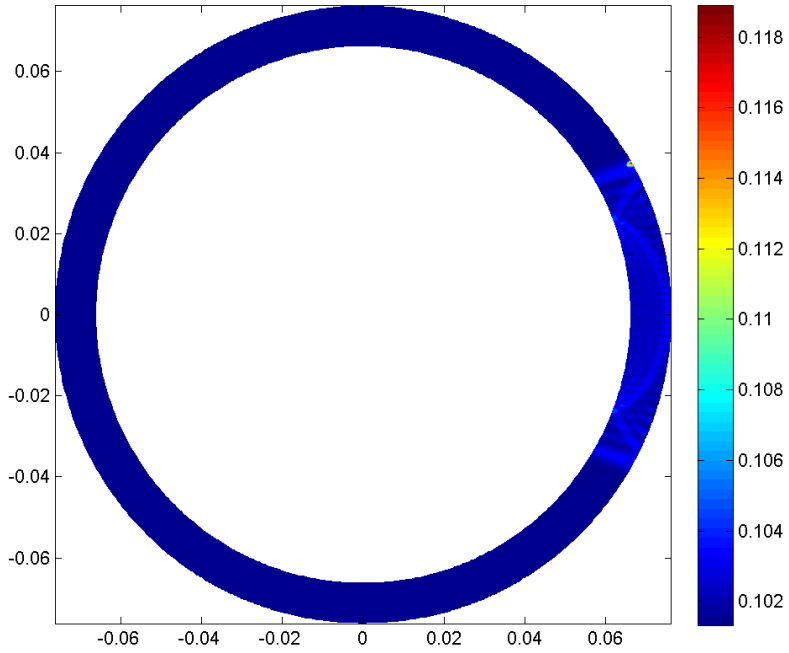

Figure 3.5: Fine mesh solution at t = 0.12 milliseconds. Units are in MPa.

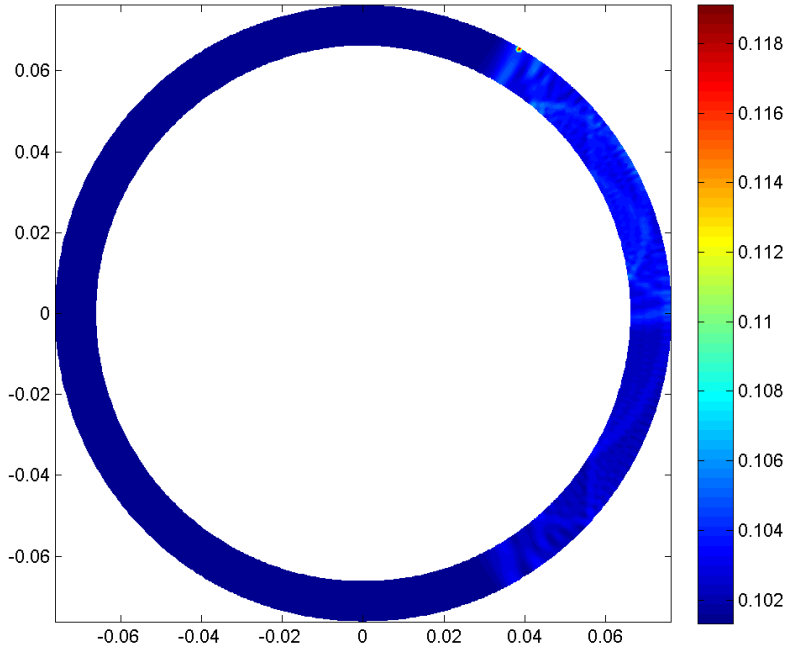

Figure 3.6: Coarse mesh solution at t = 0.24 milliseconds. Units are in MPa.

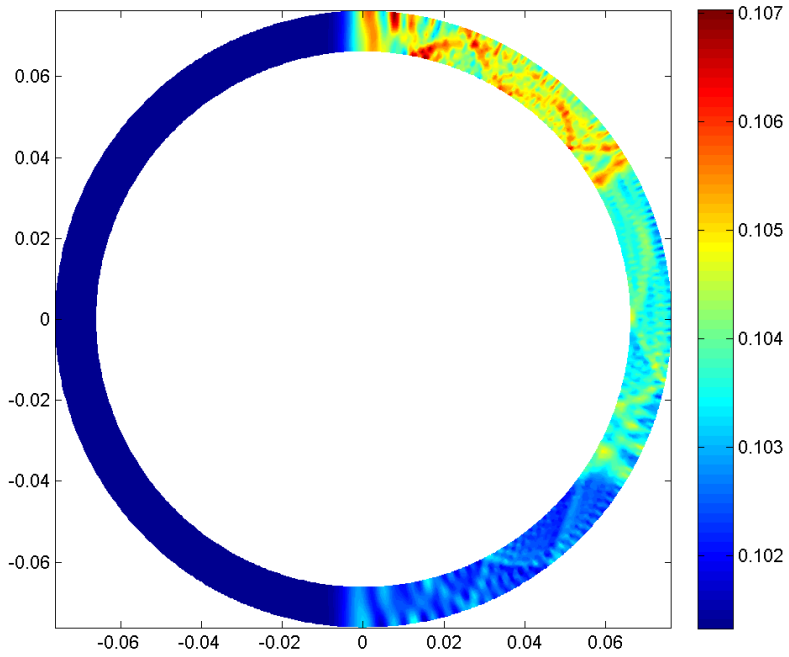

Figure 3.7: Fine mesh solution at t = 0.34 milliseconds. Units are in MPa.

3.2.2 *Implicit Method Solution*

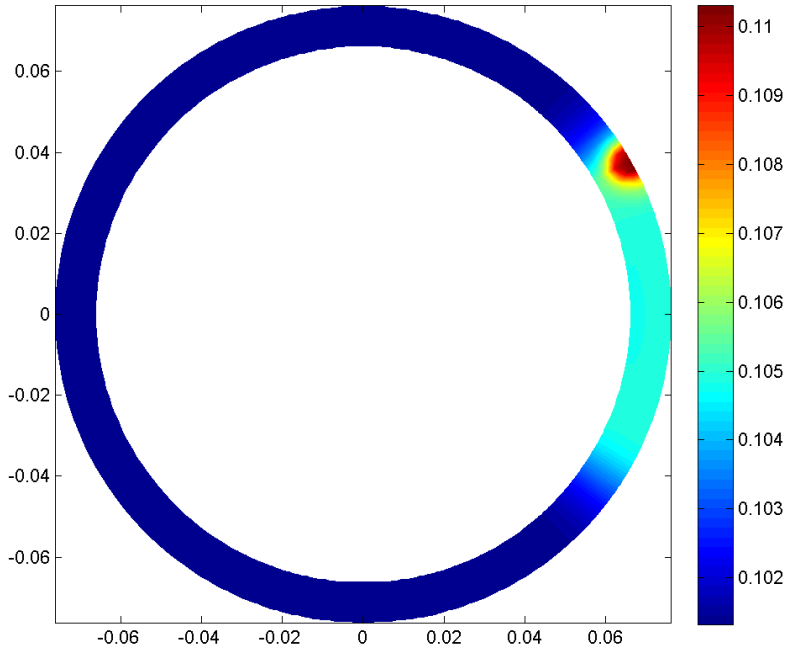

Figure 3.8: Plot of coarse solution with CFL = 2 at t = 0.14 milliseconds. Units are in MPa.

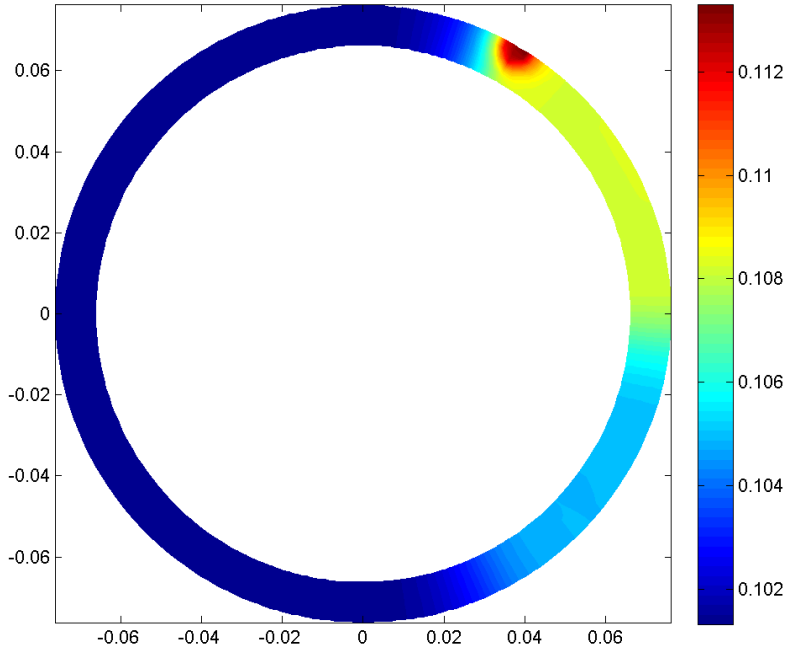

Figure 3.9: Plot of coarse solution with CFL = 2 at t = 0.25 milliseconds. Units are in MPa.

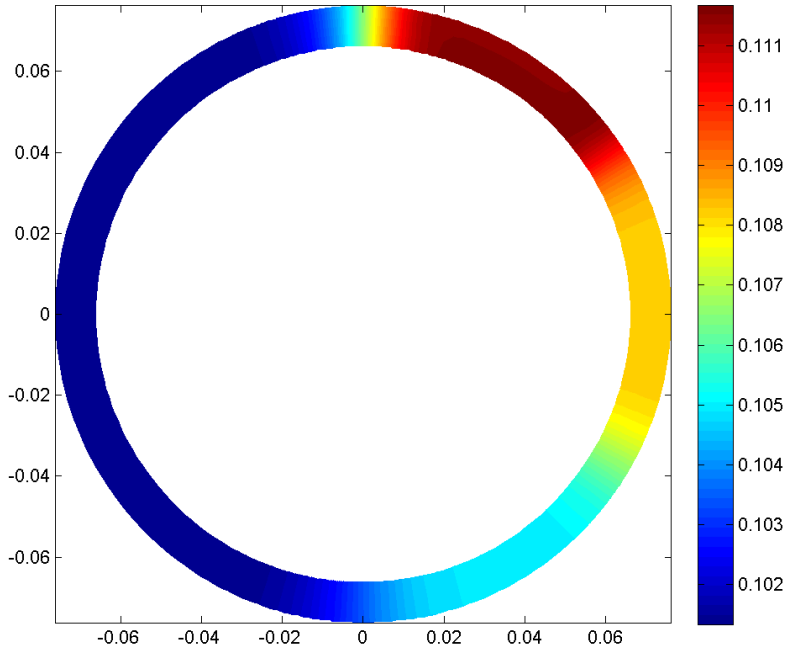

Figure 3.10: Plot of coarse solution with CFL = 2 at t = 0.34 milliseconds. Units are in MPa.

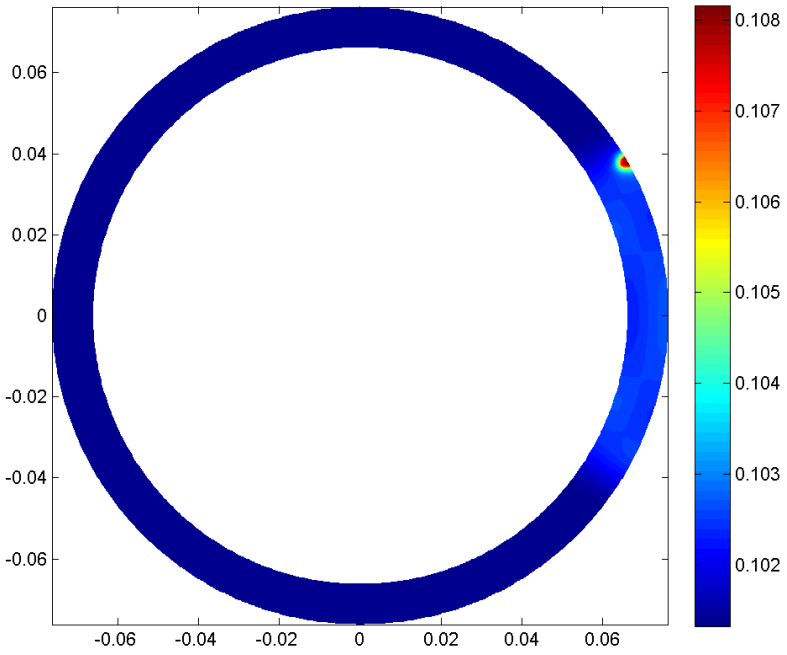

Figure 3.11: Fine mesh solution with CFL = 2 at t = 0.12 milliseconds. Units are in MPa.

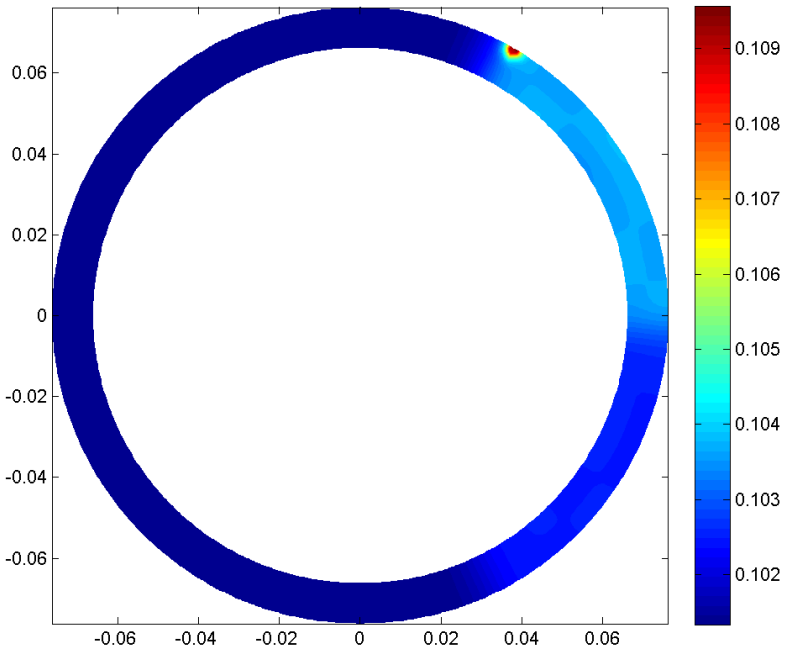

Figure 3.12: Fine mesh solution with CFL = 2 and t = 0.24 milliseconds. Units are in MPa

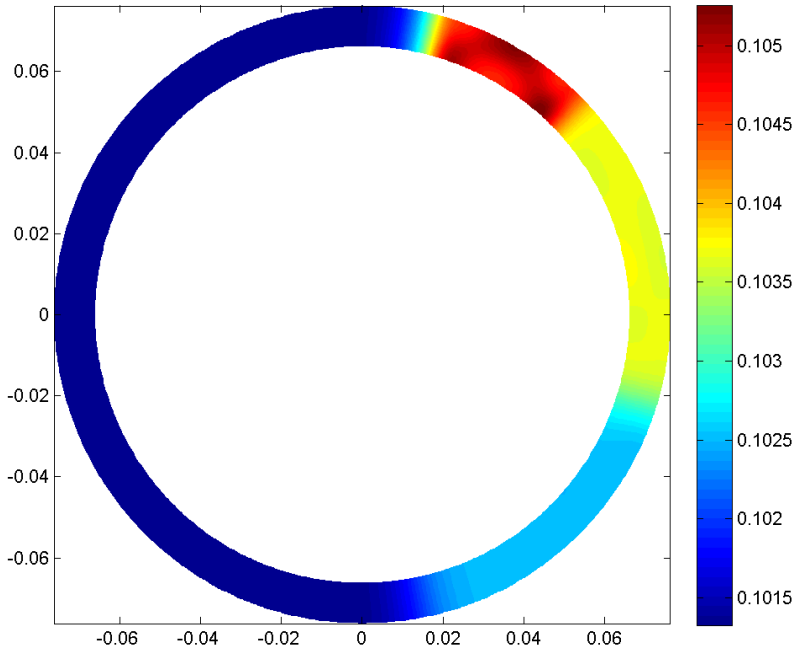

Figure 3.13: Fine mesh solution with CFL = 2 and t = 0.29

3.2.3 *Simulation Analysis*

From the plots above, it can easily be seen that the there is a strong transverse wave traveling inside the annular duct. Each pressure spike creates waves going in both directions, but since one of the directions is consistently being added upon with consecutive pressure spikes, this direction (counter-clockwise) is more powerful. One of the main purposes of using both an explicit and implicit method for solving this time-variant problem was to compare the how efficiently and accurately each of them solved the problem. In terms of efficiency, it seems that the explicit method is on par with the implicit method, which is somewhat surprising. The time required to complete the calculation for all the iterations is shown here in Table 3.

Table 3.3: Time for calculation of all nodes after all iterations

	Explicit	Implicit
Mesh	Time (sec)	Time (sec)
Coarse	0.5559	0.8369
Medium	3.9335	2.9901
Fine	4.2406	5.9012

In terms of the visual representation of the data, the explicit method seemed to capture more of the minute reflections and smaller transverse travelling waves. The implicit solution seems to show more of a damping effect of when the pressure wave interacts with the opposite wall. This appears to fall in line more with the actual progression of the wave in an annular duct since the reflected waves would die out much quicker than the circumferentially spinning wave.

Chapter 4. EXPERIMENTAL SETUP AND PROCEDURE

Testing the combustor required multiple experimental setups. Each setup helped evaluate different components of the overall system. The main focus of the research was to develop a continuous rotating combustor and determine the effectiveness of the wave controller. In addition to this, the combustor design incorporated a simpler method of mixing which required validation. Following these initial subsystem tests, the overall hot-fire combustion test would be conducted. Due to the length of the preliminary tests, the combustion tests will not be included in this body of work. The following sections further discuss each of the experimental setups to prepare the combustor for hot-fire testing.

4.1 WAVE CONTROLLER ACOUSTIC TESTING

In order to experiment with the wave controller, a separate annular duct was built. This device emulated the basic geometry of the actual combustion chamber but allowed for viewing of the sparks by keeping the annulus open on both axial ends. It didn't incorporate injection of fuel and oxidizer. The test was created solely to examine the acoustic waves produced by the spark plugs. A picture of the annular duct with the spark plugs connected is shown below.

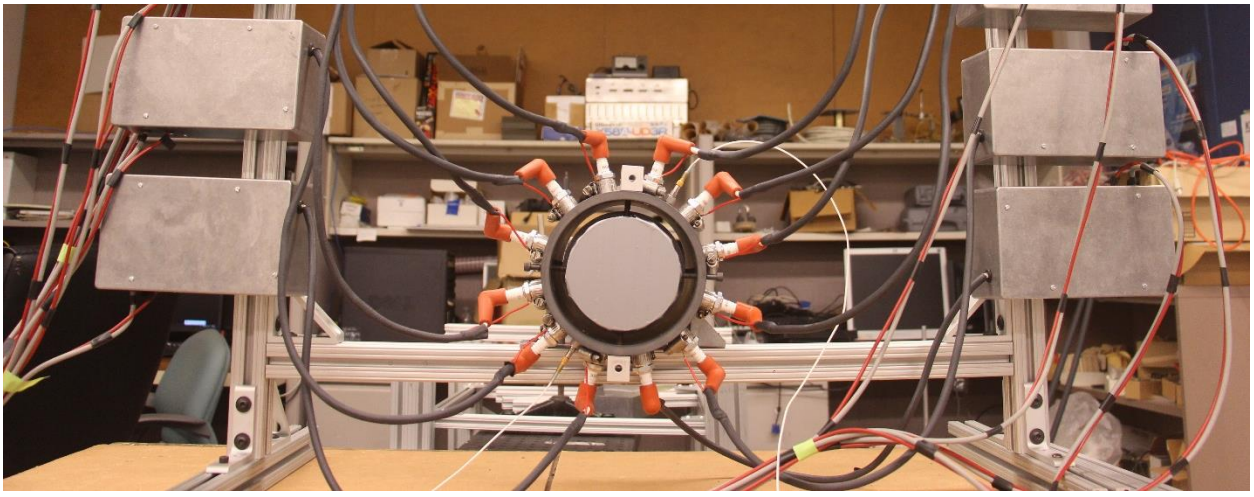

Figure 4.1: Picture of the annular duct and spark plug array for testing of the wave controller.

The acoustic duct was constructed from two PVC pipes. The inner pipe was constrained by eight radial set screws connected to the larger pipe. Since slightly modified pipe was used, the

dimensions weren't exactly the same as the stainless steel version of the combustor. The dimensions for the plastic annular duct are described in table below.

Table 4.1: Dimensions of plastic annular duct in centimeters (inches)

d_i	13.24 (5.21)
d_o	15.24 (6.00)
h	1.00 (0.39)

Since these acoustic waves travel at the speed of sound, the only way to witness the motion required the use of a high speed camera and an optical setup. A schematic depicting the setup for the experiment utilizing the high speed camera is illustrated in Figure 4.2. The optical setup used a high energy point-source light aligned at the focal point of large lens. The purpose of the lens was to collimate the light to shine through the annular duct. After the light passed through the duct, it was re-focused by another lens into a high-speed Phantom camera. When the spark plug array is switched on, the generated acoustic waves effect the density of the medium they are traveling through. As the light passes through the acoustic waves, the density gradients can be differentiated since the index of refraction varies with changing density. Due to the limits of the high-speed camera, at the highest frame rate achievable, the resolution was very small: 120 x 240 pixels. This only allowed for visualization of a small section of the annulus. This section was large enough to view one spark plug and its acoustic waves in the annulus. The camera was capable of recording up to 2 seconds at the highest speed of 240,000 frames per second. This provides plenty of time to see the rotating waves because of the waves' high speed. An acoustic wave in the annular duct would make 760 rotations in a single second. Therefore in only 2.6 milliseconds the wave will have made 2 full revolutions in the annulus.

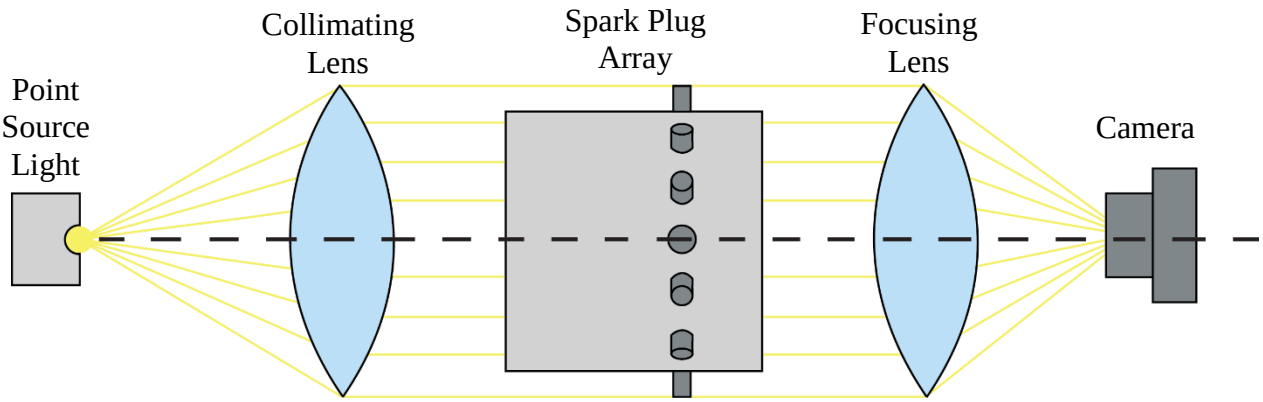

Figure 4.2: Schematic of the experiment while using the Phantom high speed camera.

Due to the resolution limits at the frame rates necessary to catch the moving acoustic waves, another idea on how to image the acoustic waves was conceived. The new method used nearly the exact same setup as the one depicted in Figure 4.2. In place of the always-on light, a device called a spark gap was used. The spark gap produced a very bright light for only 0.5 microseconds; essentially a very brief flash. The short duration of light made it possible to take a high resolution still image of the entire annulus using a basic DSLR. In order to time the flash of the spark plug to the precise moment of capture on the camera, the spark gap was wired to the external flash output of the DSLR. With this combination, 16MP still images of the entire annulus were captured.

With both of these methods to acquire image data, the testing of the wave controller was carried out. The main variables of the testing were the sparking input frequency and the sparking energy. While the input frequency was easily adjustable from 100 Hz to 20 kHz, the main region of interest was near the 9.12 kHz frequency. The reason, as mentioned in the design section, is that this frequency corresponded to a single rotation of a wave moving at the speed of sound in air. Therefore, the bulk of the data was taken using this frequency as input for the wave controller. Another area of control was the energy emitted by each spark. This was varied slightly by changing the input voltage of the power supply anywhere from 80-190 volts. At 150 volts, the amount of energy input from each spark was about 20 millijoules.

4.2 MIXING TESTS

In the design of the combustor, a new injection method was introduced in an attempt to enhance the mixing of the fuel and oxidizer. Therefore, the effectiveness of the mixing needed to be verified. Two separate tests were developed to determine the mixing efficiency. The first experiment used flow visualization within a water tunnel, while the second test was performed on the designed combustor using inert gases.

4.2.1 *Subsonic Water Tunnel Visualization*

As the combustor was being developed, a separate team was tasked with designing a flow visualization experiment that mimicked the injection scheme of the engine. The team of

undergraduate students included Trever Byrd, Ben Greaves, Sean Phenisee, and LongJi Yan. Instead of using gases, the team used a pH titration method of two liquids. The two liquids used were hydrochloric acid and a mixture of sodium hydroxide and phenolphthalein. The chemical reaction is detailed by the following chemical equation.

$$HCl + NaOH \rightarrow H_2O + NaCl \quad (4.1)$$

The combination of the acid and base produced a neutral solution of water and table salt. The phenolphthalein's magenta color makes it possible to visualize the interaction. When the mixture of sodium hydroxide and phenolphthalein reacts with the hydrochloric acid, the solution turns from magenta to a colorless liquid. This allowed the team to put a visual metric on the level of mixing. The test was carried out using a clear acrylic annulus with the axis aligned vertically and closed off at its base. The two different solutions were injected radially inward near the base of the annulus. The setup of this test is illustrated below. One of the variables of the testing was the degree of offset between the inner and outer injectors. They varied in increments of 5 degrees, from injectors being in line to perfectly offset. During the testing, the flow was imaged from both directly above and from the side. The images were then imported into a processing code in Matlab to quantify the level of mixing. More detail can be found in their original final report entitled *Continuous Rotating Detonation Engine: Propellant Mixing Visualization*.

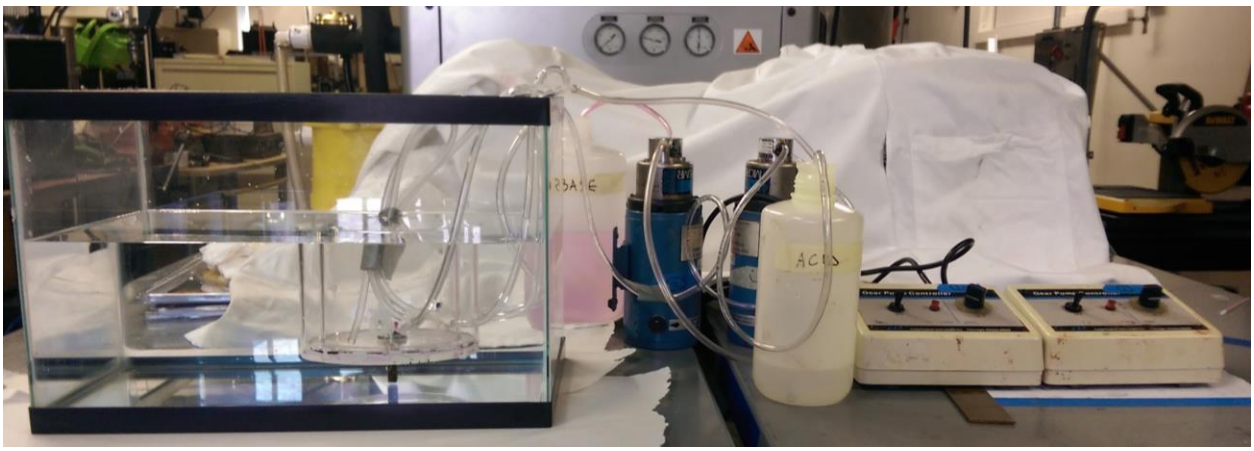

Figure 4.3: Image of the experiment setup for the liquid flow mixing test

4.2.2 *Gas Chromatograph*

In an attempt to further validate the mixing visualization experiment, the injection mixing design of the hot-fire combustor was tested. This proved to be more complicated than the water tunnel

visualization tests since the actual gases are highly combustible. Therefore, oxygen and hydrogen were replaced with inert gases, argon and helium respectively. While their characteristics differ from the actual oxidizer and fuel, argon and helium have similar molecular weights when compared to oxygen and hydrogen.

$$MW_{He} = 4.00\frac{kg}{mol}, \qquad MW_{Ar} = 39.95\frac{kg}{mol}$$

Since stoichiometric hydrogen and oxygen has a fuel to oxidizer ratio of 2:1, the same ratio was used with helium and argon. Consequently, on a mass basis for every 8 kilograms of helium injected into the annulus, 40 kilograms of argon was also introduced. The method to quantify how well the two gases had mixed required a gas chromatograph (GC). This device is used to measure the quantities of gases in mole percentages. It does have some limitations. The machine requires the use of medical grade air, hydrogen and an inert carrier gas such as nitrogen. The gas chromatograph is incapable of identifying the carrier gas. The particular device used in these experiments had not been run for quite some time and required calibration. As the only gases of concern were argon and helium, these two gases were used to calibrate the system. The process of calibration required taking multiple small samples of argon and helium gas mixtures of known quantities. These mixtures would then be measured by the gas chromatograph to determine if the mole percentages corresponded with the known mixture quantities.

When collecting each sample of argon and helium in each bottle, the amount of each gas was determined by using the partial pressures of each. The partial pressure of a particular compound in a gas mixture is directly related to the amount of that compound in the mixture. This relationship is shown below.

$$\frac{P_i}{P_{mix}} = \frac{n_i}{n_{mix}} = \frac{V_i}{V_{mix}} \tag{4.2}$$

$$P_{mix} = \sum P_i \tag{4.3}$$

P_i, n_i, and V_i are the partial pressure, moles, and volume of a particular gas in the mixture. The other variables describe the same properties for the mixture. Equation X shows that if both the partial and total mixture pressure is known, then the amount of the particular gas by either mole or volume percent can easily be obtained.

The first step required that the bottle be at vacuum pressure. This ensured that no other gas or compound was contained in the sample bottle prior to its use. Then, the sample bottle was filled with compressed argon until the bottle reached the desired pressure. At which point the supply of argon was shut off. This pressure corresponds to the partial pressure of argon in the mixture. Next, the same was done with the compressed helium until the bottle reached the desired total pressure. The partial pressure of helium was calculated using the equation x2. The ratio between partial pressure of each gas and the mixture pressure is equivalent to the amount of the gas by percent volume. Using this process, several sample bottles were collected with varying ratios of argon and helium, shown by the following table.

Table 4.2: Argon and helium sample bottle mixture ratios

	Sample 1		Sample 2		Sample 3	
Gas	Pressure (psi)	% Volume	Pressure (psi)	% Volume	Pressure (psi)	% Volume
Argon	50.3	25%	100	50%	165	76.8%
Helium	149.7	75%	100	50%	49.7	23.2%

The sample bottles were then hooked up to the gas chromatograph. Each bottle was tested multiple times to provide further calibration of the GC. The results from the

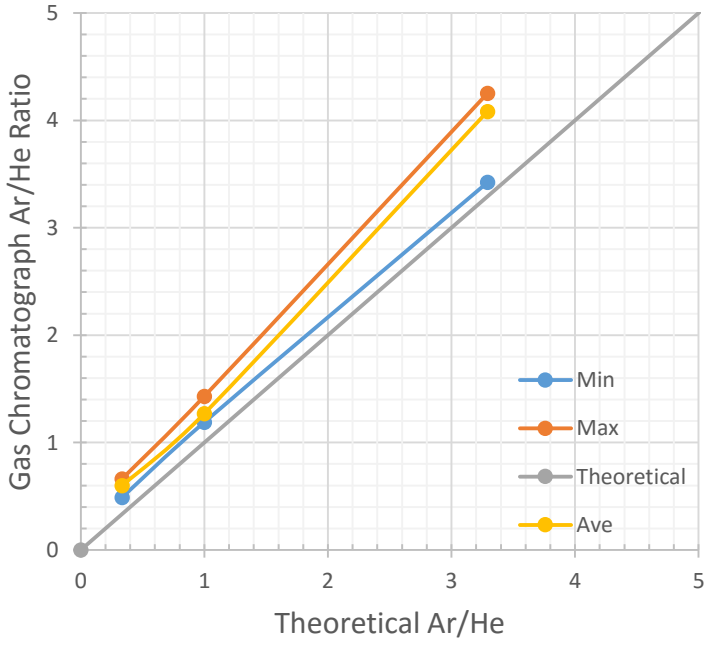

Figure 4.4: Gas chromatograph calibration curves

4.3 COMBUSTION TEST

Although the results of the hot combustion test will not be included in this body of work, the images below show the setup of the combustion testing.

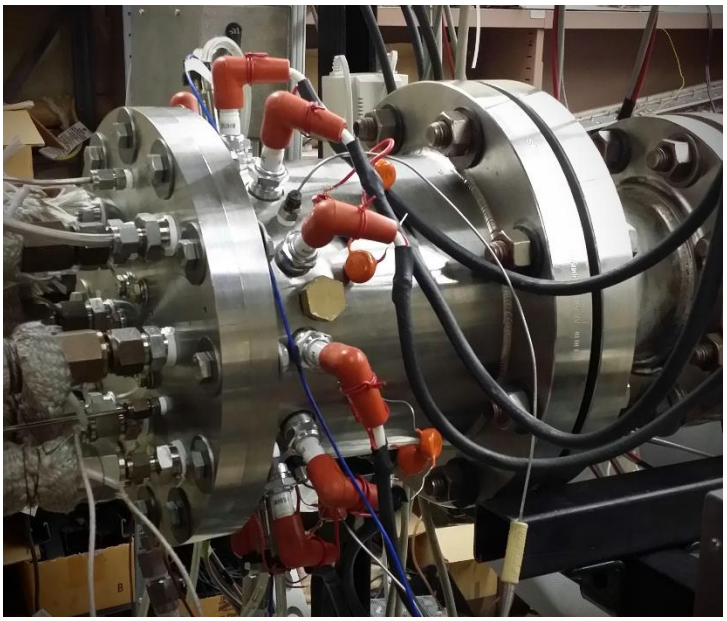

Continuous Rotating Detonation Combustor

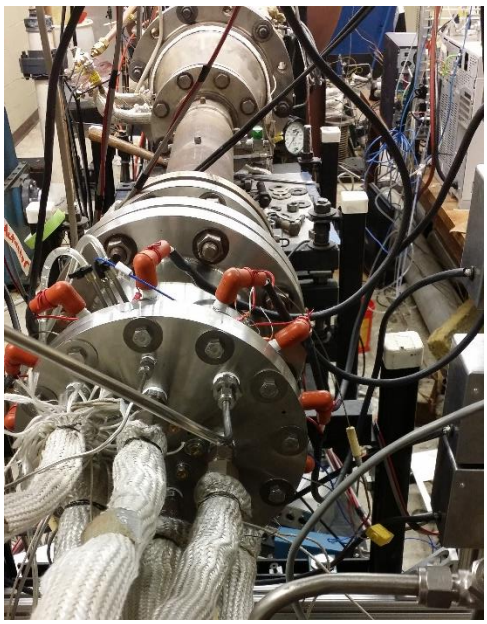

Top View

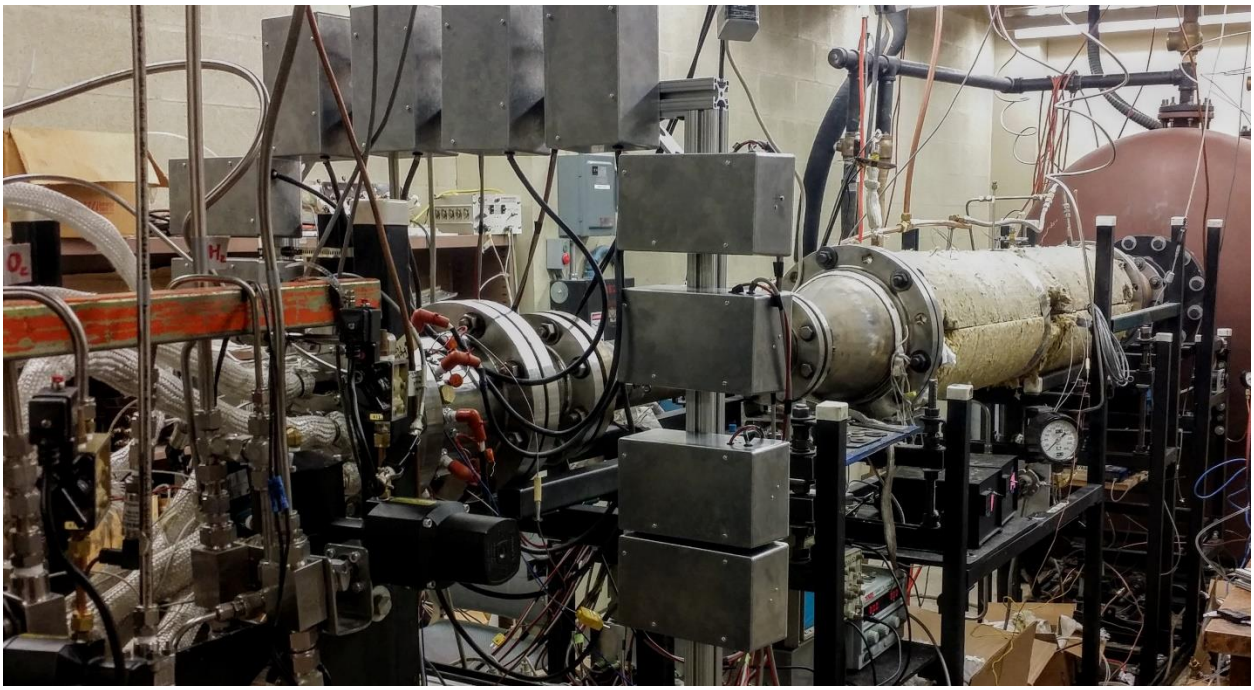

Side View

Figure 4.5: Images of experimental setup of combustor in the SWR lab

Chapter 5. RESULTS AND DISCUSSION

5.1 ACOUSTIC ANALYSIS OF THE WAVE CONTROLLER

Initially, the acoustic analysis of the wave controller was believed to be a minor step in the goal toward hot-combustion testing. However, the early analysis proved that a significant amount of time would be required to fully understand and develop the operating parameters to achieve successful wave controller operation. The two main goals of the test were to determine if the sparking array was able to first create a consistent transverse wave and second, force the transverse wave to travel in only one azimuthal direction.

5.1.1 *High-Speed Camera Data*

The setup with the high-speed camera focusing on a small section of the annulus seemed to be the best scenario to catch the acoustic waves in motion. The high speed-camera was set to record at the rate of 240,000 frames per second. At this speed the resolution of the images produced were only 120 x 240 pixels. The low resolution still made it possible to see the shock waves. The sparking mechanism was set to $n = 1$, producing 1 wave, with an input frequency of 9.125 kHz and a voltage of 150 V. The camera was oriented to see through the annulus toward the light source, providing an end-view of the annulus. The 3 figures on the next few pages depict the individual frames from the high speed camera centered on a single spark plug. The time elapsed between each frame is only 4.16 microseconds. In each frame the spark plug is located on the exterior wall of the annulus with the actual spark being emitted at a point tangent to the outer diameter of the annular gap. Since the wave controller was on for 5 seconds before acquiring the camera data, there was plenty of time to let the system reach a steady state of operation.

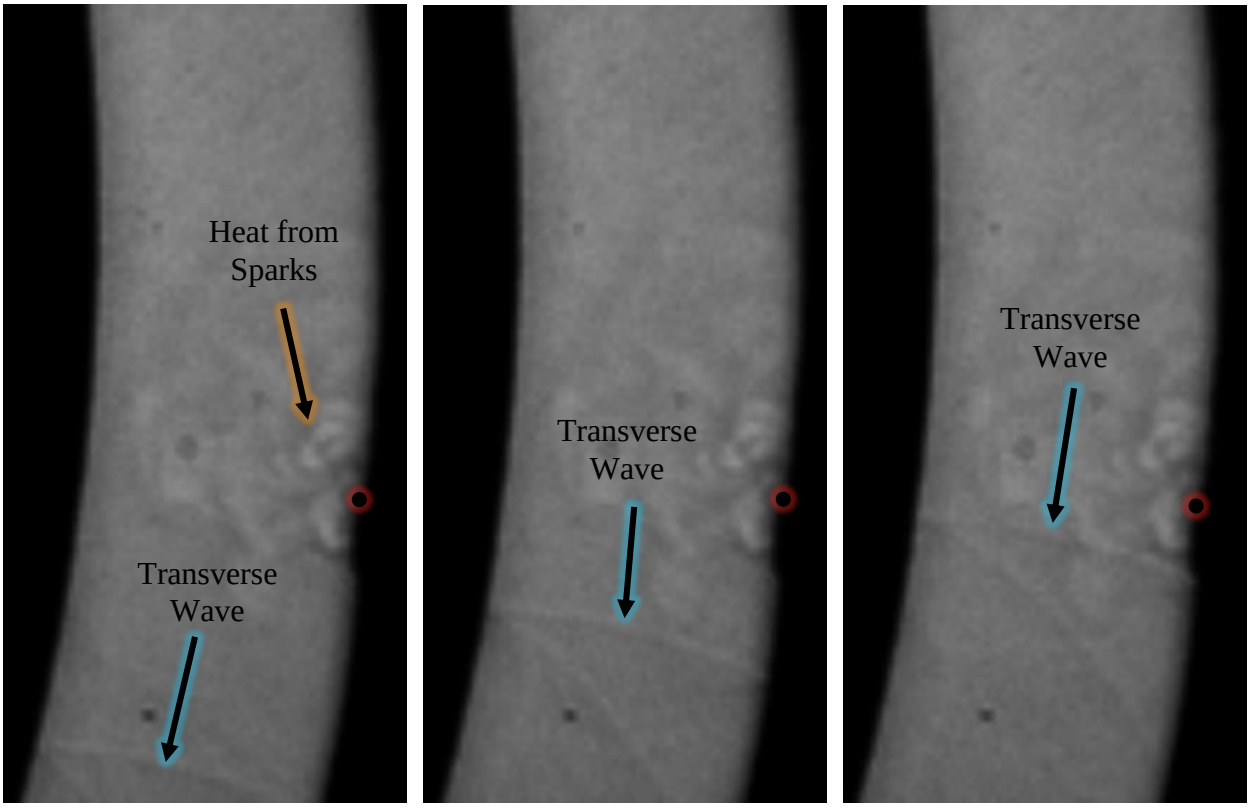

Frame 1 Frame 2 Frame 3

Figure 5.1: Frames 1-3 showing the transverse wave traveling counter-clockwise, before a new spark is fired. The red dot indicates the location of the spark plug.

From the three frames shown in Figure 5.1, there is a transverse wave generated. This is from the previous spark plugs blast waves coalescing. The plumes in the center of the each frame show the heat generated by the spark plug. The slightly angled line protruding from the left side of the transverse wave is the reflected wave off of the inner wall of the annulus. It is important to note that there is no transverse wave moving clockwise in annulus. This demonstrates that the wave controller is indeed forcing the acoustic waves to travel in only one direction. However, this is only half of the requirement to show the wave controller is being successful. The second criteria is that the transverse wave must be phased with the blast wave from the next spark firing.

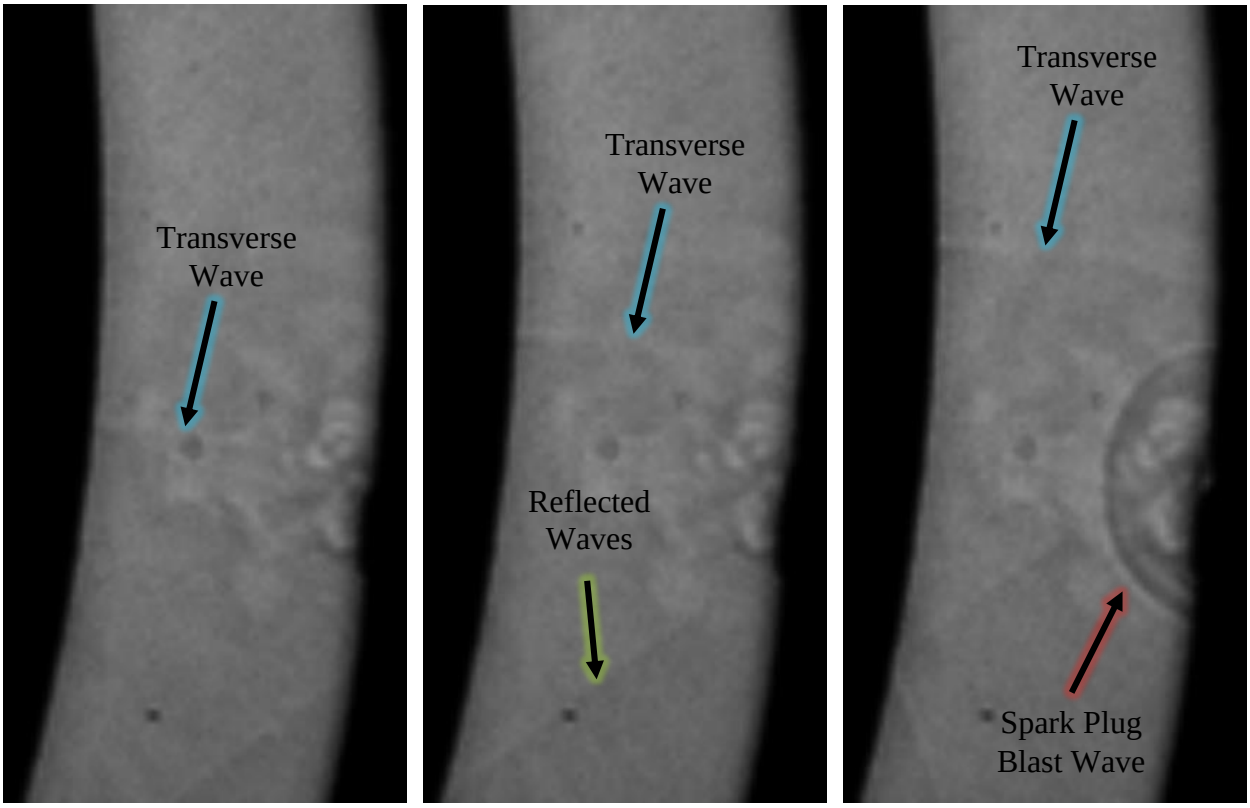

Frame 4 Frame 5 Frame 6

Figure 5.2: Frames 4-6 showing the transverse wave propagating while the spark plug fires

In the next three frames, the transverse wave continues to propagate counter-clockwise through the annulus. In the time between Frames 5 and 6, another spark is fired generating a new blast wave. Confined by the outer wall, the wave travels in all inward directions as a spherical wave propagating from a single point source. In Frame 6, the blast wave of the new spark is only slightly behind the transverse wave from the previous spark plugs. This shows that the individual spark plugs are perfectly timed with each other. The next 3 frames depicted in Figure 5.3 show the blast wave continuing to propagate toward the inner wall of the annulus. By Frame 9, the original transverse wave and the new blast wave have nearly coalesced to form a single transverse wave.

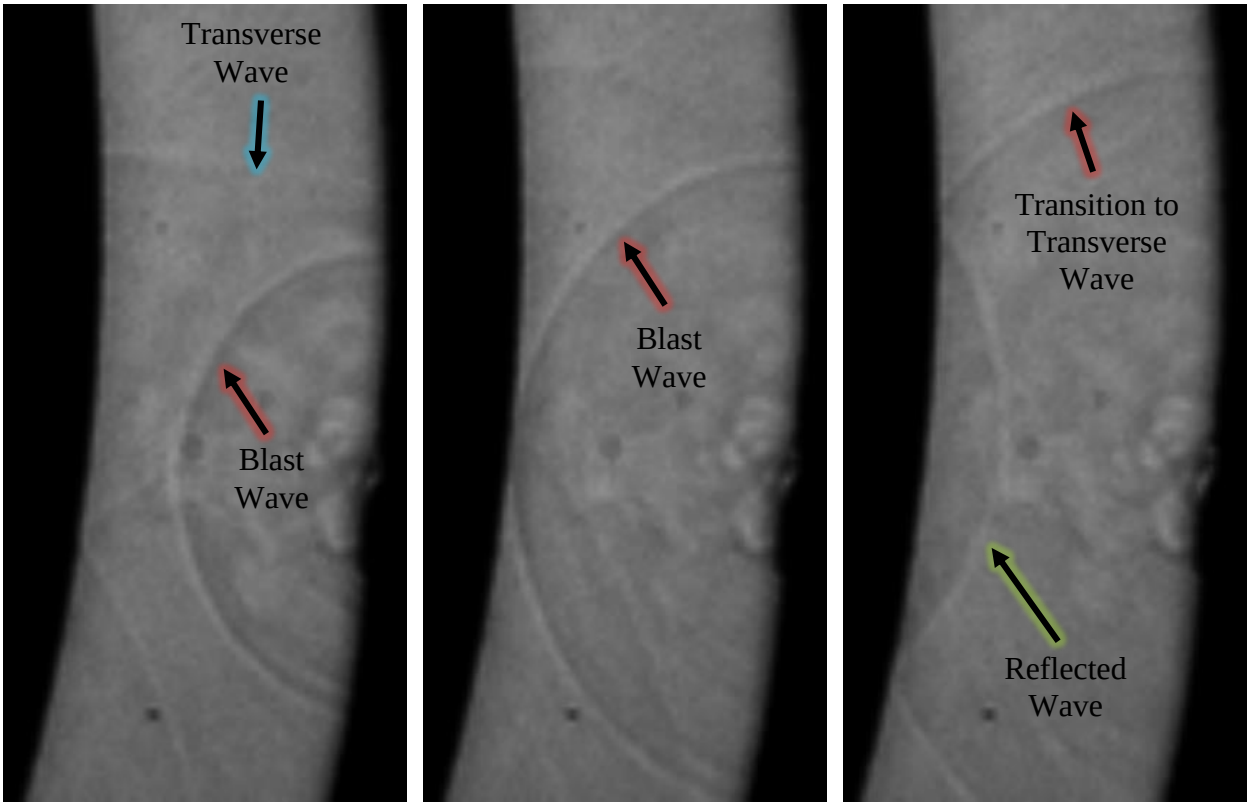

Figure 5.3: Frames 7-9 showing the new blast wave enhancing the transverse wave

By analyzing the distance traveled by the blast wave from Frame 6 to Frame 9, the speed of the blast wave can be determined. The velocities and Mach numbers are depicted in Table 5.1 shown below.

Table 5.1: Velocities and Mach numbers of the acoustic waves for air at T = 320 K.

	Frames	Velocity (m/s)	Mach Number
Blast Wave	6-7	780	2.1
	7-8	780	2.18
	8-9	720	2.01
	1-9	660	1.84
Transverse Wave	1-2	1080	3.01
	2-3	750	2.09
	3-4	750	2.09
	4-5	720	2.01
	5-6	780	2.18
	6-7	780	2.18
	7-8	810	2.26

Looking at the velocities and Mach numbers of the waves, the waves are supersonic. This demonstrates that the waves produced from spark plugs do indeed emulate shock waves and are not purely acoustic waves. It is also interesting to see that the velocity of the transverse wave starts high 780 meters per second and then slows down over the next few frames. From frame 5 to 6, the transverse wave starts to pick up speed again. This correlates exactly to the new blast wave firing. From frames 6-9, the blast wave is transferring its energy into the transverse wave, since it is decreasing in velocity. This confirms that the phased pulses of the spark plug array is successfully creating and sustaining a transverse wave moving in a single circumferential direction.

5.1.2 *Spark-Gap Data*

Using the spark-gap as a flash light source, high resolution stills of the engine were obtained. This setup used the same settings for the spark plug array except the number of waves was varied throughout the testing. Even though the flash was wired to the external flash output of the camera, the timing of the flash didn't always correspond with the camera shutter being open. This made acquiring useful images somewhat difficult and the bulk of the images collected had a small portion of the shutter visible. Since the light produced was just a flash with its center somewhat unknown, aligning everything perfectly also proved difficult. Despite countless attempts to address this issue, most of the images obtained have light and dark areas instead of the grayish shade of the high-speed camera data. Even with these setbacks, a few quality images were acquired.

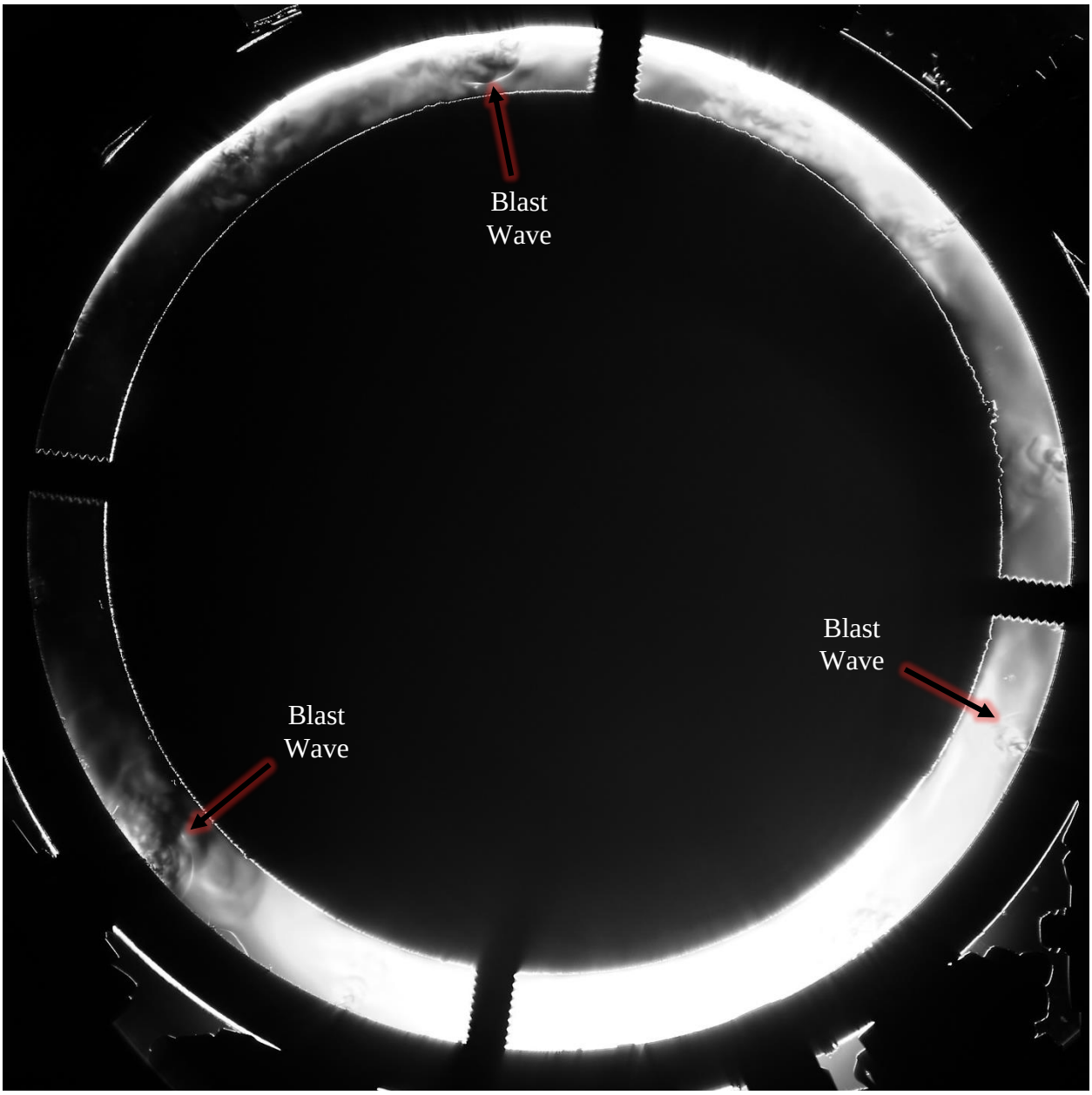

Figure 5.4: Image of blast waves in the annulus using the spark-gap where $n = 3$

Another challenge of imaging the blast waves is that there was no way to control the time the image is captured in reference to the location of the blast waves. With some luck, an image showing 3 blast waves each 120° apart was captured. These correspond to the three spark plugs firing at the exact instant. In Just like the high-speed camera data, the heat plumes of each spark plug are visible.

Figure 5.5 shows the same blast wave image only zoomed in, to see the minor details. The zoomed in sections show that each hemi-spherical wave has near equivalent radius, proving the spark plugs did fire at the exact same instant.

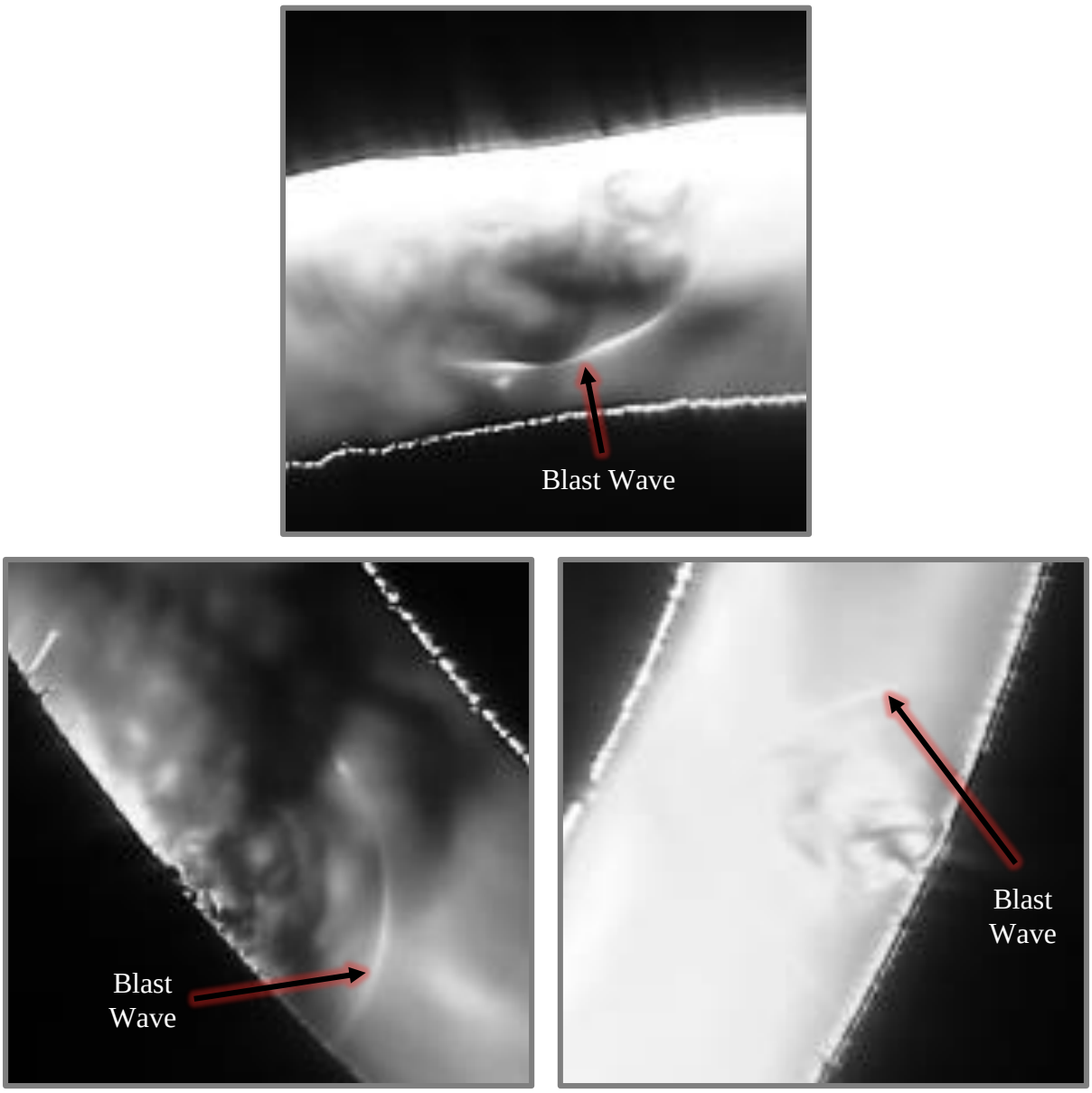

Figure 5.5: Zoomed in areas of blast waves

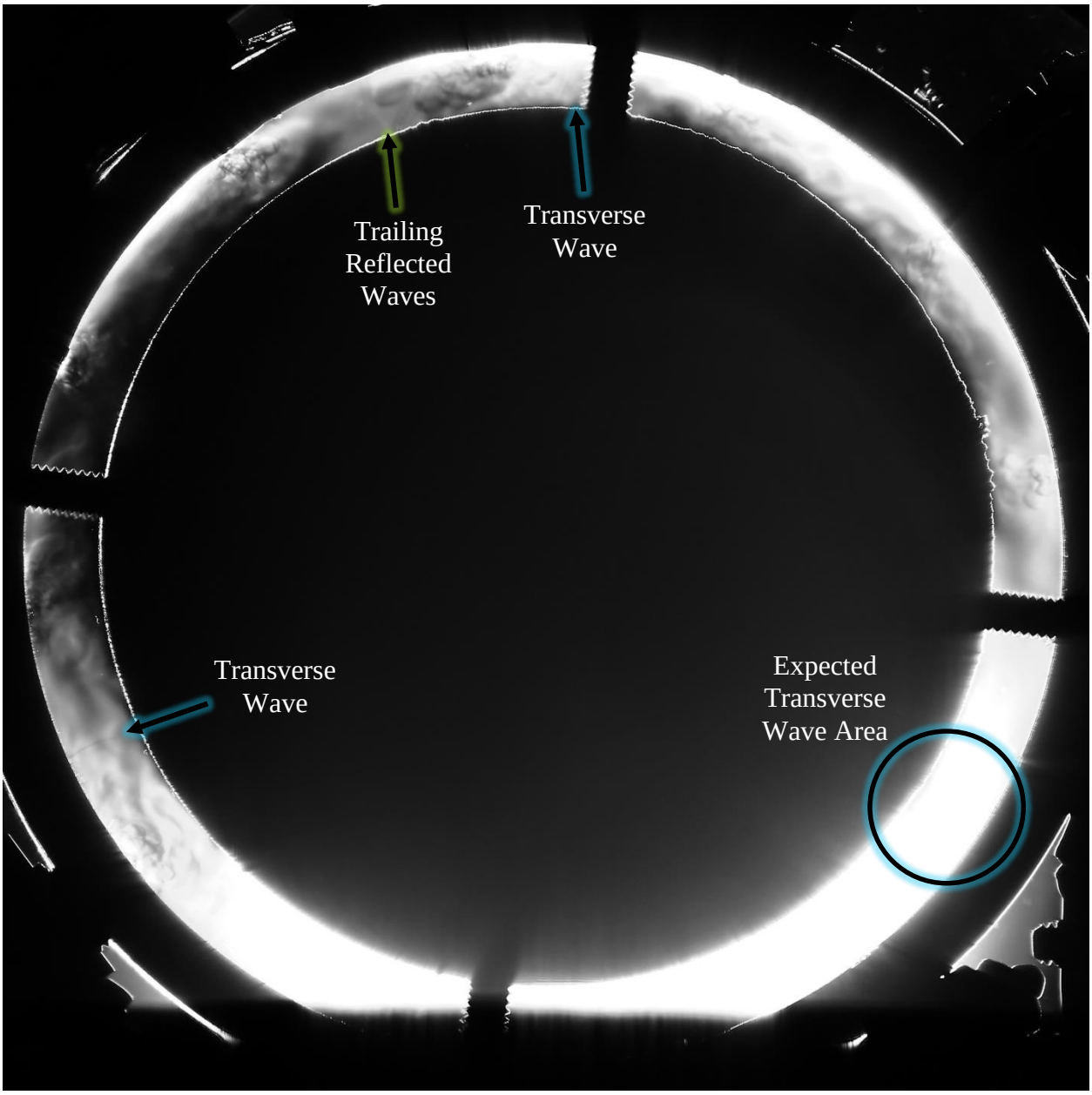

Figure 5.6: Image of transverse waves in the annulus using the spark-gap where $n = 3$

Shown in the figure above is another image of the waves propagating in the annulus. Except in this instant the image captured the waves moving transversely. Due to the slightly misaligned light, the third transverse wave is not visible. The next figure shows a zoomed in view of the sections involving the transverse waves. By looking at the curvature of the waves, the motion of the waves is counter-clockwise. Just as expected for $n = 3$ waves, the two visible transverse waves are roughly 120° apart.

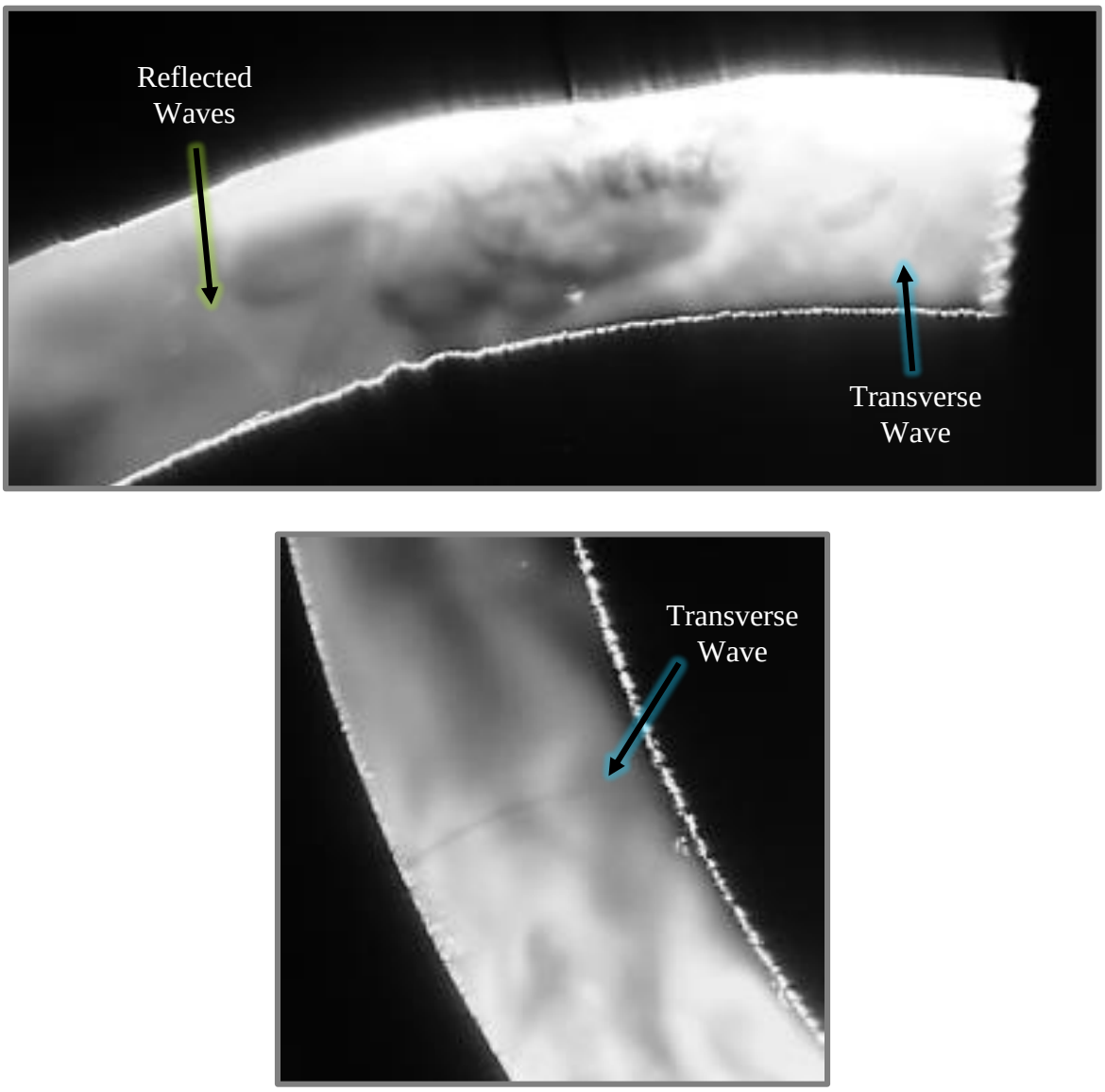

Figure 5.7: Zoomed in areas of transverse waves

The image data acquired using the spark-gap illustrates the wave controller is capable of generating multiple equidistant waves within the annular gap and is capable of controlling the direction of the waves.

5.2 MIXING TESTS

5.2.1 *Subsonic Flow Visualization Results*

The results of the subsonic flow visualization tests are shown in the figures below. The color gradient image maps were obtained from grayscale images and illustrate the level of mixing. Red depicts the areas in which the hydrochloric acid and a mixture of sodium hydroxide and phenolphthalein have reacted, indicating completely mixed. The blue illustrates areas of completely unmixed fluid. Each image shows the exact same flow area of the annular duct. The red/yellow line is the injection of one of the fluids.

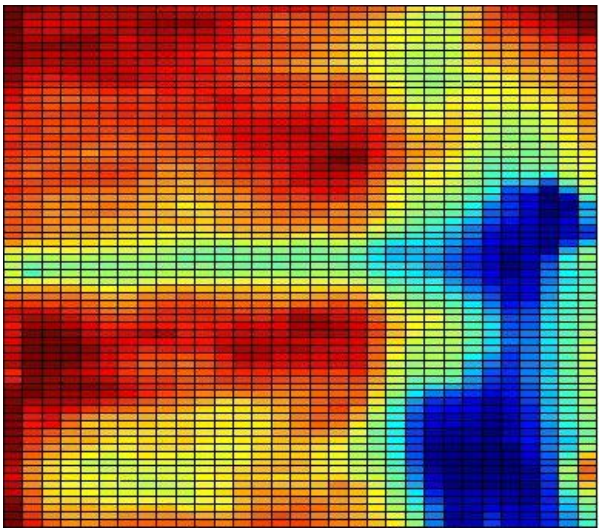

Injectors inline, 0°

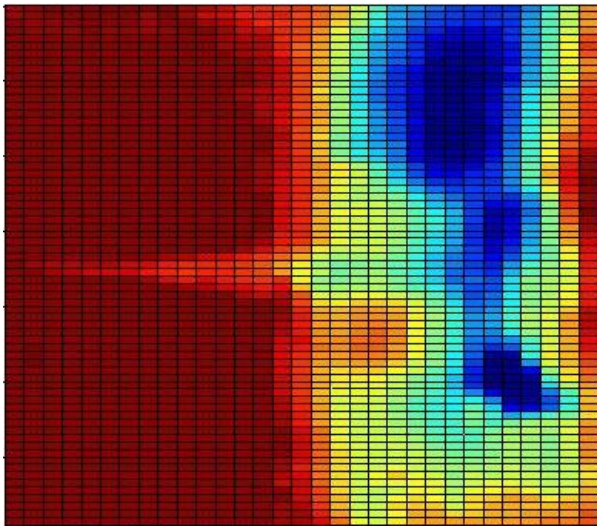

5° offset

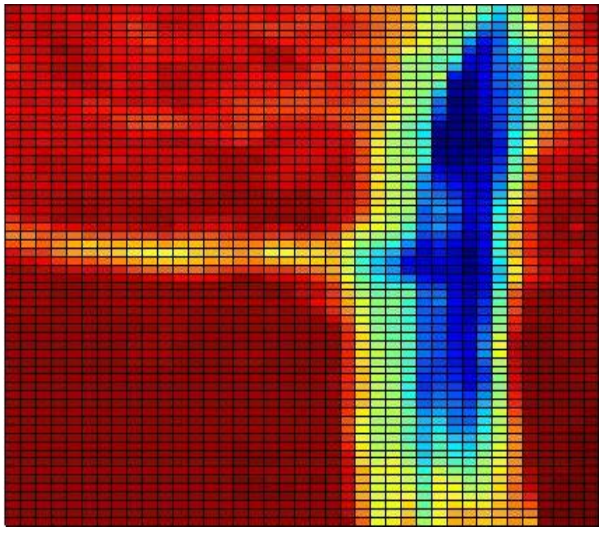

10° offset

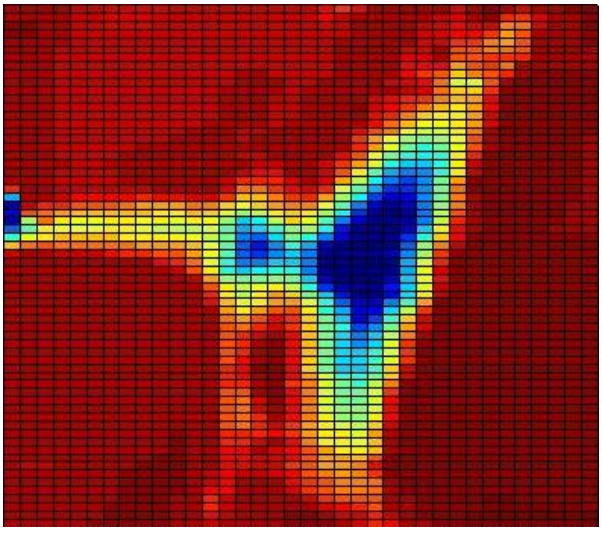

Symmetrically offset, 15°

Figure 5.8: Color maps of mixing area for different injection offset.

From the images of Figure 5.8, it is evident that the amount of blue decreases as the injector angle increases from inline to symmetrically offset. By associating values to the colors with red equal to 1 and blue equal to 0, the standard deviation with respect to 1 was calculated for each image. The table below shows the standard deviation for each configuration.

Table 5.2: Standard deviation

Injector Configuration	**Standard Deviation**
Directly aligned	0.0468
5° offset	0.0349
10° offset	0.0319
Symmetrically offset (15° offset)	0.0262

Table 5.2 reveals that the standard deviation decreases as the injector angle approaches the symmetrically offset configuration. A smaller standard deviation demonstrates a higher degree of mixing.

5.2.2 *Gas Chromatograph Results*

In this section, the results from the sample bottles of gas taken at varying axial and azimuthal locations will be provided. Throughout the analysis of the sample gases, the gas chromatograph had several technical issues that were difficult to resolve. Due to these complications, an insufficient amount of samples were collected. Therefore, the data presented here may not be a true representation of the level of mixing. The first sample bottles collected were obtained at different axial and azimuthal locations in the annulus. Because of the axis-symmetric nature of the annulus, only the axial location was recorded. The following table describes the locations for each sample bottle.

Table 5.3: Axial distance of sample bottles measure from the injectors

Sample Bottle	1	2	3	4	5	6	7	8
Axial Distance (in)	0.25	1	3	5	0.25	1	3	5

The gas chromatograph analyzed all of the sample bottles and the results of the mole ratio of helium to argon are shown in Figure 5.9.

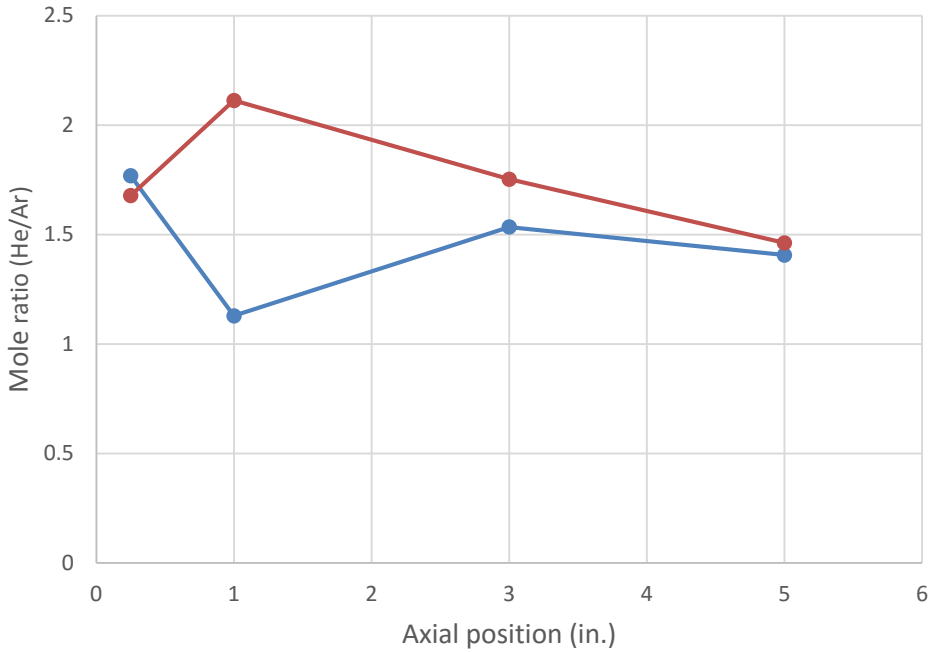

Figure 5.9: Plot of mole ratios for the sample bottles with varying axial distance

The data from the figure above shows that the degree of mixing is somewhat erratic for the first inch and then begins to converge onto a mole ratio of 1.5. The flow of the argon and helium were delivered at a mole ratio of 2 (He/Ar). This would imply that the degree of mixing is getting worse as the fluid moves farther down the annulus axially. By applying the calibration curves to the data, the mole ratio corrects to value even lower. Therefore, the data does not seem to be a good representation of the mixing. It is possible that the mole ratio of helium to argon was not truly 2:1. Therefore, this test should be conducted again with more sample bottles to be more indicative of mixing.

A second set of sample bottles were collected where the axial distance remain constant, but the azimuthal locations were varied. The axial location of the probes was set to the spark plug array azimuthal line. This particular location is important because at this point the mixing needs to be sufficiently close to the stoichiometric mole ratio. The mole ratios of these six sample bottles are shown in Figure 5.10.

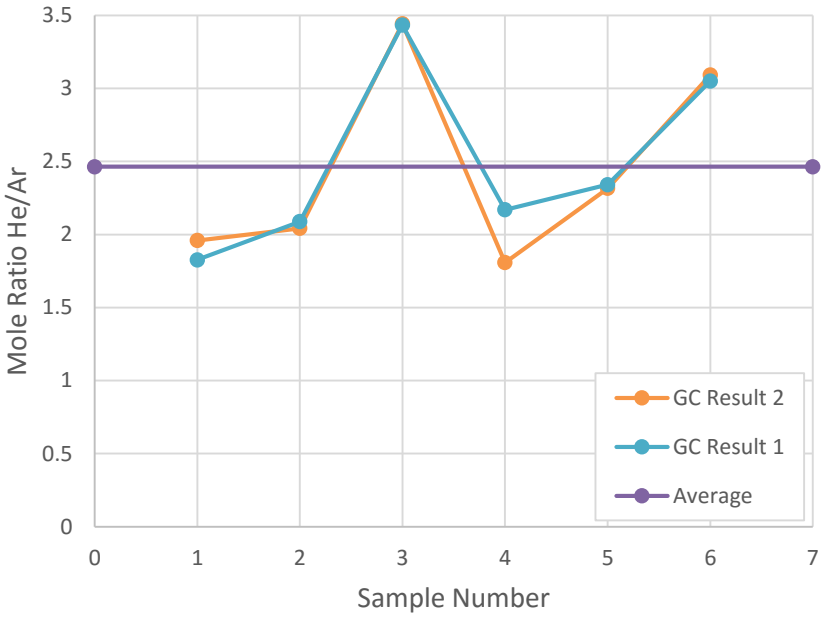

Figure 5.10: Mole ratios for the sample bottles aligned with spark plugs

The mole ratios determined by the gas chromatograph varied slightly, from just under 2 to nearly 3.5. However, the average of the mole ratios was 2.46:1, helium to argon. This correlates to a fuel rich combustion scenario. Using the average calibration curve, a corrected set of data was obtained. This data is shown below.

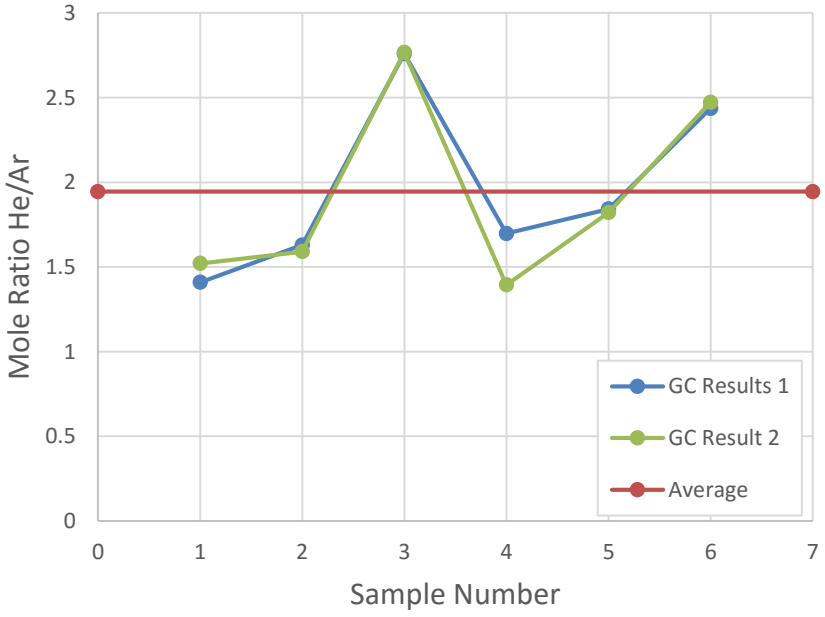

Figure 5.11: Corrected mole ratios for the sample bottles aligned with spark plugs

The corrected data shows that the average mole ratio is 1.94. This is quite close to the desire stoichiometric mole ratio of 2:1. However, the variation of the individual sample bottles indicates that the mixing is not equivalent at the varying circumferential location along the same axial plane. The degree of variation warrants the need for further testing of mixing using the gas chromatograph.

5.2.3 *Mixing Results Summary*

From the subsonic flow visualization test, it is evident that the injector design of the combustor will produce adequate mixing. The test illustrated that it is more beneficial to set the inner and outer injectors symmetrically offset from each other. While the results obtained from the gas chromatograph were not ideal, they did demonstrate that a degree of mixing is taking place. For a more complete representation of the gas mixing of the combustor, a much larger sample size is required.

Chapter 6. CONCLUSION

6.1 Summary and Concluding Remarks

The overall intent of this research is to successfully develop a continuous rotating detonation combustor. The key element in advancing this combustor is the wave controller. By utilizing this system, the combustor can achieve continuous detonation in the annular combustion chamber. The images obtained using the high-speed camera from the acoustic testing show that the wave controller is indeed capable of generating transverse acoustic waves traveling in only one azimuthal direction. This data proves the wave controller performs as predicted by theoretical analysis. In addition to this, the still images obtained using the spark-gap light source illustrate the wave controller is also able to create and sustain more than one wave in the annulus. In addition to the wave controller, the simple injector design has been proven to adequately mix the reactants for successful combustion. While the mixing results from the gas chromatograph shows some positive results, more data should be acquired to obtain a better representation of the mixing. However, the data from the subsonic flow visualization demonstrated the design has a high level of mixing. With the wave controller images and the mixing results, it is very plausible that hot-fire combustion testing will be successful.

6.2 Recommendations for Future Research

For future analysis of continuous rotating detonation combustor research, it is recommended to focus on the following areas to improve the combustor and wave controller.

6.2.1 *Heat Management of Combustor*

Since the process of detonation combustion produces such high temperatures, future iterations of detonation combustors should incorporate active cooling methods. This is one major aspect of continuous detonation combustors keeping it from becoming a mainstream technology. By implementing cooling methods, the combustor could be run for much longer than 1 second. Active water cooling of both the interior and exterior walls of the annulus, would keep the metal sufficiently cool for long-term operation. It should also be noted that for better heat transfer through the metal, a metal with a higher thermal conductivity than stainless steel should be used.

Besides water cooling, un-combusted fuel or oxidizer could be rerouted and introduced into the combustion chamber downstream of the spark plugs. Injecting the gas parallel to the flow and along the walls of the annulus would help keep these surfaces at a lower temperature than the combusted products. This process is known as film cooling and is often performed on turbine blades on turbojet engines.

6.2.2 *Higher Energy Input of Wave Controller*

To increase the effectiveness of the wave controller, it would be beneficial to increase the number of spark plugs of the system. This would increase the energy input into the system and decrease the distance from spark to spark. With a shorter distance, the transition from each spark plug would be smoother, creating a more powerful transverse wave. By introducing more spark plugs, a greater number of individual transverse waves could be created. For example, by doubling the number of spark plugs to 24, the wave controller would theoretically be capable of creating up to 8 equivalently spaced transverse waves. This would greatly enhance the operational range of the combustor since the number of detonation waves is directly related to the mass flow rate of the flow.

6.2.3 *Improved Acoustic Visualization*

While the acoustic wave controller data has been proven to demonstrate the capabilities of the wave controller, future analysis could focus on acquiring high resolution data of the entire annular duct with a high speed camera. While the data from the still images obtained using the spark-gap do show the entire annulus, they are just still images. They do not provide concrete data regarding the direction the transverse waves are traveling. Being able to use a high-speed camera at the high frame rate of 240,000 frames per second and at a least a 1 megapixel resolution would make it possible to catch every transverse wave and determine its direction.

REFERENCES

[1] E. Winterberger and J. E. Shepard, "Thermodynamic Cycle Analysis of Propagating Detonations," *Journal of Propulsion and Power, vol 22(23)*, pp. 694-698, 2006.

[2] F. A. Bykovskii, S. A. Zhdan and E. F. Vedernikov, "Continuous Spin Detonations," *Journal of Propulsion and Power*, vol. 22, 2006.

[3] J. C. Shank, "Development and testing of a rotating detonation engine run on hydrogen and air," Air Force Institute of Technology, 2012.

[4] S. Claflin, "Recent Progress in Rotating Detonation Engine Development at Aerojet Rocketdyne," in *International Workshop on Detonation for Propulsion*, Tainan, 2013.

[5] A. C. Edwards, W. D. Sherman and R. E. Breidenthal, "Turbulent Mixing in Tubes with Transverse Injection," *AlChE Journal*, vol. 31, no. 3, pp. 516-517, 1985.

[6] R. E. Breidenthal, V. R. Buonadonna and M. F. Weisbach, "Molecular mixing via jets in confined volumes," *Journal of Fluid Mechanics,*, vol. 219, pp. 531-544, 1990.

APPENDIX A

A.1 SHOCK WAVE REACTOR

The Shock Wave Reactor or SWR is a combustor in which hydrogen and oxygen are burned and expanded through a nozzle in the presence of high temperature steam. The purpose of using the steam in combination with the propellant was to produce a very hot flame that mimicked the temperatures and conditions a re-entry vehicle would experience.

APPENDIX B: FLOW SYSTEM PID

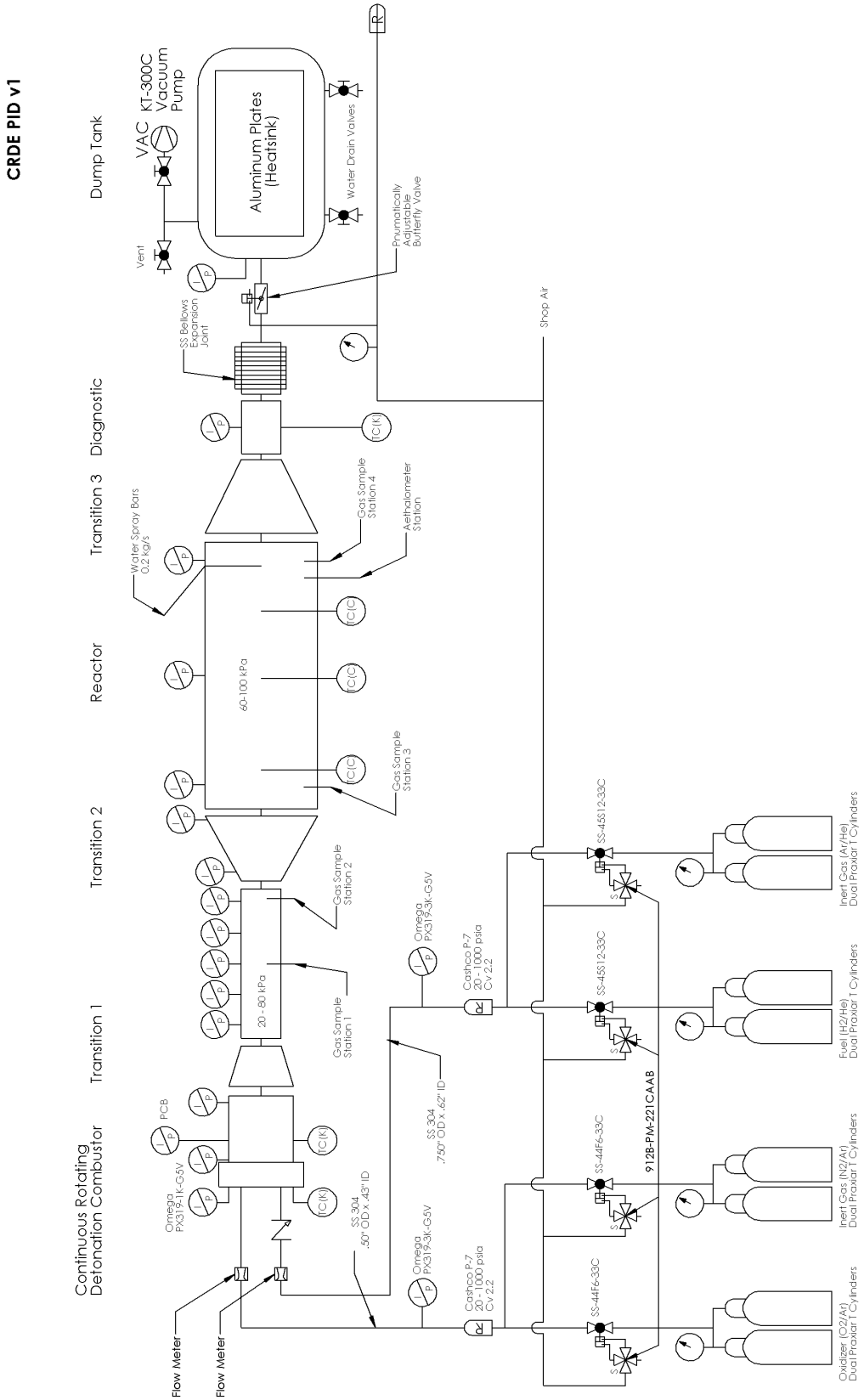

APPENDIX C: CAD DRAWINGS

C.1 INNER CYLINDER

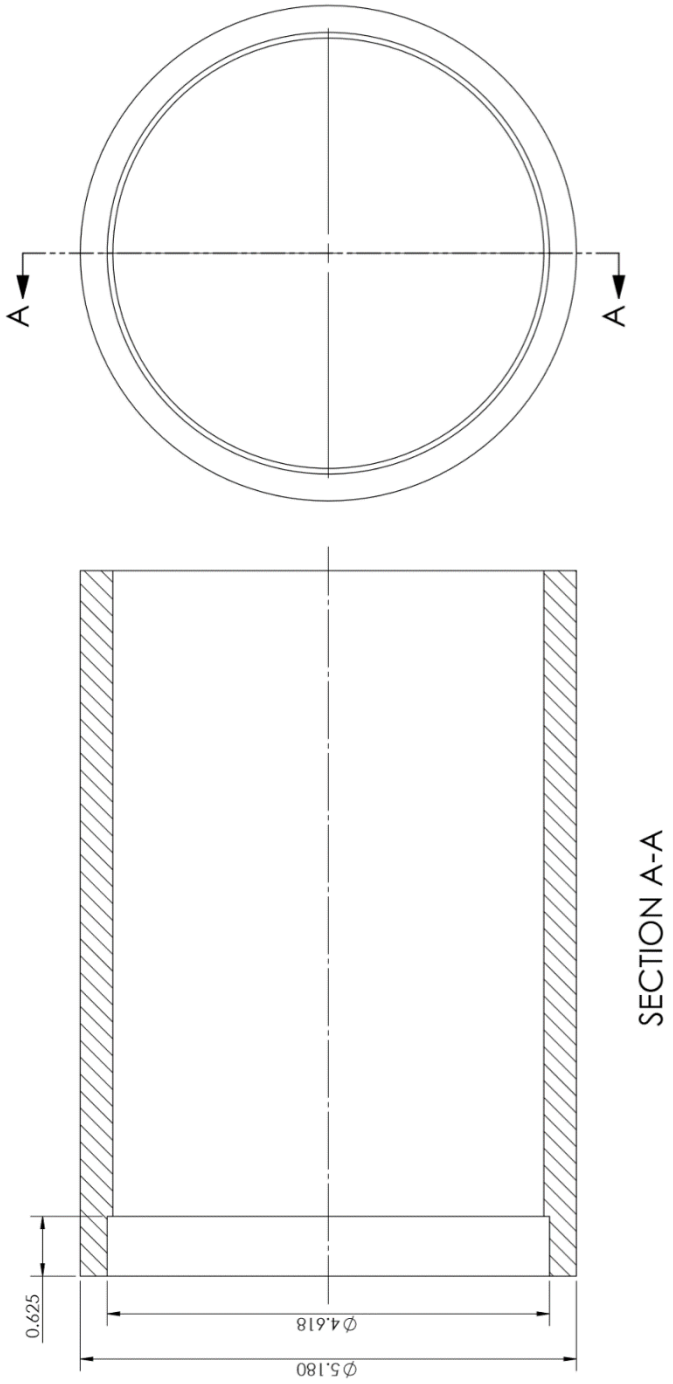

C.2 INNER CYLINDER CAP

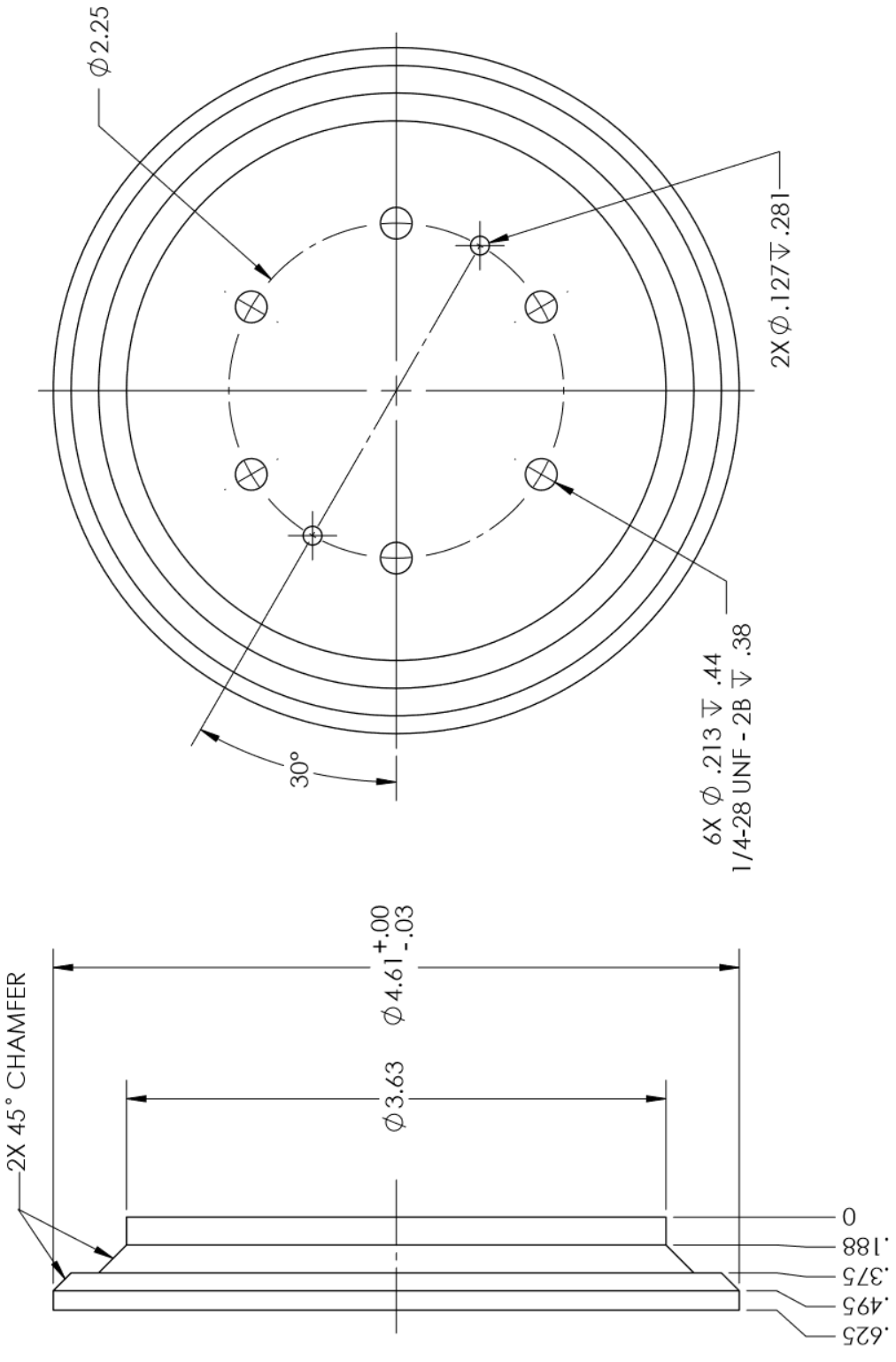

C.3 INNER CYLINDER ASSEMBLY

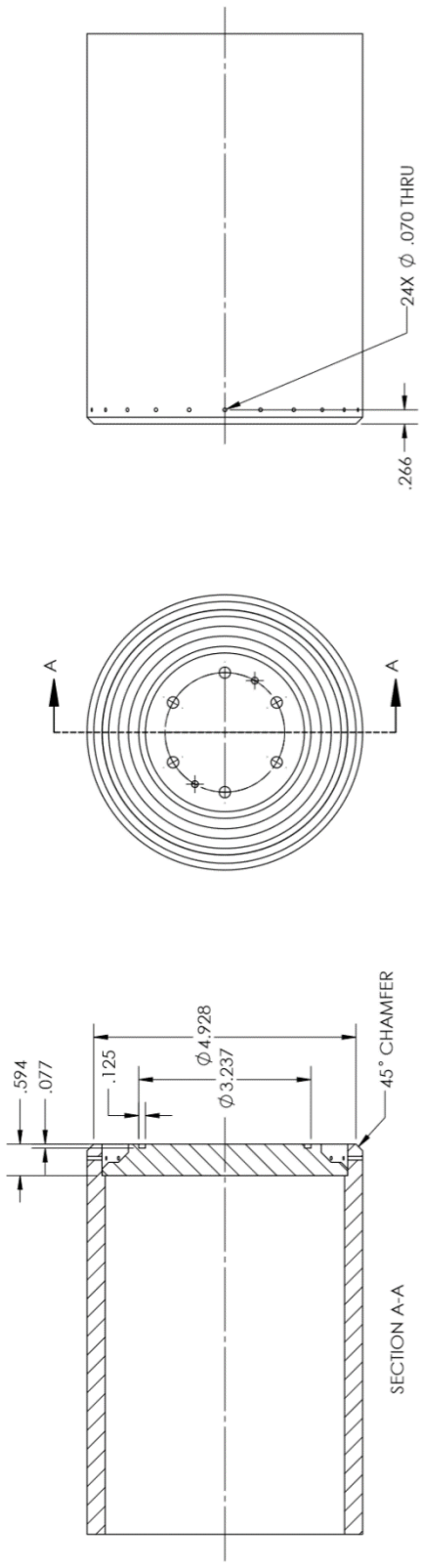

C.4 OUTER CYLINDER

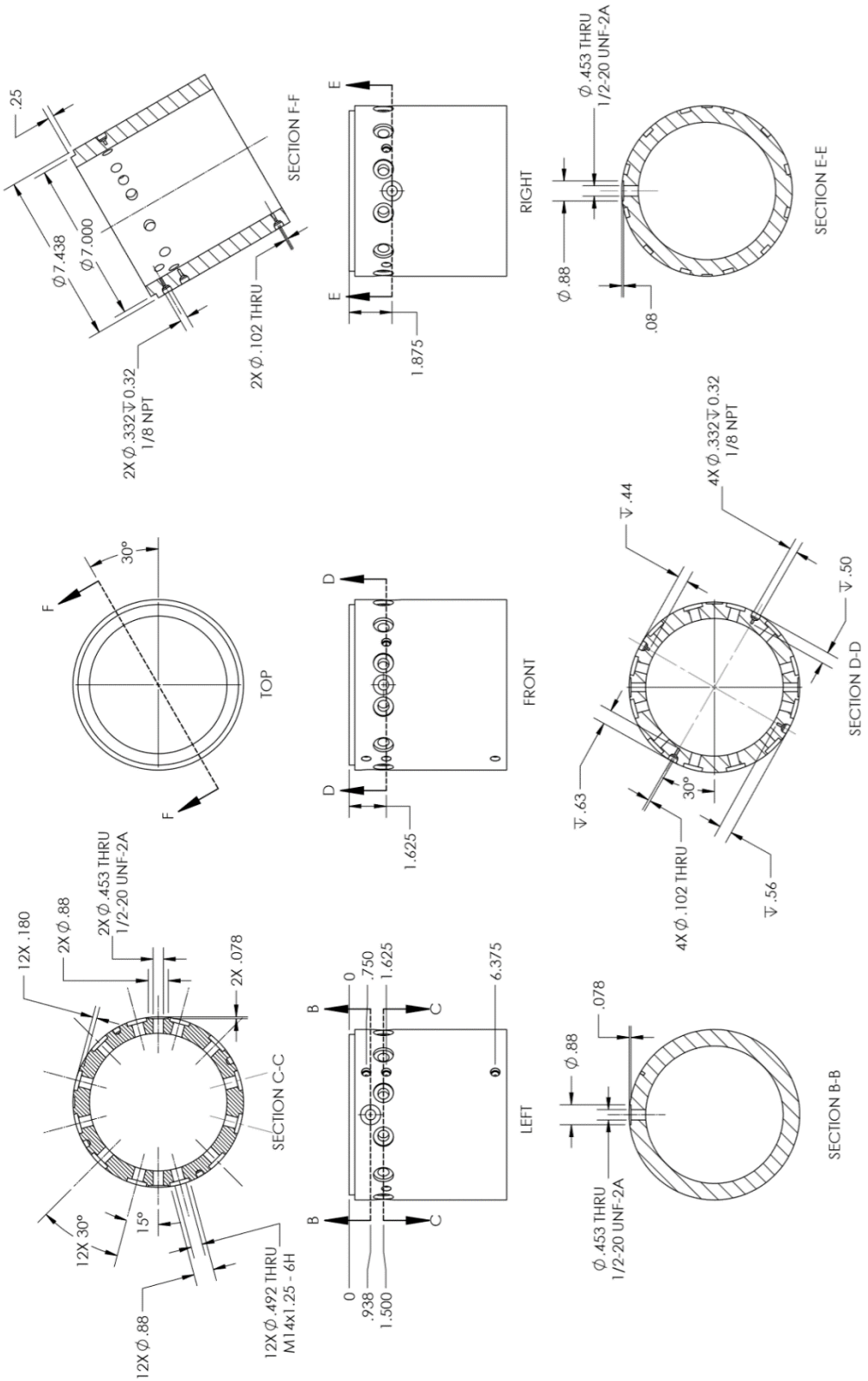

C.5 Outer Cylinder Flange

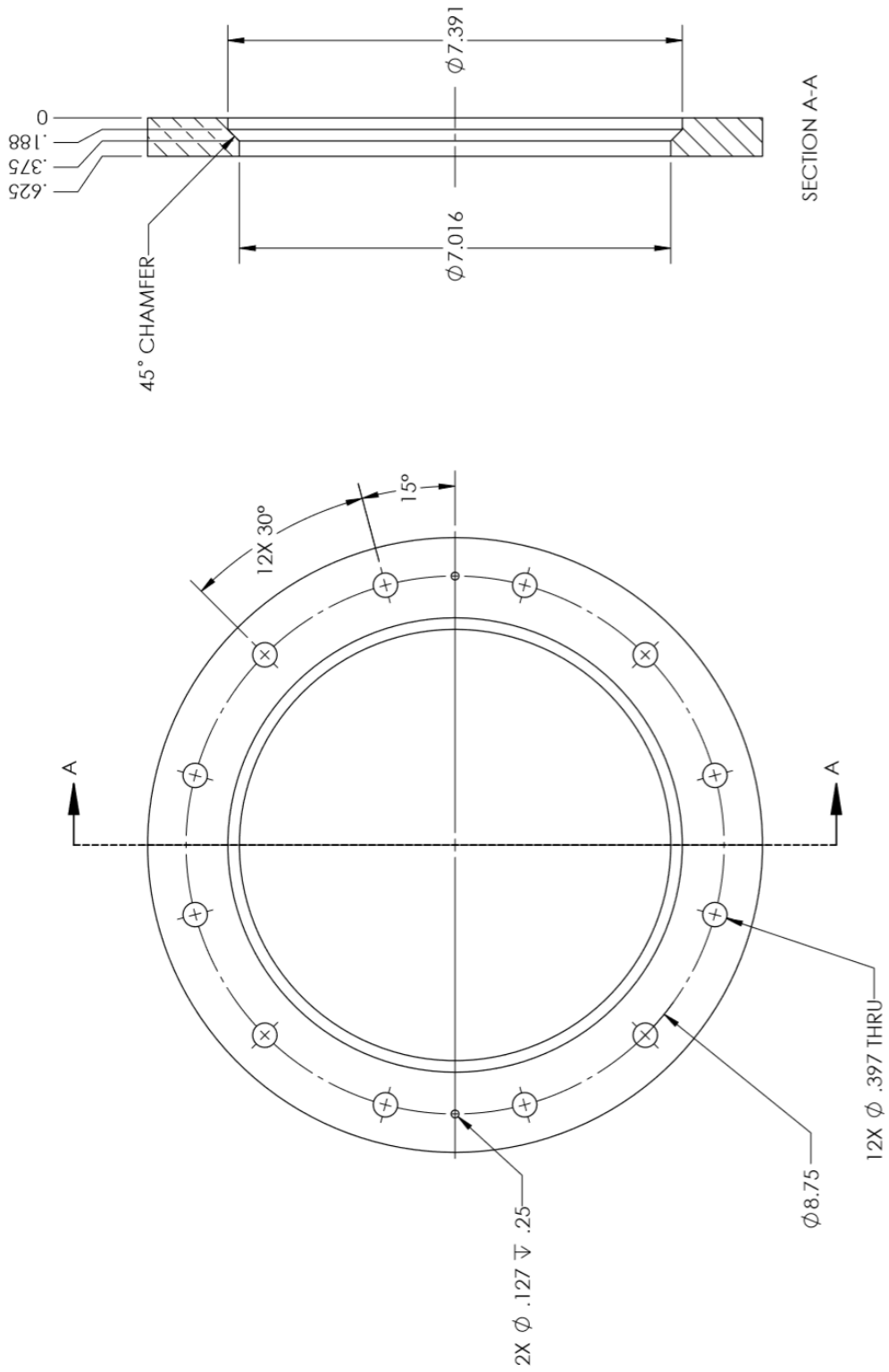

C.6 END PLATE FLANGE

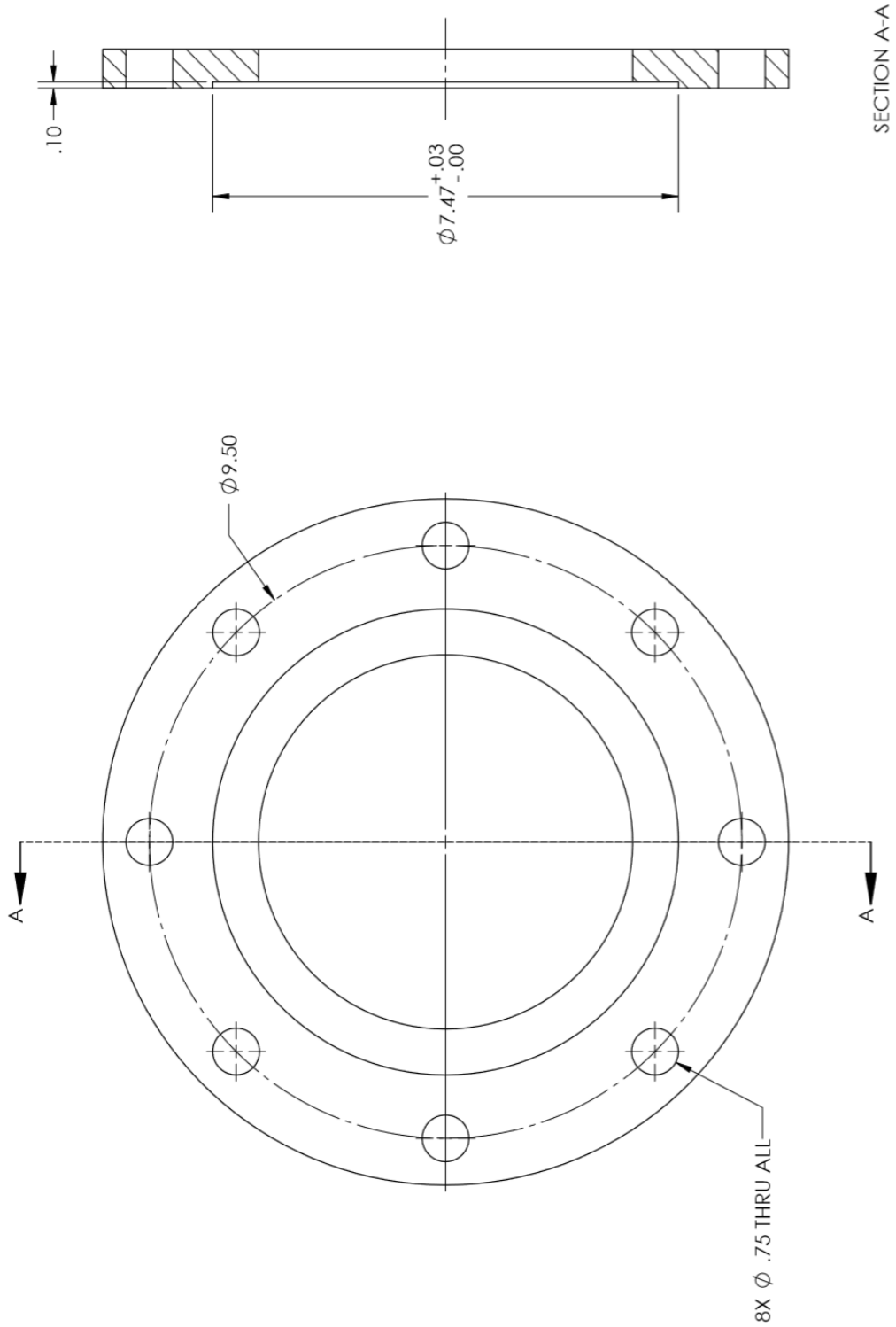

C.7 OUTER CYLINDER ASSEMBLY

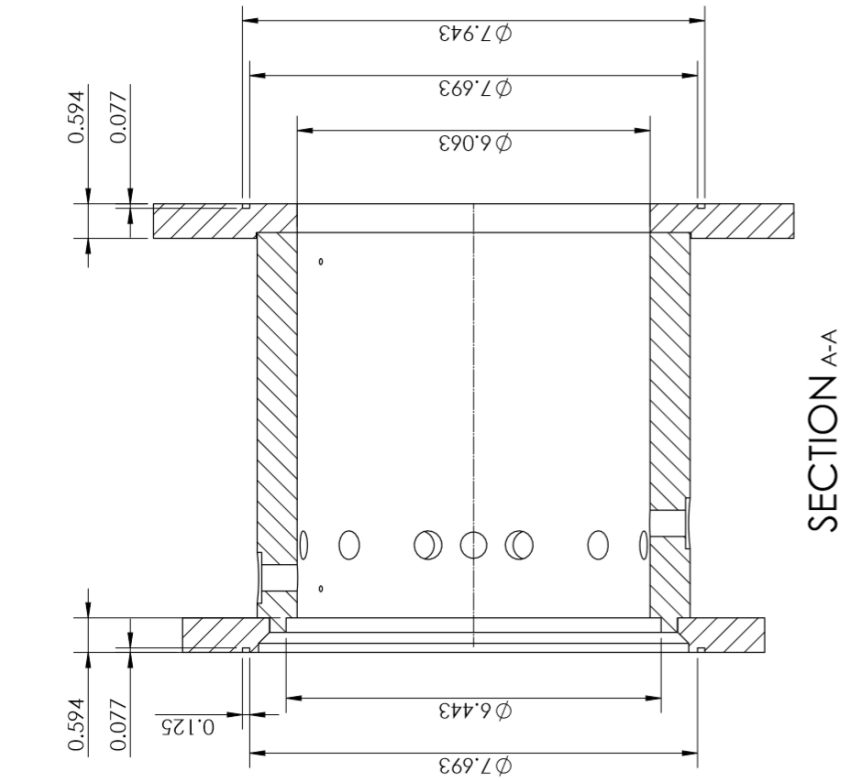

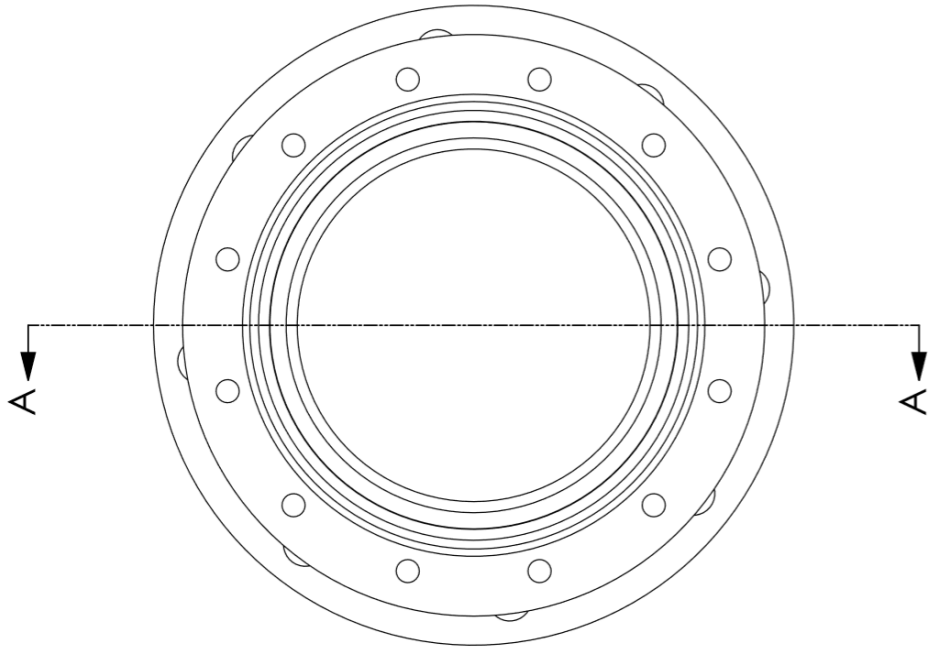

C.8 INJECTOR RING

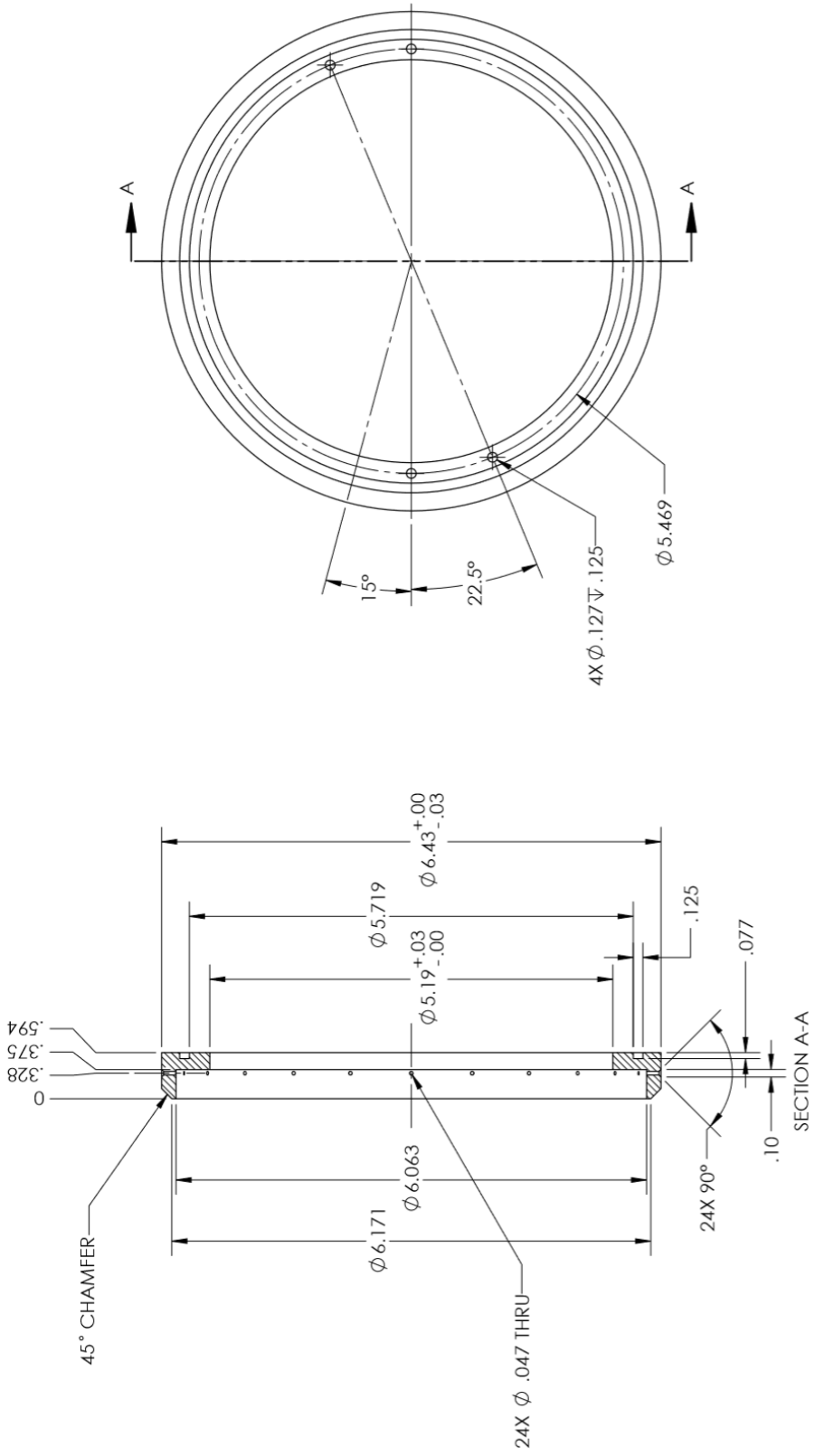

C.9 BASE PLATE